4D DSA: New Methods and Applications for 3D Time-Resolved Angiography for C-arm CT Interventional Imaging

By

Kevin Royalty

A dissertation submitted in partial fulfillment of
the requirements for the degree of

Doctor of Philosophy
(Biomedical Engineering)

at the
UNIVERSITY OF WISCONSIN-MADISON
2014

Date of final oral examination: 8/13/2014

The dissertation is approved by the following members of the Final Oral Committee:
Charles Mistretta, Ph.D., Professor, Biomedical Engineering
Charles Strother, M.D., Emeritus Professor, School of Medicine
M. Elizabeth Meyerand, Ph.D., Professor, Biomedical Engineering
Christopher Brace, Ph.D., Associate Professor, Biomedical Engineering
Oliver Wieben, Ph.D., Associate Professor, Biomedical Engineering

Abstract

Over the last decade, much advancement has been made in the field of interventional radiology and surgery. New devices and pharmacological therapies have been introduced to the market that allow the endovascular treatment of diseases ranging from occlusion of cerebral aneurysms to mechanical removal of blood clots from blocked arteries for patients suffering from acute ischemic stroke. Similarly, advancements in interventional imaging technologies have led to improved imaging techniques for diagnosis, treatment planning, and treatment evaluation. These C-arm-based imaging systems now routinely feature high-resolution flat panel x-ray detectors and powerful x-ray tubes allowing for high-spatial resolution imaging. This new hardware technology has enabled such technologies as 2D fluoroscopy/roadmapping, 2D digital subtracted angiography (DSA), 3D DSA, and C-arm CT soft tissue 3D imaging that are now routinely used during many interventional cases. These technologies currently allow for time-resolved 2D projection imaging or static 3D volumetric imaging. However, they do not provide time-resolved 3D angiographic imaging, which may be of value to the clinician for pathologies that include complex vascular anatomy and blood flow patterns that are difficult to fully understand using 2D DSA and 3D imaging alone.

4D DSA is a new method that is based on undersampled reconstruction techniques previously used in the field of magnetic resonance angiography (MRA) to enable high-speed, high-quality time resolved 3D angiography. 4D DSA allows for the use of a single C-arm 3D DSA acquisition combined with an injection of contrast to derive time-resolved 3D DSA volumes that the clinician can view from any projection angle at any point in time. These volumes have isotropic spatial resolution

of less than 0.5mm and in many cases can provide temporal resolution of the acquired projection data (typically on the order of 30 frames-per-second).

The work described in this dissertation is aimed at developing a basic validation framework for time-solved 3D DSA evaluation, developing metrics to characterize the complexity of vascular anatomy, optimize acquisition protocols for clinical practice, and evaluate initial pre-clinical and clinical results of the algorithm. These results are aimed at identifying methods, workflows, and potential clinical applications for 4D DSA. Finally, areas targeted for future research and development will be discussed in order to motivate continued work in this field.

Acknowledgements

I want to acknowledge and offer my sincere thanks to Dr. Charles Mistretta and Dr. Charles Strother for their patience, guidance, and mentoring over the last four years. Without their support, the work presented in this dissertation would not have been possible. I also want to thank the dissertation committee for their advice, guidance, and their commitment to this dissertation work. Thank you Dr. Meyerand, Dr. Wieben, and Dr. Brace!

Imaging research means little without the involvement and feedback of clinicians that will eventually be using this technology. The feedback, ideas, and motivation provided by Dr. Beverly Aagaard-Kienitz, Dr. David Niemann, Dr. Azam Ahmed, Dr. Mustafa Baskaya, Dr. Carolina Sandoval-Garcia, and Dr. Pengfei Yang were invaluable to this research. Thank you for your enthusiastic support and willingness to share your time on this project.

I want to thank Dr. Markus Kowarschik, Dr. Christopher Rohkohl, and Dr. Sebastian Schafer (my colleagues from Siemens Healthcare) for their support with this work and our thought-provoking conversations. I also want to thank Dr. Klaus Klingenbeck and Dr. Andrew Hall for their encouragement and commitment to this project.

Most importantly, I want to offer a loving thank you to my wife, Emily and my sons, Brandon and Duncan, for their endless support.

Table of Contents

Abstract i

Acknowledgements iii

Table of Contents iv

1 Chapter 1: Introduction and Background 1

1.1 Introduction 1

1.2 Clinical Background and Motivation for Work 2

1.2.1 C-arm Interventional Imaging Systems 2

1.3 Overview of Common Interventional Neurosurgical and Vascular Procedures 6

1.3.1 Cerebral aneurysm assessment and treatment 6

1.3.2 Ischemic Stroke and Cerebral Embolic Events 8

1.3.3 Vascular Malformations 9

1.4 Background on 4D DSA 10

1.4.1 Vessel Overlap Correction 12

1.4.2 Angular Minimum Search Method 13

1.5 Other Methods for Time-Resolved 3D Angiography for C-arm Systems 14

1.6 Motivation for the 4D DSA Modality 15

2 Chapter 2: Methods for Validation 17

2.1 Overview of Methods for Validation of the 4D DSA Algorithm 17

2.1.1 Framework Design 18

2.1.2 Input data 19

2.1.3 Evaluation of Results 19

2.2 Steps for Digital Phantom Creation 21

2.2.1 Step 1: 3D Acquisition of Vascular Anatomy 21

2.2.2 Steps 2 and 3: Computational Fluid Dynamics (CFD) Simulation and Creation of Time-Resolved Virtual 3D Angiogram Datasets 22

2.2.3 Creation of Final Digital Phantom Input Data for 4D DSA Framework 23

2.3 4D DSA Digital Phantoms 24

2.3.1 Tube Phantom Model 24

2.3.2 Aneurysm Phantom Model 25

2.3.3 Anterior and Posterior Cerebral Circulation Phantom Model 26

2.4 An Alternative Local Minimum Search Technique 28

2.5 4D DSA Digital Phantom Results 29

2.5.1 Tube Phantom Results 30

2.5.2 Aneurysm Phantom Results 33

2.5.3 Anterior and Posterior Cerebral Circulation Phantom Results 36

2.6 Discussion 39

2.6.1 Case 1: Single Vessel Center Voxel 39

2.6.2 Case 2: Single Vessel Center Voxel with Pulsatile Flow 41

2.6.3 Case 3: Single Vessel with Off-Center Voxel 43

2.6.4 Case 4: Two Vessels with Center Voxel 44

2.7 Conclusion 46

3 Chapter 3: Metric for Image Sparsity and Improved Methods for Vessel Overlap Detection 47

3.1 Introduction 47

3.2 Methods and Materials 50

3.2.1 2D Slice Digital Phantom Design 50

3.2.2 Methods for Generation of Ground Truth Datasets 51

3.2.3 Vessel Number Area Histogram 52

3.2.4 Methods for Evaluation of 4D DSA Results 53

3.3 Results 54

3.4 Summary 57

3.5 Future Work 58

3.5.1 Explicit Overlap Detection and Correction 58

4 Chapter 4: Acquisition Protocols for 4D DSA 60

4.1 Preliminary 4D DSA Acquisition Methods using Standard Commercial 3D Protocols 60

4.2 Preliminary 4D DSA Results Using Standard Protocols 61

4.2.1 Preliminary 5s DSA Acquisition Results 62

4.2.2 Preliminary 10s DSA Acquisition Results 63

4.3 Challenges and Limitations with Commercial 3D DSA Acquisitions for 4D DSA 65

4.3.1 Insufficient 3D DSA Scan Duration 65

4.3.2 Geometric Artifacts from Data Inconsistencies in the Acquired Projections 65

4.4 Experimental Acquisition Protocols for 4D DSA 67

4.4.1 Temporal Duration for Experimental 4D DSA Acquisitions 69

4.4.2 Data Consistency Improvements using Experimental 4D DSA Acquisitions 69

4.4.3 Clinical Workflow for Experimental 4D DSA Acquisitions Protocols 71

4.4.4 Experimental Protocol Results 73

4.5 Open Issues 75

4.5.1 Current Scan Protocols do not Consistently Result in Adequate Venous Visualization 75

4.5.2 Parenchymal Contrast Blush 76

4.5.3 Bolus Duration is Longer than Desired 77

4.6 Future Work 78

4.6.1 Multi-Rotation Protocols 78

4.6.2 Modeled Bolus Visualization 79

5 Chapter 5: Pre-clinical and Clinical Results and Applications 81

5.1 4D DSA Prototype Design and Implementation 81

5.1.1 4D DSA Prototype Workflow 82

5.1.2 3D and 4D DSA Reconstruction Engine 82

5.1.3 4D DSA Prototype User Interface 84

5.2 Pre-clinical Study and Evaluation 88

5.2.1 Methods 88

5.2.2 Results 95

5.2.3 Discussion 96

5.3 Clinical Study and Evaluation 97

5.3.1 Methods 98

5.3.2 Results 100

5.3.3 Radiation and Contrast Dose 100

5.3.4 Discussion 101

5.3.5 Conclusion 102

5.4 Future Work 103

5.4.1 Interventional Neuroradiology Applications 103

5.4.2 Non-invasive or Minimally Invasive 4D DSA 103

5.4.3 Quantitative 4D DSA 104

5.4.4 Applications for 4D DSA Outside of Neuroradiology and Neurosurgery 104

Appendix 1: Canine Image Review Form 106

Appendix 2: Reviewer Evaluation Form for Clinical AVM Imaging 120

References 121

Chapter 1: Introduction and Background

1.1 Introduction

The development of new techniques and devices for "minimally invasive" endovascular procedures has advanced significantly over the last 20 years, and has led to safer and faster procedures with reduced complication rates and improved mortality and morbidity rates across a wide range of procedures[1]–[4]. In parallel to these advancements in medical practices, the level of sophistication of the x-ray imaging technology available in the interventional operating room has also grown enormously over the last 20 years. The imaging modality most commonly used for interventional imaging is the C-arm angiography system.

C-arm angiography systems are used by a diverse set of operators (interventional radiologists, surgeons, neurologists, cardiologists, and many other sub-specialties) to perform a wide variety of endovascular diagnostic and surgical procedures. Diagnostic procedures using the interventional imaging system are typically aimed at using high spatial and temporal resolution to identify pathologies that are vascular in nature (stenosis, acute trauma, ischemic stroke, aneurysms, vascular malformations, tumors, and numerous others). Interventional surgical procedures are becoming increasingly complex as new devices and arterial-based drug therapies continue to expand at a rapid growth rate. The requirements of the interventional imaging system are becoming increasingly complex, as the need for both 2D and 3D high-quality anatomic and functional imaging becomes necessary to assess the state of the patient before, during, and after the interventional procedure.

Recently, magnetic resonance angiography (MRA) techniques have been developed that allow for sub-Nyquist acquisition and constrained reconstruction resulting in highly accelerated scan protocols. These advancements have altered the traditional tradeoffs between spatial and temporal resolution and have provided contrast-enhanced MRA techniques using as little as 1 cc of intravenous gadolinium[5]–[7]. The principles of constrained reconstruction have also been extended to other areas of medical imaging where significant dose reductions or SNR increases have been reported[8]–[10]. These principles can be applied to C-arm angiography to greatly increase the rate at which 3D time resolved volumes can be obtained, which are currently limited to approximately 1 volume every 5 seconds[11]. As a result, we have recently developed a C-arm based 4D digital subtraction angiography (DSA) method that provides a series of fully time resolved 3D DSA volumes (4D-DSA) at frame rates comparable to standard 2D DSA with higher temporal and spatial resolution than current MRA and CTA techniques[12], [13].

1.2 Clinical Background and Motivation for Work

1.2.1 C-arm Interventional Imaging Systems

The C-arm x-ray system consists primarily of an x-ray source (x-ray generator and tube) and camera (traditionally image intensifiers or more recently flat-panel detectors) mounted at opposite ends of a "C"-shaped gantry. Most C-arms are attached to a motorized gantry that can mechanically move the C-arm into different viewing angles, optimized by the operator for each specific procedure.

The patient lies on an operating table that is motorized and integrated with the imaging system to provide the physician and staff with the ability to control the C-arm and table movement all while working at the patient's side. Overhead monitors are positioned on a stand (typically mounted from the ceiling) and allow for real-time imaging and review while the procedure is ongoing. C-arm systems such as this have several imaging modes available to the operator for use in image-guided navigation and anatomical and physiological assessment of vascular and soft tissue anatomy. **Figure 1-1** shows an example of a state-of-the-art C-arm x-ray system that can be found in interventional and surgical suites at institutions around the world. Several specialties such as interventional neuroradiology and neurosurgery, electrophysiology, and pediatric cardiology require biplane systems that consist of two C-arms imaging simultaneously for precise device localization. Modern C-arm angiography systems have three basic modes of operation that are used during interventional and diagnostic procedures: 2D fluoroscopy, 2D angiography, and 3D imaging.

Figure 1-1: Robotic C-arm based angiographic imaging system (Artis zeego, Siemens AG, Forchheim Germany)

1.2.1.1 Two Dimensional Interventional Imaging

While 2D fluoroscopy and road mapping (subtracted fluoroscopy with vascular overlay) provide excellent imaging for navigation of high contrast medical devices, the low radiation dose limits the diagnostic use of these 2D imaging techniques for assessing anatomic vascular abnormalities or blood flow. For diagnostic catheter angiography, a higher dose (and typically

lower frame rate) acquisition is performed with an arterial injection of contrast agent to improve the signal to noise ratio (SNR) and provide excellent diagnostic quality imaging[14]. Interventional radiologists and endovascular surgeons often use digital subtraction angiography (DSA), which involves an initial mask frame that is used to subtract bone and soft tissue from subsequent image frames that are acquired after the introduction of contrast agent[15]. Due to the high spatial and temporal resolution of this technique, clear visualization of blood flow within both large and small blood vessels is possible, making DSA the gold standard for diagnostic vascular imaging. **Figure 1-2** shows an example of a DSA sequence after the coiling of a cerebral basilar tip aneurysm, and shows how all bone, soft tissue, and even the implanted coils are subtracted from the image such that only the contrast enhanced vessels are visible. In the cases where significant non-rigid motion occurs (such as interventional cardiology), subtraction is difficult and non-subtracted angiography is used with highly attenuating contrast agents to assess vascular lesions around the heart and lungs.

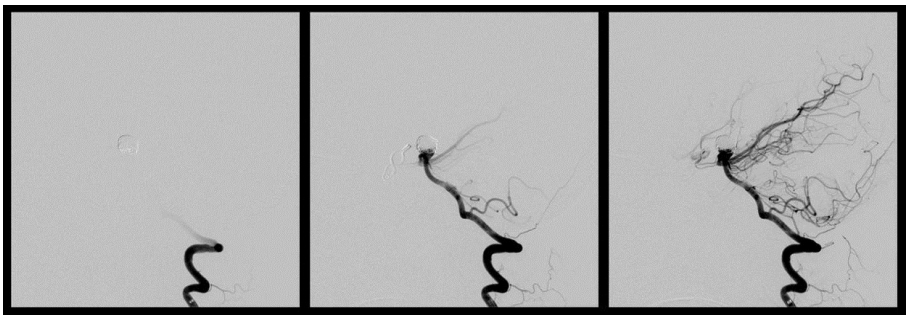

Figure 1-2: Three consecutive time frames of a digital subtracted angioigraphy (DSA) sequence

1.2.1.2 Three Dimensional Interventional Imaging

Three dimensional imaging using a C-arm angiography system is a relatively new technology. Factors such as slow gantry speed (typically on the order of 5-20 seconds), mechanical instability of the gantry, and patient motion make reliable and repeatable three-dimensional acquisitions a challenge. Ground breaking research by Fahrig et al. in 1997 demonstrated that a C-arm system with an image intensifier could be used in conjunction with arterial contrast agent injections to generate static 3D reconstructions of high contrast vascular structures (termed "rotational angiography")[16], [17]. Rotational angiography was quickly introduced into commercial C-arm angiography systems and was shown to be an essential tool in the diagnosis and treatment planning for vascular abnormalities such as cerebral aneurysms[18]–[20]. **Figure 1-3** shows an example of a modern rotational angiography reconstruction using a direct arterial injection of contrast agent into the internal carotid artery. In the early 2000's, flat detector based C-arm angiographic systems were introduced, replacing the standard image intensifier (II)-based systems. Flat detectors offer a number of advantages over II-based systems, including improved SNR and a relatively linear response to radiation intensity[21]. Shortly after the introduction of the flat panel, work by Zellerhoff et al. demonstrated the ability to reconstruct soft-tissue and small devices using a flat panel C-arm angiography system[22].

Figure 1-3: Example of a rotational angiographic reconstruction of a cerebral aneurysm

These new methods take advantage of the characteristics and sensitivity of the flat panel detector to reconstruct CT-like images with high spatial resolution and Hounsfield unit (HU) accuracy on the order of 10 HU[23]. **Figure 1-4** shows C-arm (a) low contrast reconstructions of the brain at the lower level of the lateral ventricles and (b) a deployed flow diverting stent with arterial enhancement by a diluted contrast injection. These images demonstrate the reasonable soft-tissue resolution and tremendous spatial resolution that can be accomplished with modern C-arm CT imaging hardware and reconstruction techniques.

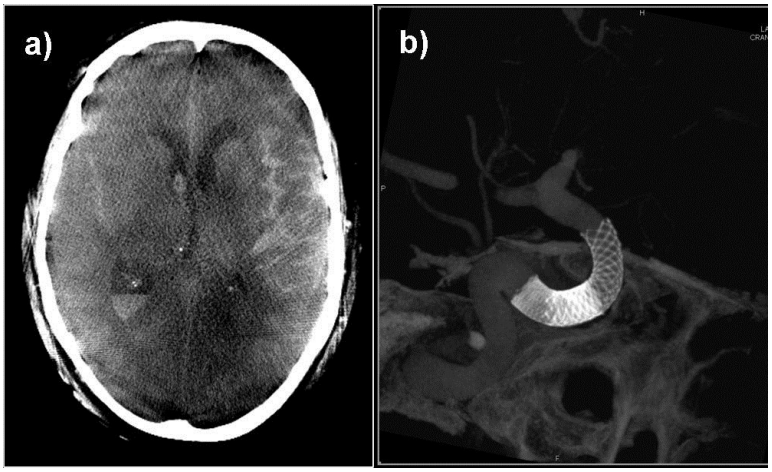

Figure 1-4: Low contrast, high spatial resolution C-arm CT-like reconstructions. **a)** 10mm MPR head C-arm CT. **b)** MIP presentation of flow diverting stent with dilute contrast agent injection

1.3 Overview of Common Interventional Neurosurgical and Vascular Procedures

1.3.1 Cerebral aneurysm assessment and treatment

Cerebral aneurysm treatment and evaluation are among the most common interventions performed by endovascular surgically trained neuroradiologists, neurosurgeons, and neurologists. The reported incidence rates for cerebral aneurysms are believed to be between 2-5% of the total population, with only a small percentage of those resulting in rupture and consequential subarachnoid hemorrhage[24].

Aneurysms are usually discovered as a result of imaging using diagnostic modalities such as MRA or CTA. However, follow-up imaging for further evaluation and treatment planning is almost always performed with 2D and 3D DSA using C-arm angiography due to the high spatial and temporal resolution of the system, combined with selective arterial injections to fully understand the vascular anatomy, and to rule out additional aneurysms that may have been missed in the diagnostic MRA or CTA studies[19], [25]–[27]. **Figure 1-5** shows an example of a 2D DSA and 3D DSA acquisition of the same intracranial aneurysm. Note the additional vascular detail provided by the 3D DSA reconstruction. A combination of both 2D DSA and 3D DSA imaging is required to understand both the anatomical detail and complex blood flow patterns that exist with cerebral aneurysms.

The treatment options and techniques for aneurysms have evolved significantly over the last few decades. While surgical clipping remains as one of the primary treatment options, endovascular options have become safer and even preferred for certain types and locations of intracranial aneurysms. Aneurysm coils are by far the most frequent endovascular device used to treat aneurysms[28]. Depending on the aneurysm geometry, stents or balloons may be used to temporarily or permanently support the coil mass in the aneurysm to achieve a stable result. Recently, a new class of flow diverting devices have been introduced to the market that have shown great safety and effectiveness for treatment of large or fusiform aneurysms that were previously not

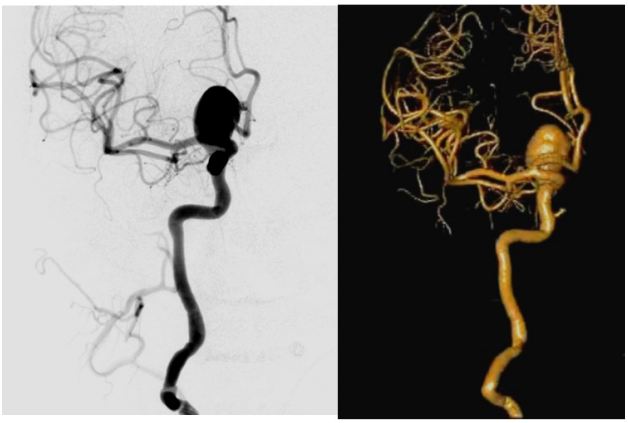

Figure 1-5: 2D DSA (left) and 3D DSA (right) images of an intracranial aneurysm

recommended for coiling and dangerous to treat surgically[29]. A C-arm CT image of a flow diverting stent is shown in **Figure 1-4.**

1.3.2 Ischemic Stroke and Cerebral Embolic Events

Diagnosis and treatment of ischemic events represents another significant population of procedures in the interventional neuroradiology and neurosurgery suites. Procedures in this group range from extracranial and intracranial assessment of acute and chronic stenosis, vessel dissection, vasospasm following subarachnoid hemorrhage, and acute ischemia as a result of clot or embolism, which can originate from a variety of vascular locations.

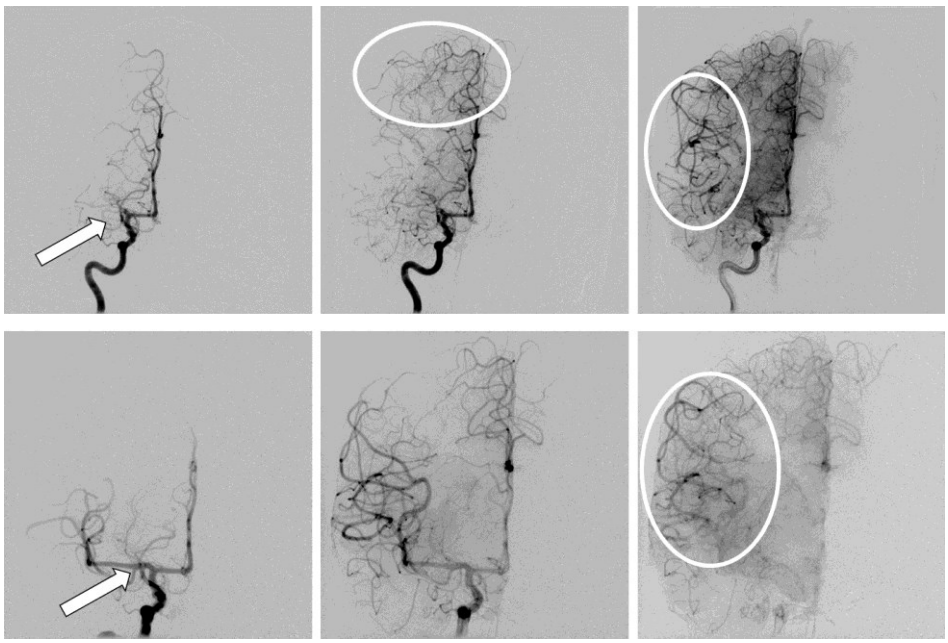

Figure 1-6: Example of an acute stroke pre and post treatment. The upper row of images shows the early, mid, and later phase angiograms before treatment. The white arrow shows the location of the clot which is occluding flow into the middle cerebral artery (MCA). The circles show the collateral supply (upper middle) and the flow into the cerebral territory supplied by the compromised MCA (upper right). The lower row of images shows the early, mid, and late phase angiograms after removal of the clot by endovascular intervention. The time series of angiograms clearly shows the successful revascularization of the MCA-supplied territory

Figure 1-6 shows an example of a 2D DSA angiogram taken before and after removal of a clot that was obstructing flow into the middle cerebral artery (MCA). Clinicians need both high resolution anatomical details of the blood vessels to identify segments where flow is occluded, as well as a time sequence of images to understand the timing of the collateral pathways that may be supplying blood flow to ischemic regions that are compromised by a proximal arterial occlusion. Similar imaging requirements are needed after treatment to assess the success of the intervention and if additional intervention is necessary to further benefit the patient.

1.3.3 Vascular Malformations

Vascular malformations of the brain are among the most complex and difficult to treat vascular diseases that have been identified. Vascular malformations are defined by locations in the vascular anatomy where an unusually large number of small arterial vessels come together (nidus) and connect directly to veins, bypassing the normal capillary system that provides essential nutrients to the cellular tissue. The malformations can result in seizures, hemorrhage, migraines, paralysis, and a host of other neurological deficits and disorders. The causes of vascular malformations are not well understood, but is believed to be primarily due to genetic disorders or injury[30].

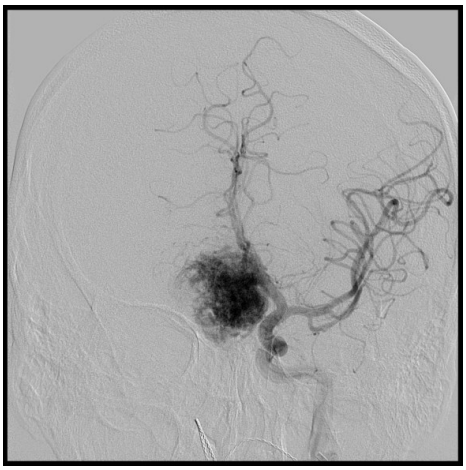

Figure 1-7: DSA of a cerebral AVM using an arterial injection of contrast agent

Diagnostic imaging of vascular malformations often includes multiple modalities in order to fully understand the anatomy and flow patterns for each case. CT and MR are often used for frontline

diagnostic imaging, and if the patient is considered exclusively for surgery or radiosurgery, these may be sufficient for treatment planning[31], [32]. For large and complex vascular malformations, a combination of arterial embolization, surgical resection, and radiosurgery may be employed[33], [34]. Cases that involve endovascular treatment will typically undergo selective arterial angiograms using DSA to methodically interrogate and characterize the arteries that feed and the veins that drain the vascular malformation[35]. **Figure 1-7** shows an example of a cerebral AVM. Contrast-enhanced C-arm CT has also been shown to offer excellent image quality and diagnostic value for very small AVMs that are undetectable using other imaging modalities, including 2D DSA[36].

1.4 Background on 4D DSA

In 2009, Mistretta et al. [13] introduced a new method for generating time-varying 3D angiographic volumes using rotational angiographic acquisitions on a commercial C-arm angiography system. Using a sparse vascular 3D volume (created by standard 3D rotational angiography) as a constraining volume, temporal projections can then be applied to the constraint volume to generate a time-varying series of 3D volumes that retain a spatial resolution comparable to the original 3D reconstruction. **Figure 1-8** below shows a pictorial representation of the 4D DSA algorithmic workflow.

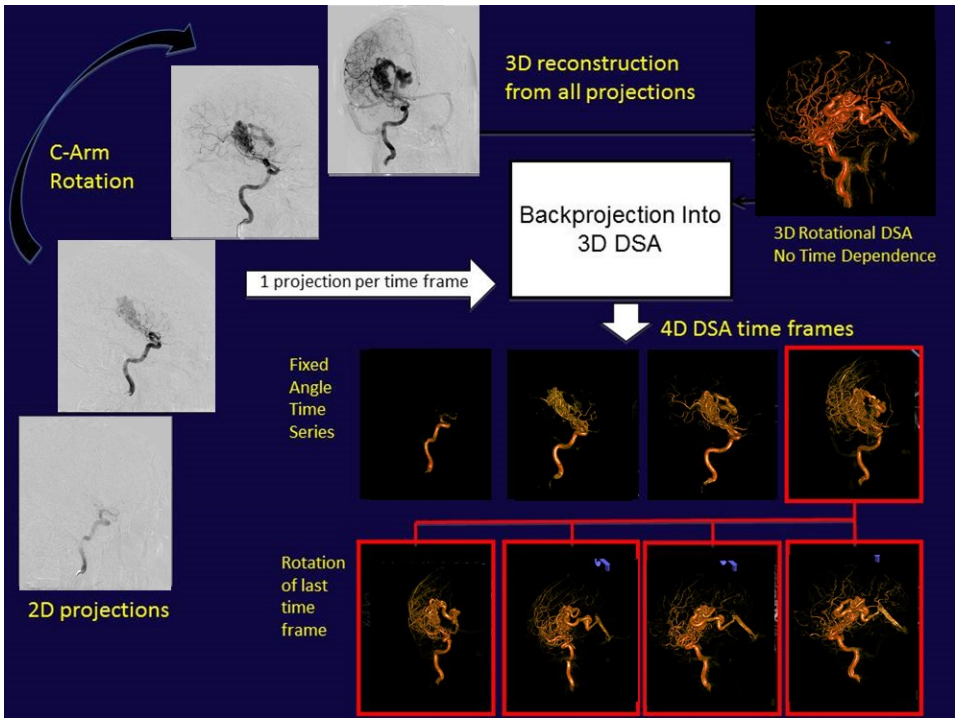

Figure 1-8: 4D DSA algorithmic workflow

The following mathematical notation can be used to describe the basic 4D DSA algorithmic implementation:

$C: \mathbb{R}^3 \to \mathbb{R}$: constraining volume $C(x)$; $C(x)$ is generated by segmenting a CT reconstruction algorithm (typically filtered back projection) of subtracted projections. The segmentation step assigns a zero value to all non-vascular voxels.

K : A convolution kernel applied to the projection images to improve SNR and account for small misregistrations of the 2D to 3D mapping.

$p: \mathbb{N} \times \mathbb{R}^2 \to \mathbb{R}$: time-dependent subtracted projection value $p(t,u)$, after pre-processing of the projection image, *t*: time point, *u*: detector coordinate (continuous representation)

$A: \mathbb{N} \times \mathbb{R}^3 \to \mathbb{R}^2$: 3D to 2D perspective projection, $A(t,x) = u$

$L(t,u) = \{x \in \mathbb{R}^3; A(t,x) = u\}$: X-ray path through object point x at time t hitting detector at position u (line integral of x-ray attenuation projected through volume $C(x)$)

$$f_1(t,x) = C(x) \cdot \frac{K \star p(t, A(t,x))}{K \star \int_{L(t,A(t,x))} C(y)dy} \qquad (1\text{-}1)$$

$f_1(t,x)$ represents the 4D DSA volume after the application of the algorithmic steps.

The denominator of this formula can approach zero for cases of little to no attenuation along the line integral of x-ray attenuation values of the constraint dataset. In these cases, both the numerator and the denominator are assumed to be approaching zero and value is simply assigned a value for zero to enforce numerical stability and avoid divide by zero errors.

1.4.1 Vessel Overlap Correction

The algorithm described above is designed to recover the 3D signal in time for situations where there is little or no vessel overlap in 3D to 2D perspective projection for a given time point. When vessel overlap occurs, the basic 4D DSA algorithm does not include methods to appropriately reweight the temporal encoding to the 3D vessels to account for overlapping vascular structures that have different enhancement levels at the same point in time. As a result, all vessels that are overlapping along a given x-ray path will receive an equal weighting for a given point in time. This can lead to either overestimation or underestimation errors for a given voxel in time depending on the values of the other overlapping vascular structures at that same point in time.

1.4.2 Angular Minimum Search Method

In order to improve the accuracy of the 4D DSA reconstruction in situations of vascular overlap, a modified 4D DSA reconstruction method has been devised that selects local minimum for each voxel based on a small angular range of measured projection values that are close in time to the projection time point that is to be encoded. The fundamental idea is that vessels that overlap will introduce sharp increases in measured attenuation values. These situations can be corrected by using a local minimum for a given voxel (associated with that measured projection value) close to the time point in question. The following mathematical notation can be used to describe this variant of the 4D DSA algorithm that results in a two-step process:

For all locations $\boldsymbol{x}$ of vascular voxels:
For all $\boldsymbol{t}$:

Step 1: $$t^* = argmin_{t' \in [t \pm \Delta\tau]} \left[K * p\left(t', A(t', x)\right) \right] \quad (1\text{-}2)$$

Step 2: $$f_1(t, x) = \frac{C(x) \cdot [K \star p\left(t^*, A(t^*, x)\right)]}{K \star \int_{L\left(t, A(t^*, x)\right)} C(y) dy} \quad (1\text{-}3)$$

Figure 1-9 provides a simple example of a resulting time contrast curve (TCC) from one of two vessels with different enhancement patterns that overlap in a local range of projections without and with the minimum angular search correction applied.

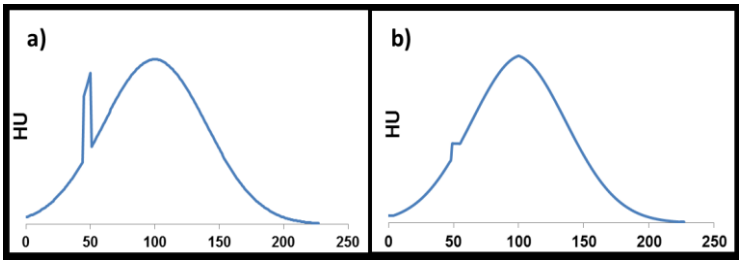

Figure 1-9: a) 4D DSA TCC result with overlapping vessels and no corrections b) 4D DSA TCC results with overlap correction by minimum angular search algorithm

Feasibility and preliminary

results of the 4D DSA algorithm were published in 2013 by Davis et al.[12] However, to date there have been no efforts to evaluate and optimize the 4D DSA acquisition methods, evaluate and validate the TCCs generated by 4D DSA, or perform a systematic clinical evaluation of the 4D DSA reconstructions.

1.5 Other Methods for Time-Resolved 3D Angiography for C-arm Systems

Other research groups (Schmidt et al in 2005[37], Waechter et al in 2008[38], Copeland et al in 2010[39], Waechter et al in) have proposed and evaluated other methods for measuring and displaying 4D angiography based on C-arm systems. There are two primary differences between the 4D DSA method presented here and these methods. First, the 4D DSA method presented here uses the projection data acquired for the 3D dataset as the basis for the measurement of the transit of contrast material. The other work in this domain relies on previously acquired 3D data and a second acquisition (and contrast injection) of fixed angle 2D DSA data that is used for measuring the transit of contrast material. The 4D DSA method has the advantage that the acquired projections have already been calibrated such that the 2D to 3D geometrical registration has already been accomplished. The other methods rely on a separate calibration and registration step to register each projection to the 3D data. The 4D DSA also has the advantage that it requires only a single injection of contrast agent. The second difference is that the 4D DSA algorithm relies only on the measured projection data as a means to calculate the 4D data, and does not rely on satisfying any smoothness or other criteria through an iterative regularization procedure. This allows for the 4D DSA algorithm fewer constraints related to computation complexity and the possibility for shorter reconstruction times.

1.6 Motivation for the 4D DSA Modality

The current imaging requirements for diagnosis, treatment planning, and post-procedural imaging are well understood for cases involving intracranial aneurysms, vascular malformations, and acute and chronic cerebral ischemia. **Table 1-1** below provides a simple overview of these general imaging requirements.

	Aneurysm	Vascular Malformation	Ischemic Stroke
Spatial Resolution (less than 0.75 mm)	√	√	
Temporal Resolution (greater than 3 samples/sec)		√	
3D Imaging	√	√	
Selective Angiography	√	√	√

Table 1-1: Imaging modality requirements per neurovascular disease type

As a result of these imaging requirements, a combination of imaging modalities is often used during the diagnosis, treatment planning, intervention, and follow-up phase for these neurovascular disorders. **Table 1-2** shows a comparison of these imaging requirements across the common imaging modalities, including 4D DSA. As shown in **Table 1-2**, 4D DSA has the potential to provide an imaging modality that meets all of the requirements necessary to diagnose, plan, evaluate treatment, and follow up patients with typical neurovascular disorders.

	2D DSA	3D DSA	4D DSA	MRA	CTA
Spatial Resolution (less than 0.75 mm)	√	√	√		√
Temporal Resolution (greater than 3 samples/sec)	√		√		
3D Imaging		√	√	√	√
Selective Angiography	√	√	√		

Table 1-2: Comparison of imaging requirements across common imaging modalities and 4D DSA

Both patient and operator radiation dose is continuing to become an important consideration for interventional and diagnostic procedures. Recent studies show that selective 3D DSA imaging provides advantages in both diagnostic accuracy and radiation dose savings compared with 2D DSA imaging alone[18], [19]. Schueler et al. found that 3D DSA can save up to 4 times the peak skin radiation dose compared to biplane 2D DSA[40]. As a result 3D DSA is now commonly performed as part of the workup for cerebral aneurysms to avoid performing iterative 2D DSA acquisitions to find optimal working projections for aneurysm treatment. However, because 3D DSA does not include temporal information, additional 2D DSA acquisitions are required to assess the vascular filling of anatomical structures. 4D DSA can provide a time series of 3D volumes, allowing the operator to visualize any desired viewing projection for all time points of vascular filling, including projections that are not physically obtainable with 2D DSA due to limitations of the C-arm gantry positioning. Additionally, since 4D DSA is derived from a rotation angiography acquisition, 4D DSA has the potential to further reduce the radiation dose by including temporal information in the 3D DSA that would otherwise require additional 2D DSA scans.

Chapter 2: Methods for Validation

2.1 Overview of Methods for Validation of the 4D DSA Algorithm

4D DSA provides spatial and temporal resolution that has the potential to exceed any equivalent gold-standard imaging modality. Therefore, validation of the 4D DSA reconstruction technique is a challenge outside of digital simulations, since it is difficult to measure the real world ground truth in 4D with existing modalities. Publications on 4D DSA to date have provided validation based on simulations with a single CT slice and a limited number of simulated vascular structures, or by observer analysis based in preliminary *in vivo* data[12], [13]. This chapter outlines the development of a validation framework that uses currently available tools as a means to assess and validate the accuracy of the 4D DSA reconstructions. The framework can be used with both digital simulated data and real-world flow phantoms where we can accurately reproduce the physiology and injection profiles for repeated scans without concern for radiation and contrast dose.

The validation methods and framework can be used as a means to evaluate the performance of the 4D DSA algorithm with vascular datasets of varying complexity. The framework can also be used to evaluate the performance of different normalization or correction algorithms, such as the minimum angle search algorithm which is aimed at correcting situations where vessels overlap each other in a projection or series of projections that confound the algorithm's ability to properly recover the 4D TCC.

2.1.1 Framework Design

The 4D DSA algorithm can be represented in block diagram form as a series of inputs and outputs to algorithm sub-blocks. The inputs correspond to measured projection data, system geometry information (2D/3D transforms), a 3D constraint volume, and reconstruction parameters. The output is the series of time-resolved 3D volumes generated by the 4D DSA algorithm applied to the inputs. **Figure 2-1** provides a graphical block diagram description of the 4D DSA inputs, outputs, and some of the basic steps within the algorithm.

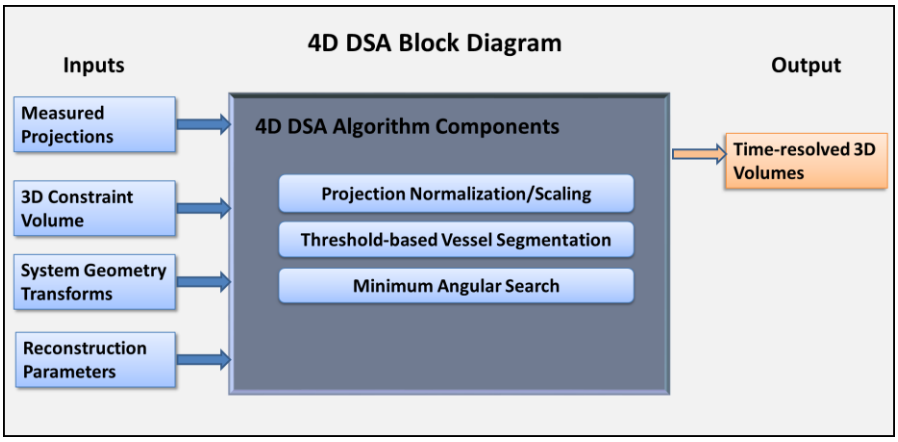

Figure 2-1: Block diagram of 4D DSA algorithm illustrating system inputs and outputs

For this work, we will refer to the static 3D volume as $V(x)$ where x represents a 3D location $\{x, y, z\}$ in $\mathbb{R}^3$. Measured projections will be noted as $P(u, t)$ where u represents a 2D location $\{u, v\}$ in $\mathbb{R}^2$ and $t \epsilon \{1,2,..T\}$ represents the individual acquired projection in time. A_t represents the system matrix operator that defines the transform from 3D voxel space to the 2D projection space where $P(u, t) = A_t V(x)$. Finally, the 4D DSA result is represented as $F(x, t)$ where x represents a 3D location $\{x, y, z\}$ in $\mathbb{R}^3$ and $t \epsilon \{1,2,..T\}$ represents the individual acquired projection in time that is encoded by the 4D DSA algorithm.

The overall goal of the framework is to apply a known set of input data (ground truth) that can then be used compare the accuracy of the results generated by the algorithm. This allows the use of

standardized error metrics and observer-based analysis to provide a benchmark to compare the performance of different reconstruction parameters or evaluate changes to the reconstruction algorithm.

2.1.2 Input data

For this framework, the input data falls into one of two categories. The first category involves digitally simulated voxel-data where a known geometric phantom with a mask of voxels has a simulated transit of contrast starting at a proximal location and traverses the vascular tree in a prescribed manner. In these cases, we have full knowledge of the original ground truth time-varying volumetric data (referred to here as $G(X,t)$ that can be compared (voxel by voxel) to the 4D DSA result. The ground truth time-varying volume can be reprojected to create the subtracted measured projection data $P(U,t)$ that is used as input to the 4D DSA algorithm.

The second type of input data for the framework consists of acquired data from a flow phantom study where the injection and acquisition can be well controlled and easily repeated in order to gain additional ground-truth measurements. In this case, the ground truth measurements are measured with standard 2D DSA from various projection angles. The 4D DSA results can then be reprojected to the matching orientations (relative to the ground truth acquisitions), and evaluated in 2D coordinates rather than 3D as was done with the digital phantom study. For the purposes of this dissertation work, I will limit the scope of this work to only the simulated digital phantom data. Future work will include the evaluation of flow phantom data.

2.1.3 Evaluation of Results

2.1.3.1 Error Analysis for Digital Phantom Evaluations

Once the 4D DSA results are generated (based on the ground truth input data), we can directly compare the algorithm results $F(x,t)$ with the original ground truth data $G(x,t)$. A 4D dataset of voxel-wise error measurements are calculated to provide voxel-specific error values (relative to the ground truth) of the 4D DSA algorithm for each point in time. This allows for the visual evaluation of which vessel segments had the highest or lowest error values, which helps to understand how the vessel sparsity and spatial location impacts the accuracy of the algorithm. **Table 2-1** provides an overview of the different error parameters used to determine overall error of the reconstruction. In addition to root mean squared error (RSME) to the ground truth, it is also important to include parameters that did not penalize scaling differences between the 3D+T results and the ground truth. Rather, these parameters focus on the temporal behavior of the contrast dynamics (time of peak, bolus arrival time, and full width half max), as there are clinical applications where recovery of the absolute attenuation value is not required as long as the attenuation changes over time are relatively correct.

Evaluation Parameter	Equation
Root Mean Squared Error (RMSE)	$RMSE(X) = \sqrt{\frac{\sum_{t=1}^{N} \left(G(X,t) - F(X,t)\right)^2}{N}}$
Absolute error for Time of Peak (ET_{max})	$ET_{\max}(X) = \lvert T_{\max}\left(G(X)\right) - T_{\max}\left(F(X)\right)\rvert$
Absolute error for Bolus Arrival Time (ET_{ba})	$ET_{\mathrm{ba}}(X) = \lvert T_{\mathrm{ba}}\left(G(X)\right) - T_{\mathrm{ba}}\left(F(X)\right)\rvert$
Absolute error Full Width Half Max (EFWHM)	$EFWHM(X) = \lvert FWHM\left(G(X)\right) - FWHM\left(F(X)\right)\rvert$

Table 2-1: Summary of measured error parameters

In addition to the voxel-specific measurements, global values of mean and standard deviation will be calculated for each of the evaluation parameters to assess overall error for each algorithmic method.

Finally, color maps of the results and the error distributions can be created to better understand the spatial distribution of the error in addition to histogram plots and basic mean and standard deviation metrics.

2.2 Steps for Digital Phantom Creation

In order to evaluate the 4D DSA algorithm for general diagnostic use, it is important to consider not just one digital phantom, but a series of digital phantoms with varying vascular complexity. The creation of the time resolved digital phantoms is a multi-step process, but is generally the same for all digital phantoms developed and used in this research.

2.2.1 Step 1: 3D Acquisition of Vascular Anatomy

The first step of the process involves the 3D imaging of a physical flow phantom in order to define the 3D vascular geometry of the digital phantom. For all cases, the flow phantoms was filled with a mixture of saline and contrast, de-bubbled, and then allowed to sit for several hours in order to allow for the homogenous diffusion of contrast mixture throughout the phantom. After several hours, the phantom is then placed on the table of the C-arm CT scanner (Siemens Artis zee biplane, Siemens AG, Forchheim, Germany) with realistic clinical positioning and then imaged with the highest quality C-arm CT imaging protocol. In this case, the DynaCT protocol used was the 20s DR-H protocol that includes 496 projection images acquired at the highest 3D imaging radiation dose (1.2uGy/F) at 70kV tube current.

After image acquisition, a 3D volume of the phantom was reconstructed at the full field of view with an image matrix of 512x512x388 voxels with an isotropic spatial resolution of 0.47 mm. A standard edge enhancement vessel kernel was used in order to enhance the vessel wall boundary.

After reconstruction, the volumes are reviewed for any significant artifacts (metal streak artifacts, beam hardening artifacts, or truncation artifacts) that may impact the quality of the simulation results.

2.2.2 Steps 2 and 3: Computational Fluid Dynamics (CFD) Simulation and Creation of Time-Resolved Virtual 3D Angiogram Datasets

Steps 2 and 3 are based on the work by Endres et. al[41] where virtual angiograms are generated based on results from a CFD simulation. The precise methods are covered in detail in the publication and are beyond the scope of this work, so only a high-level overview will be discussed.

First, the 3D dataset from step one is cut, cropped, segmented, and then converted to a surface mesh. Secondly, a set of initial conditions and boundary conditions are defined. In the case of our digital phantoms, we chose to simulate non-pulsatile using standard values for Newtonian fluid density and viscosity with steady-state flow in order simply the phantom. The CFD solver then attempts to solve the set of Navier-Stokes equations using a discretized iterative approach to generate velocity and pressure data.

Once the CFD simulation is complete for a given dataset, then the virtual angiography dataset is generated. This is accomplished using a particle-based approach, where the contrast transport is modeled as massless and dimensionless particles deposited and freely movable within space, but bounded by a rigid vessel wall. The virtual angiography method uses a combination of the velocity field influence on the particle along with an algorithmic model of the diffusive mixing that a contrast agent undergoes when injected with blood.

For the purposes of our study, we choose to use time steps and simulated contrast injections that were similar to our clinical 4D DSA acquisitions (based on the 12s DSA protocol). Specifically, 304 time points were considered, spaced at 33ms intervals, which is approximately the acquisition rate

for a standard 12s DSA acquisition. This new acquisition protocol is described in detail in Chapter 4. Particle delivery was simulated for the first 7 seconds, similar to the injection protocol used for our clinical cases. Once the simulation was completed, the time-resolved virtual 3D angiogram is converted into the 4D DSA data format (described in Chapter 5). I want to acknowledge and sincerely thank Juergen Endres (University of Erlangen, Germany), Dr. Thomas Redel (Siemens AG), and Dr. Markus Kowarschik (Siemens AG) for generating the virtual angiography results based form our C-arm CT data for these digital phantoms.

2.2.3 Creation of Final Digital Phantom Input Data for 4D DSA Framework

Once we have the time-resolved virtual 3D angiogram for each digital phantom, we must then convert this data to the input format required by the 4D DSA framework. First, a 3D volume as $V(x)$ is required as input to serve as the constraint for the 4D DSA reconstruction. In this case, we used the temporal MIP (peak TAC value for each voxel) as the voxel-wise HU value for $V(x)$. Secondly, measured projections $P(u,t)$ need to be created. In this case, we use the calibrated system projection matrices for the 12s DSA acquisition (A_t) to define the transform from 3D voxel space at any given point in time to the 2D projection space where $P(u,t) = A_t G(x,t)$ and calculate a reprojection from the time-resolved volumetric angiogram to create the simulated subtracted projections. The simulated $P(u,t)$, derived $V(x)$, and the actual calibrated system matrix A_t serve as the inputs to the 4D DSA framework for these digital phantom studies.

2.3 4D DSA Digital Phantoms

Three digital phantom models were used for this preliminary validation work, and will be described in this section. In the future, additional models with more patient-specific anatomy can be used for further evaluation of 4D DSA algorithm performance and parameter tuning.

2.3.1 Tube Phantom Model

The simplest digital phantom was derived from a 3D data acquisition of length of surgical tubing with an inner diameter of 6.35mm (comparable in size to the internal carotid artery in adults) that was filled with a mixture of 25% iodinated contrast agent (Omnipaque 300, GE Healthcare, Milwaukee, WI) and 75% saline. The surgical tubing was placed in the shape of an upside down 'U' on the table of the angiography system (Siemens Artis zee biplane, Siemens AG, Forchheim, Germany), and then a C-arm CT acquisition was performed and reconstructed using a commercial workstation (syngo X-workplace, Siemens AG, Forchheim, Germany). This model allows for the evaluation of two basic challenges to the 4D DSA algorithm. The first is how the respective algorithm under consideration can detect and correct for the overlap of the portions of the tubing filling in opposite directions. The second challenge is for the algorithm to deal with deriving 4D DSA temporal information where the projection rays are not orthogonal to the vessel centerline, but may even run parallel to the vessel centerline. This situation can cause complications with determining the value that a voxel located along the direction of the projection ray (parallel to the direction the vessel is running) will be assigned at that point in time.

As outlined by the steps in section 2.2, the 3D model (derived from the C-arm CT reconstruction) was used to create the time-resolved digital phantom data. As discussed, 304 discrete time points were created for the digital phantom, which coincides with the number projection acquisitions acquired during the longest 4D DSA acquisition. **Figure 2-2** shows a volume rendering of the tube digital phantom for selected points in time. The early and late time frames show the wash-in and wash-out of virtual contrast medium. Another important characteristic of this model is that the filling of the vessels is non-uniform across a cross-section of the vessel for the wash-in and wash-out phases. This is an important point that will be discussed in the results section.

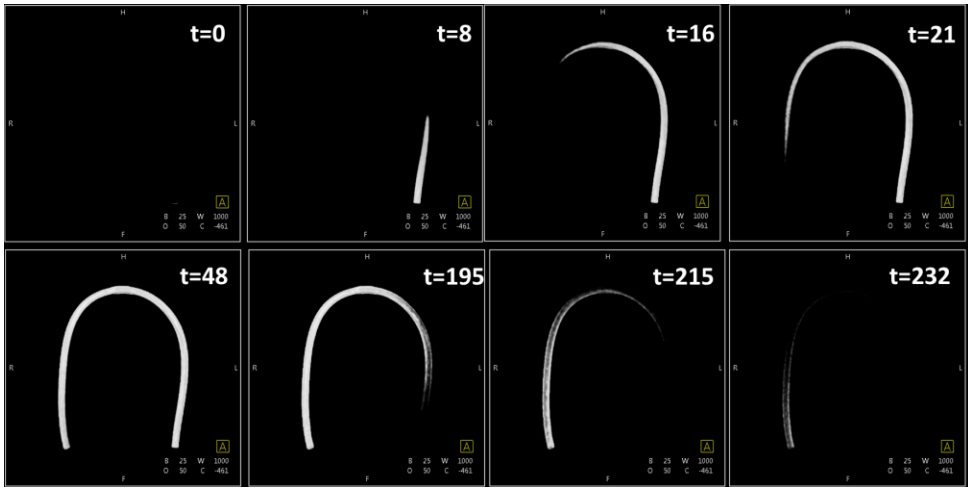

Figure 2-2: Volume rendering of select time frames for digital phantom tube model

2.3.2 Aneurysm Phantom Model

The aneurysm digital phantom is derived from a commercially available flow phantom ('The Replicator', Vascular Simulations, Stony Brook, NY) that is based on real clinical patient data. This phantom model includes the right internal carotid with a cavernous carotid aneurysm and the first branches of the anterior cerebral artery (A1) and middle cerebral artery (M1). The A1 and M1 terminate into a common output vein, creating an anatomical model with a single input and a single output. The C-arm CT scan was performed while the flow phantom was operating with a 5F guide

catheter placed just past the origin of the internal carotid artery. A contrast injection using 50% iodinated contrast agent (Omnipaque 300, GE Healthcare, Milwaukee, WI) and 50% saline was used in conjunction with the C-arm CT acquisition. This more complex model introduces the challenges of additional overlapping vessel segments, as well as a large aneurysm that can exhibit non-uniform enhancement patterns.

As outlined by the steps in section 2.2, the 3D model (derived from the C-arm CT reconstruction) was used to create the time-resolved digital phantom data. Similar to the previous digital phantom, 304 discrete time points were created. **Figure 2-3** shows a volume rendering of the aneurysm digital phantom for selected points in time. The early and late time frames show the wash-in and wash-out of virtual contrast medium. The figure illustrates the uneven filling of the aneurysm in the early and late frames (blue arrows) where the contrast agent is first entering or leaving the aneurysm.

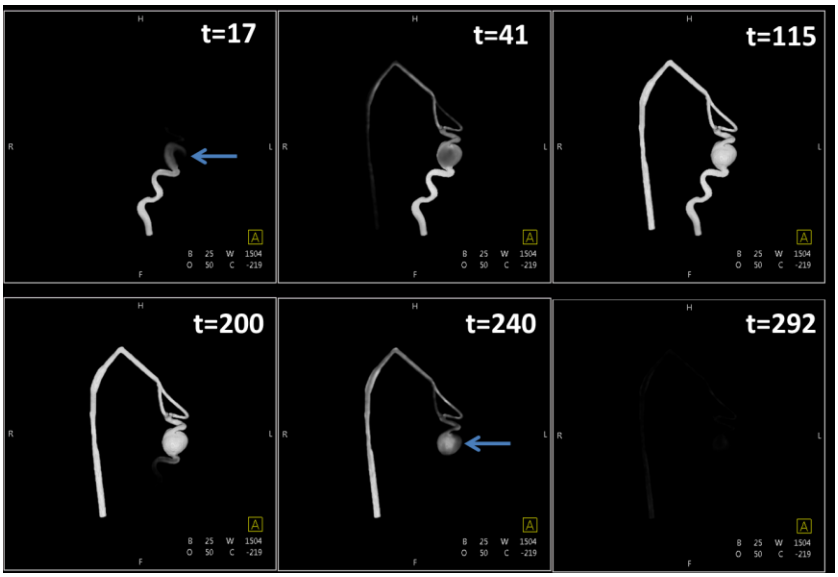

Figure 2-3: Volume rendering of select time frames for digital phantom aneurysm model. Blue arrows show the early and late enhancement phases of the aneurysm

2.3.3 Anterior and Posterior Cerebral Circulation Phantom Model

The final digital phantom is derived from a commercially available flow phantom (Anterior & Posterior Circulation Phantom, Shelley Medical Imaging Technologies, Ontario, Canada) that is also

based on real clinical patient data. This phantom model includes left and right internal carotid arteries, the left and right vertebral arteries, all connecting at a communicating Circle of Willis including the anterior cerebral arteries (ACA) and left and right middle cerebral arteries (MCA). The phantom consists of a block of silicone with the vascular structures hollowed out of the block. The phantom outputs were plugged and then the inputs where filled with contrast agent (Omnipaque 300, GE Healthcare) diluted to 50% with saline solution. The inputs to the phantom were then plugged and the phantom was allowed to sit for 24 hours in order to allow the contrast agent to diffuse evenly throughout the phantom. The C-arm CT scan was performed and the dataset was reconstructed in the same manner described in the previous sections. This is the most complex phantom model and introduces the challenge of having numerous overlapping vessel segments that would be similar to an intravenous or aortic arch injection of contrast that enhances all major vessels in the cerebral circulation.

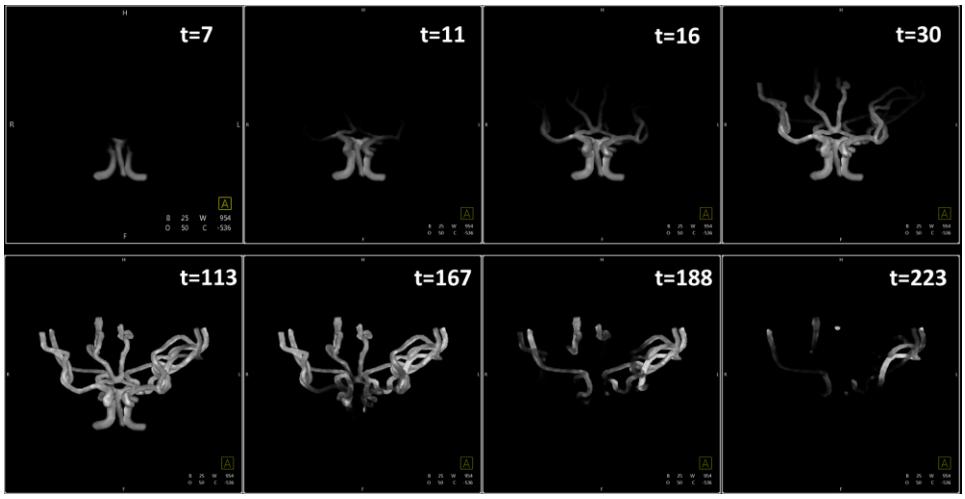

Figure 2-4: Volume rendering of select time frames for digital phantom with communicating anterior and posterior cerebral circulation vessel model.

As outlined by the steps in section 2.2, the 3D model (derived from the C-arm CT reconstruction) was used to create the time-resolved digital phantom data. Similar to the previous digital phantoms, 304 discrete time points were created. **Figure 2-4** shows a volume rendering of the

aneurysm digital phantom for selected points in time. The early and late time frames show the wash-in and wash-out of virtual contrast medium.

2.4 An Alternative Local Minimum Search Technique

For the purposes of this work, we consider an alternative minimum angular search technique that varies slightly from the one described in section 1.4.1, but could be considered as a possible alternative. This modified search algorithm is easy to implement and requires little additional computation above and beyond the standard 4D DSA algorithm. Henceforth in this chapter, we will refer to this new local minimum search as **Local Minimum Search Method 2** and the original local minimum search algorithm will be referred to as **Local Minimum Search Method 1**.

Formally, Local Minimum Search 2 is defined as:

For all locations $\boldsymbol{x}$ of vascular voxels:
For all $\boldsymbol{t}$:

Step 1: $t^* = argmin_{t' \in [t \pm \Delta t]} \left[\int_{L\left(t', A\left(t'^*, x\right)\right)} C(y)dy \right]$ (2-1)

Step 2: $f_1(t,x) = \frac{C(x) \cdot [K \star p\left(t^*, A(t^*, x)\right)]}{K \star \int_{L\left(t, A(t^*, x)\right)} C(y)dy}$ (2-2)

This modified algorithm has one primary difference to the Local Minimum Search 1. Rather than evaluating the non-normalized local minimum of a range of measured projection values (time-dependent attenuation changes) mapped to a given voxel by the system matrix $A(t,x)$, this modified algorithm searches a range of projection values for the minimum reprojected value (mapped to a given voxel) based on the constrained 3D volume $C(x)$.

Intuitively, this method is searching for reprojected (line integral value) that represents the lowest cumulative attenuation value along a range of projections that can be mapped to a given voxel that is to be temporally encoded. The rationale behind this method is that increasing instances of vessel overlay for a given voxel will lead to a larger accumulated attenuation value (line integral value) for the reprojection. In this case, we select the projection angle with the lowest line integral value (based on the reprojection of the constraint 3D voxel data) in order to determine the time point that should be considered the "overlap-corrected value" for the 4D DSA result. **Figure 2-5** provides a pictorial description of the steps for the method 2 minimum search algorithm.

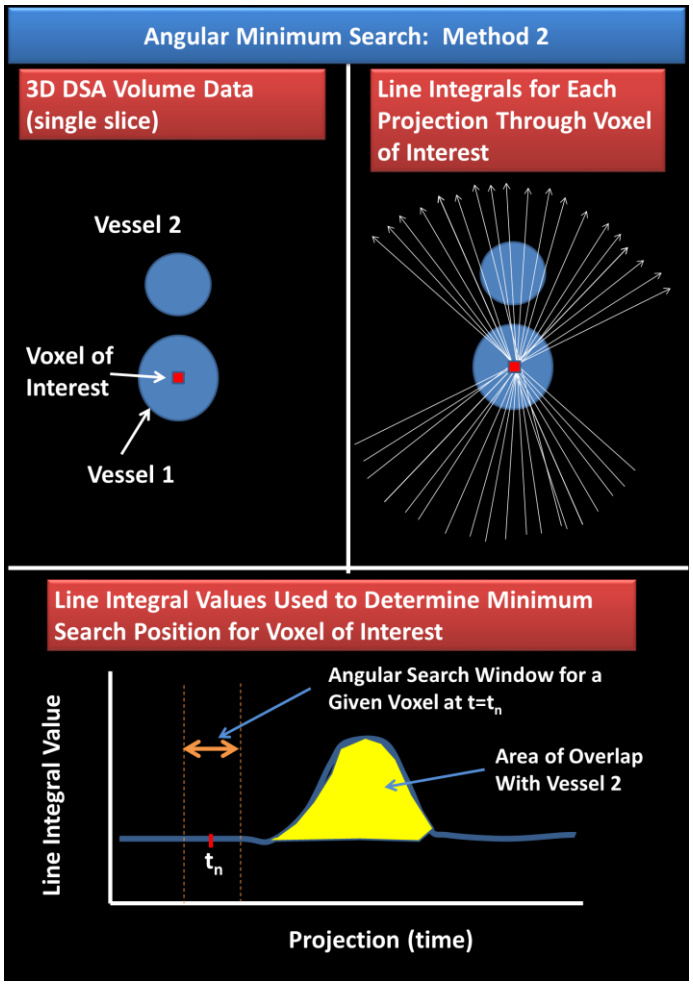

Figure 2-5: Pictorial description of the method 2 search algorithm

2.5 4D DSA Digital Phantom Results

In this section, the results for each of the digital phantom evaluations will be presented separately. For each digital phantom, the following algorithms were compared on a voxel-by-voxel basis with the ground truth values: 4D DSA no local minimum search, 4D DSA local minimum

search 1 with a search angle of ±15°, and 4D DSA local minimum search 2 with a search angle of ±15°. It is important to consider that these results are not intended to serve as a definitive guide as to how to choose the appropriate 4D DSA algorithm, but rather as an example of how the evaluation framework can be used to evaluate new algorithms for defined vascular geometries and flow patterns.

2.5.1 Tube Phantom Results

The tube phantom is designed to test common situations in a simple geometric model. These situations include two overlapping vessels, portions of vessels that are oriented parallel to the rays encoding the temporal information (in certain projection orientations), and non-homogenous cross-sectional filling of an arterial vessel. The tube phantom mimics a straight artery and exhibits fast filling and fast washout of contrast agent.

Figure 2-6: Comparison of ground truth to 4D DSA results by select time frames. a) Ground truth b) 4D DSA no min. search c) 4D DSA with local min search 1 - 15° d) 4D DSA with local min search 2 - 15°

Figure 2-6 shows a volume-rendered comparison (of selected time frames) of the three variants of the 4D DSA algorithm compared to the ground truth from a matching orientation. Visually, compared to the ground truth, the 4D DSA algorithm with no overlap correction (no local minimum angle search) performs better than the other two methods. Since the

tube phantom has little to no overlap, we would expect the method with no overlap correction to yield reasonable results. The local minimum search 1 exhibits delayed filling and early wash-out of contrast agent as a result of the overlap correction technique. The local minimum search 2 algorithm exhibits a very different result from local minimum search 1. Method 2 results in premature enhancement of both the input and the output segments relative to the ground truth. Unlike method 1, method 2 does exhibit a contrast washout that is more similar to the ground truth results. Overall, the 4D DSA method without overlap correction appears to have the best visual results.

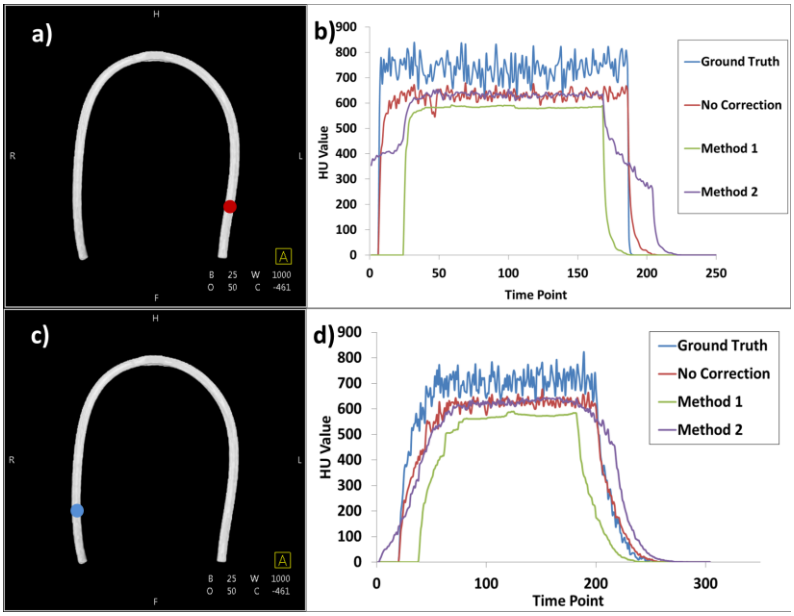

Figure 2-7: a) tube phantom with location of ROI for TCC (red) b) TCC plot for each 4D DSA method c) Tube phantom with location of ROI for TCC plot (blue) d) TCC plot for each 4D DSA method

In order to get an impression of what these TCCs

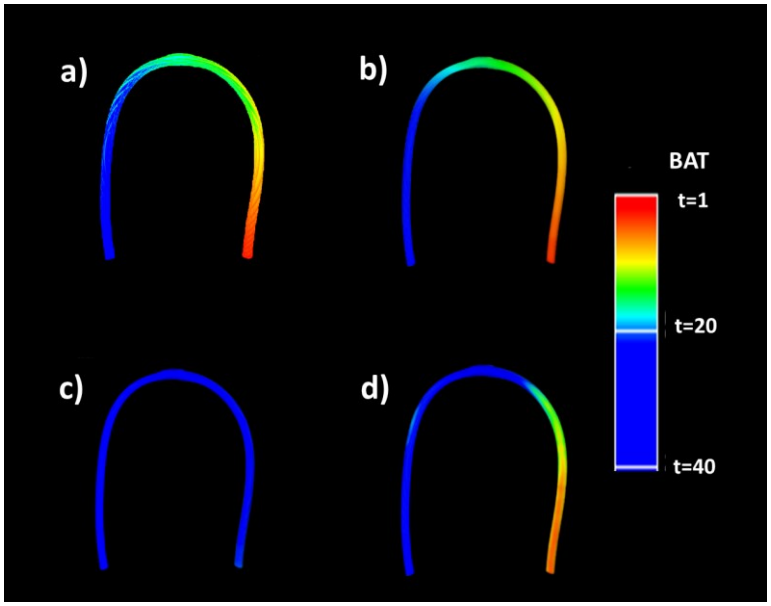

Figure 2-8: A comparison of bolus arrival time (BAT) for: a) ground truth b) 4D DSA no min search c) 4D DSA method 1 - 15° d) 4D DSA method 2 - 15°

look like, we can pick a few locations and plot the TCCs for each method. In the case of the tube phantom, we can plot the TCC for the input and for the output to compare the 4D DSA methods to the ground truth measurements. **Figure 2-7** presents a figure that shows two ROI locations on the tube phantom (a,c) and the corresponding TCCs for those ROIs for the ground truth and the different 4D DSA methods.

Another way to compare the results of the evaluation is to create a parametric color coding of a temporal parameter derived from voxel-based TACs. In this chapter, we will provide the example visualization of the bolus arrival time (BAT). The BAT is calculated as the earliest time point where the attenuation value exceeds one-third of the peak value of the voxel-specific TAC.

Figure 2-8 shows the parametric color coded BAT for the ground truth data and the 4D DSA results for each method. Here the BAT shows the late filling of contrast exhibited by method 1. However, the BAT result for method 2 fail to show the early filling of the input and output that is shown by the time frames in **Figure 2-6**. This is due to the fact that the early enhancement does not cross the threshold of one-third of the peak value, so the BAT does not visually show an early arrival of contrast for these structures. Similar to **Figure 2-6**, the BAT color coding comparison

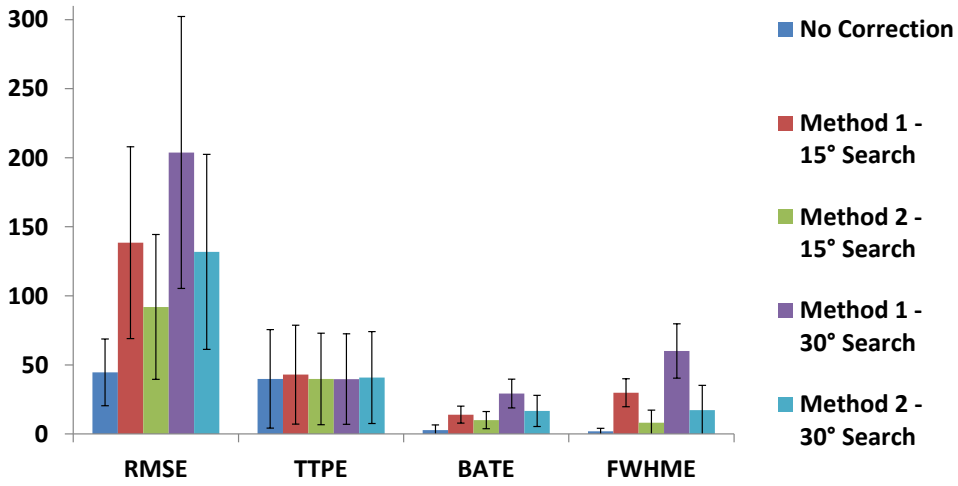

Figure 2-9: Bar graph of the average voxel-wise error of the 4D DSA results for the tube phantom. Root mean squared error (RSME), time to peak error (TTPE), bolus arrival time error (BATE), and full width half maximum error (FWHME) were evaluated for each 4D DSA overlap correction method relative to the ground truth

shows the 4D DSA method without minimum search appears to most closely match the ground truth values.

Using the metrics defined at the beginning of this chapter, a voxel-wise error analysis was performed comparing the ground truth data to the 4D DSA results including no overlap correction, method 1 and method 2 with search angles of 15 and 30 degrees (shown in **Figure 2-9**). The voxel-wise analysis reveals similar results to the visual results shown in **Figure 2-6** and **Figure 2-8**. For this simple digital phantom, the 4D DSA method that does not attempt to correct for overlap yields superior results for all parameters (RMSE, TTPE, BATE, and FWHME) when compared to the results from methods 1 and 2 for overlap correction. This bar graph also shows that increasing the angular search range leads to larger errors for both methods 1 and 2.

2.5.2 Aneurysm Phantom Results

The aneurysm phantom is designed to test common situations with a more complex geometric model. In addition to several of the situations described in the previous example, the aneurysm phantom has an aneurysm with non-uniform filling of contrast agent, more vessels with

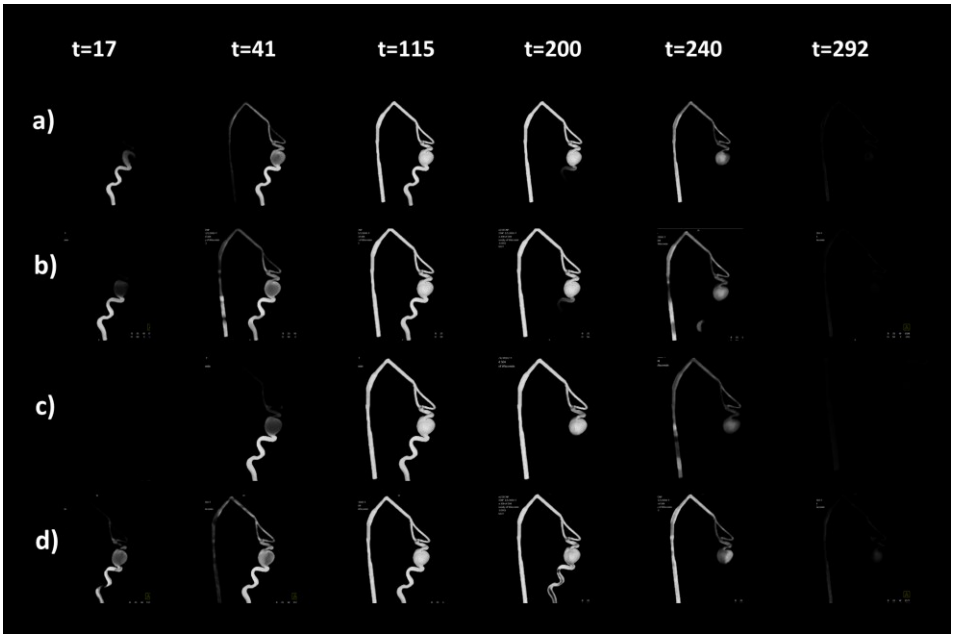

Figure 2-10: Comparison of ground truth to 4D DSA results by select time frames. a) Ground truth b) 4D DSA no min. search c) 4D DSA with local min search 1 - 15° d) 4D DSA with local min search 2 - 15°

more opportunity for overlap occurrences, and it exhibits a more delayed filling venous output (compared to the tube phantom). The aneurysm phantom is based on anatomy derived from a real patient, so this much more closely approximates a real world selective injection of contrast agent into an internal carotid artery.

Figure 2-10 shows a volume-rendered comparison (of selected time frames) of the three variants of the 4D DSA algorithm compared to the ground truth from a matching orientation. Unlike with the tube example, none of the three methods shown precisely match that ground truth time frames. Similar to the previous example, the local minimum search 1 exhibits delayed filling and early wash-out of contrast agent as a result of the overlap correction technique. The local minimum search 2 algorithm exhibits a result that more closely matches the ground truth. Method 2 does exhibit a slower contrast washout compared to the ground truth results (as seen in time frame 200).

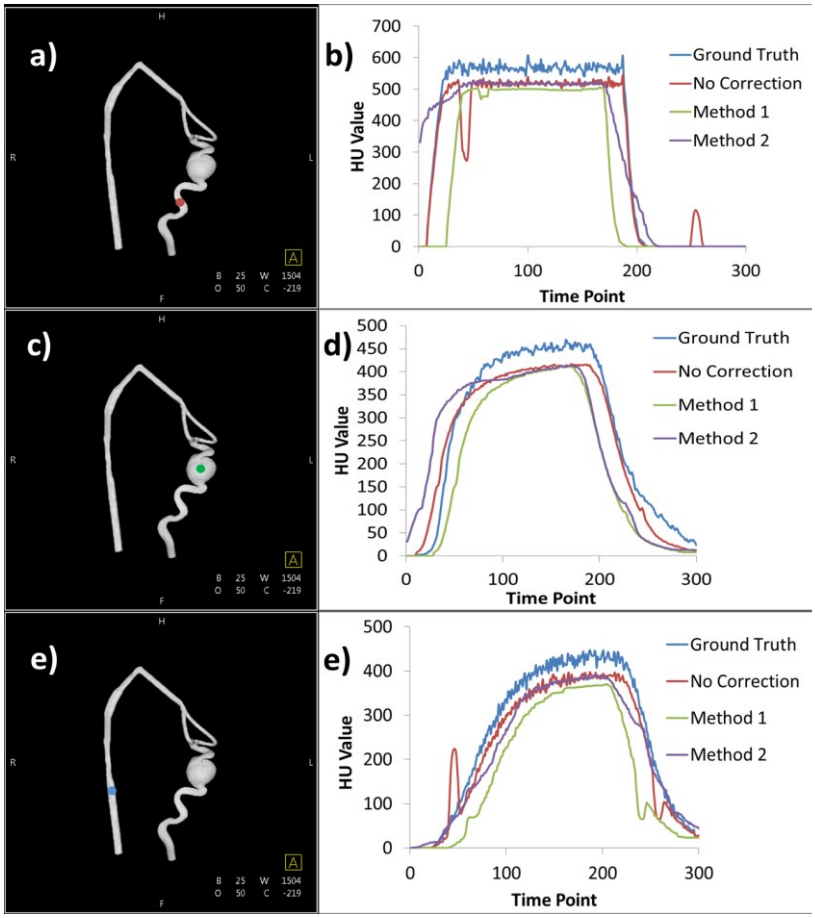

Figure 2-11: a) Aneurysm phantom with arterial location of ROI for TCC (red) b) Arterial TCC plot for each 4D DSA method c) Aneurysm phantom with aneurysm location of ROI for TCC plot (green) d) Aneurysm TCC plot for each 4D DSA method e) Aneurysm phantom with venous location of ROI for TCC f) Venous TCC plot for each 4D DSA method

For the aneurysm model case, **Figure 2-11** shows an example of three ROI locations that are defined in the artery, the aneurysm, and the vein (output) of the phantom model. TCCs for each 4D DSA method and the ground truth are plotted for each ROI location.

Figure 2-12 shows the parametric color coded BAT for the ground truth data and the 4D DSA results for each method. Here we can see that the 4D DSA without overlap correction shows an earlier arrival of contrast in the vein relative to the ground truth due to the overlap of the artery with the vein in the early time frames. As seen in the tube example, method 1 shows a later arrival of contrast relative to the ground truth, but does appear to correct the early filling vein. Method 2 also does a better job of correcting the early filling vein shown in the implementation without overlap correction. However, there are irregularities visualized in all of the vessels that exhibit non-smooth transitions of BAT for neighboring voxels.

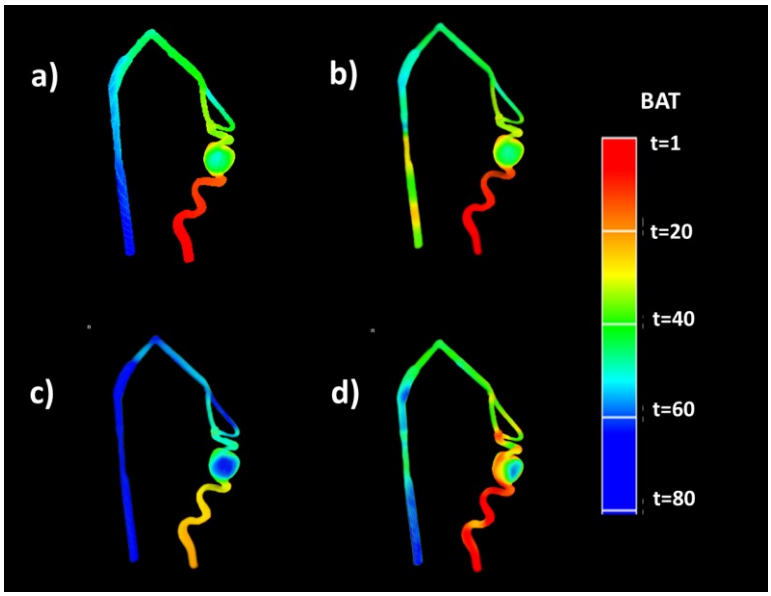

Figure 2-12: A comparison of bolus arrival time (BAT) for: a) ground truth b) 4D DSA no min search c) 4D DSA method I - 15° d) 4D DSA method 2 - 15°

Figure 2-13 shows a bar graph of the voxel-wise error analysis for the aneurysm digital phantom. Similar to the tube phantom results, it is clear that when considering the global error across all voxels, the 4D DSA result that does not include overlap correction outperforms both methods 1 and 2 for all parameters. Also, the cumulative error for methods 1 and 2 increase as the search angle increases from 15 to 30 degrees, further indicating that larger search angles do not lead to improvements in the 4D DSA results. However, the visual frames shown in **Figure 2-10** also need to be considered when evaluating the 4D DSA results in order to provide a comprehensive evaluation. For certain anatomical segments of the phantom, the overlap methods do appear to provide "more" correct visual order of filling (giving the window center and width) compared to the 4D DSA methods without overlap correction.

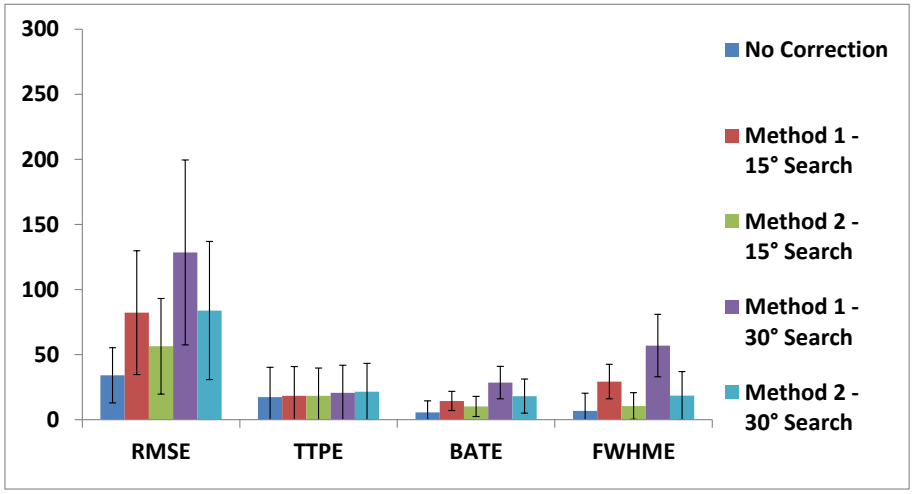

Figure 2-13: Bar graph of the average voxel-wise error of the 4D DSA results of the aneurysm phantom. Root mean squared error (RSME), time to peak error (TTPE), bolus arrival time error (BATE), and full width half maximum error (FWHME) were evaluated for each 4D DSA overlap method relative to the ground truth

2.5.3 Anterior and Posterior Cerebral Circulation Phantom Results

The anterior and posterior circulation phantom is designed to model the most complex arterial anatomy. Similar to a contrast injection into a peripheral vein or into the aortic root, this model is designed to simulate the simultaneous enhancement of all four major cerebral arterial vessels, the Circle of Willis, and the first and second order middle cerebral and anterior cerebral vessels. This complex phantom is based on anatomy derived from a real patient, so it closely approximates the main arterial anterior and posterior cerebral anatomy for humans.

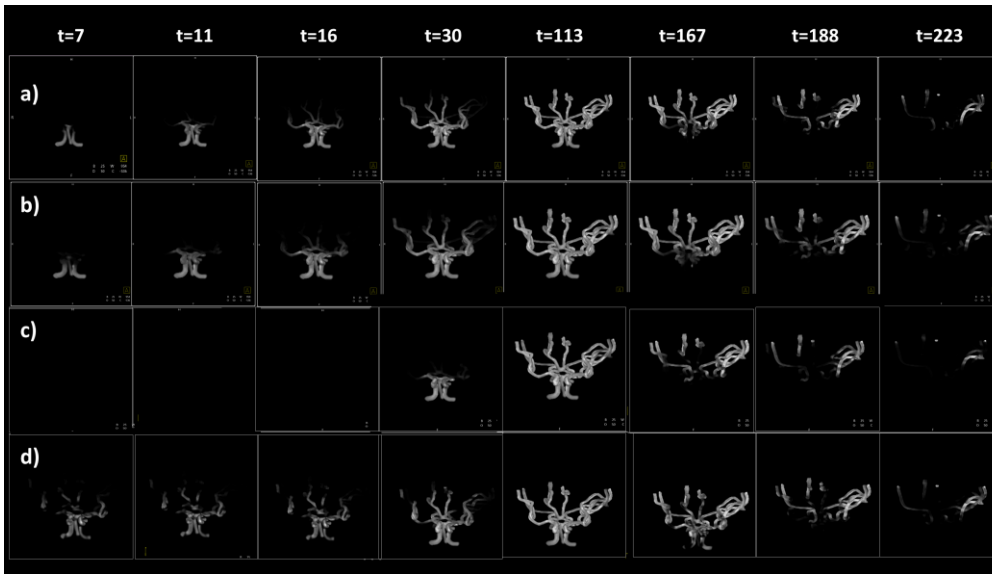

Figure 2-14: Comparison of ground truth to 4D DSA results by select time frames. a) Ground truth b) 4D DSA no min. search c) 4D DSA with local min search 1 - 15° d) 4D DSA with local min search 2 - 15°

Figure 2-14 shows a volume-rendered comparison (of selected time frames) of the three variations of the 4D DSA algorithm compared to the ground truth from a matching orientation. Similar to the aneurysm model, none of the three methods shown precisely match that ground truth time frames, however the algorithm with no overlap correction most closely matches the ground truth. The local minimum search 1 exhibits delayed bolus arrival, fast filling of the vasculature in a very short amount of time, and early wash-out of contrast agent as a result of the overlap correction technique. The local minimum search 2 algorithm results in early and somewhat erratic filling, which does not appear to be correct when compared against the ground truth.

Figure 2-15 shows the parametric color coded BAT for the ground truth data and the 4D DSA results for each method. Here we can see that the 4D DSA without overlap correction compares favorably to the ground truth. Method 1 clearly shows a later arrival of contrast relative to the ground truth, but does appear to be filling correctly (proximal to distal). Method 2 clearly shows the erratic filling and spatio-temporal discontinuities that are introduced by this method's overlap correction.

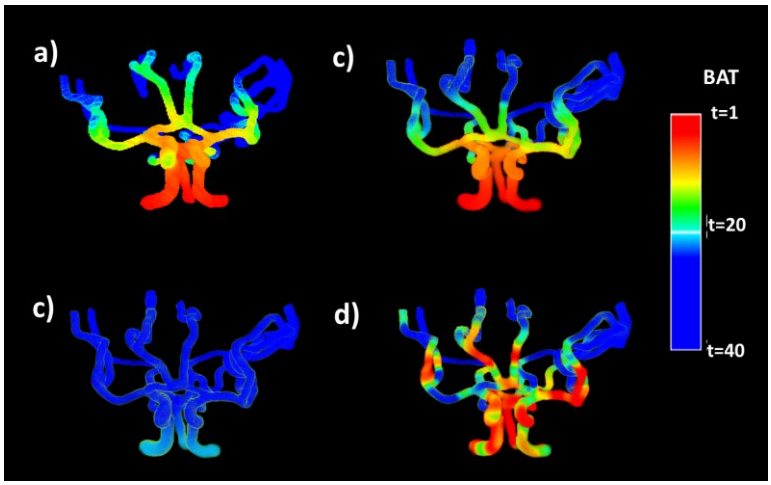

Figure 2-15: A comparison of bolus arrival time (BAT) for: a) ground truth b) 4D DSA no min search c) 4D DSA method I - 15° d) 4D DSA method 2 - 15°

Figure 2-16 shows a bar graph of the voxel-wise error analysis for the anterior and posterior cerebral circulation digital phantom. Similar to the tube phantom results, it is clear that when considering the global error across all voxels, the 4D DSA result that does not include overlap correction outperforms both

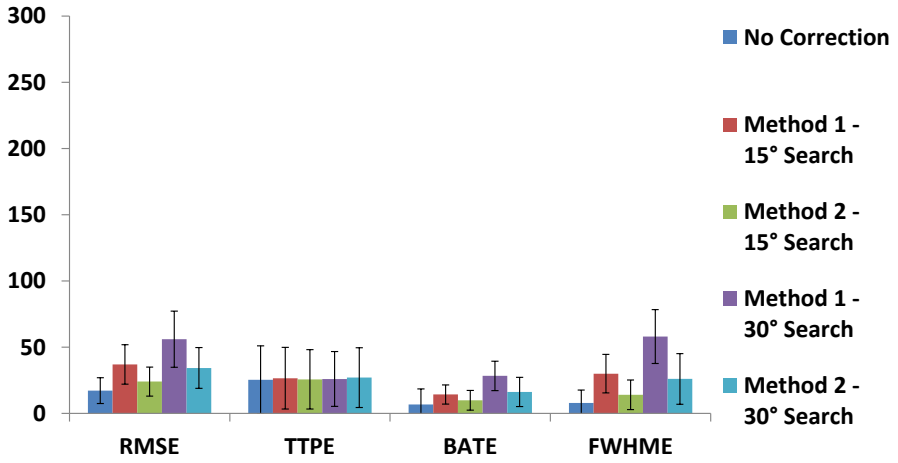

Figure 2-16: Bar graph of the average voxel-wise error of the 4D DSA results of the anterior and posterior circulation phantom. Root mean squared error (RSME), time to peak error (TTPE), bolus arrival time error (BATE), and full width half maximum error (FWHME) were evaluated for each 4D DSA overlap method relative to the ground truth

methods 1 and 2 for all parameters. Also, the cumulative error for methods 1 and 2 increase as the search angle increases from 15 to 30 degrees, further indicating that larger search angles do not lead to improved 4D DSA results. While method 2 outperforms method 1 in terms of statistical error (by the metrics defined in this work), it is visually clear that method 1 does a better job of retaining the temporal filling characteristics of the blood vessels, as method 1 is primarily shifted in time. For this reason, the visual frames shown in **Figure 2-14** also need to be considered when evaluating the 4D DSA results in order to provide a comprehensive evaluation.

2.6 Discussion

Based on this results it is clear that both Method 1 and Method 2 sometime provide improved results, and often times lead to worst results than having no overlap correction. In order to gain some intuition as to where these methods can fall short, it is helpful to look at a few simple pictorial examples that can illustrate some of the situations that are likely occurring in the phantom studies.

2.6.1 Case 1: Single Vessel Center Voxel

The simplest case to evaluate first is one where there is a single vessel and no overlap, evaluating the values encoded to the center voxel. In this case, there is no overlap issue, and in principle, the best overlap correction result should be the same result as if no overlap correction was performed.

Figure 2-17 shows an example of a single vessel cross-section. In this case we will interrogate the center voxel of the vessel cross-section. On the upper-right side of the figure is the ground truth value for that voxel. In the lower left and lower right images are the intermediate plots of the time-series of values that are used for the search method 1 (left) and method 2 (right). The left side represents the measured projection value assigned to that voxel. For no overlap, this essentially is the same as the ground truth (assuming no scaling inaccuracies). On the right side (method 2), the straight line represents the constant value of the line integral through the 3D DSA volume for each projection step. Since the vessel here is assumed to be perfectly round and the voxel is in the center of the vessel, this value will be a constant for all projections.

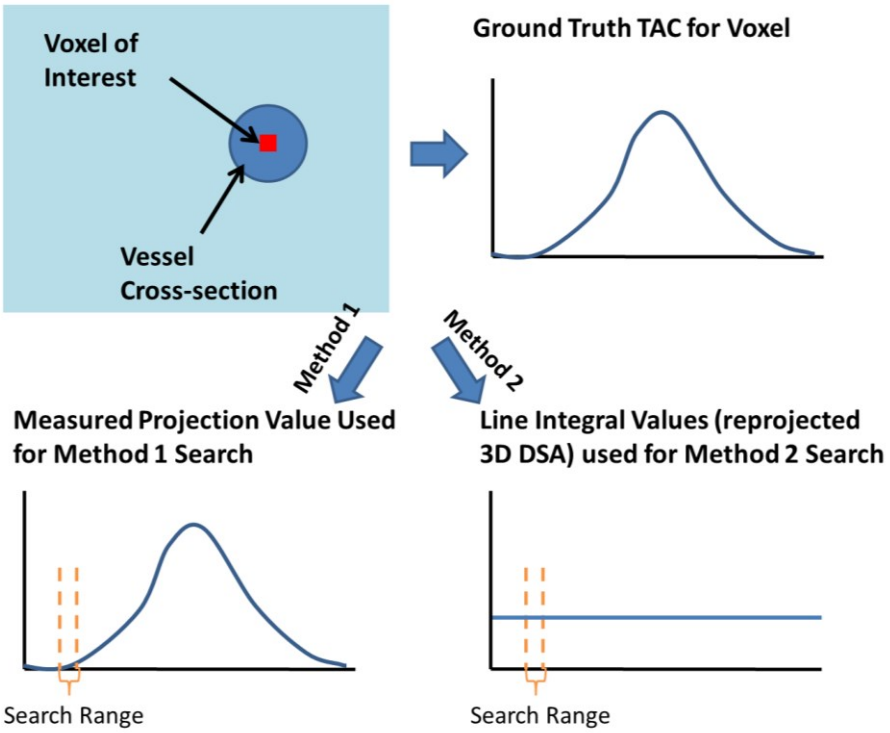

Figure 2-17: Case 1. Single vessel with no overlapping vessels comparing intermediate steps for angular search methods 1 and 2

Once this intermediate data is generated, the search range (as shown in orange brackets) is applied for each time point for the given voxel, where the minimum value within the orange brackets is always selected for use as the current time point's value. Method 1 results in always using values on the left-most end of the bracket for rising slopes and on the right-most side of the bracket for falling slopes. Since method 2 yielded a constant line, the minimum search always yields the same time point as the current time point, since it is the closest minimum value. The results are shown in **Figure 2-18**. The result for method 1 is consistent with what we see in the digital phantom studies that were investigated in this chapter. Method 1 yields a delayed filling (proportional to the size of the min search range) and an early washout (also proportional to the size of the search range). Method 2 performs as desired in this case.

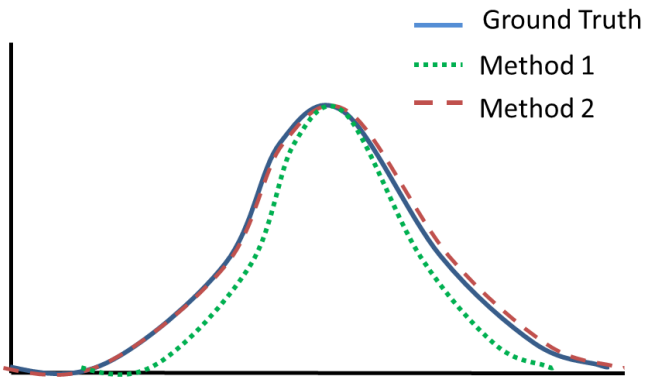

Figure 2-18: Results for case 1. In this case, method 1 yields inferior results compared to method 2.

2.6.2 Case 2: Single Vessel Center Voxel with Pulsatile Flow

Although pulsatile flow was not simulated in this work, it is important to discuss the impact of the minimum search methods in the case of pulsatile or even irregular flow patterns. In practice, the use of selective injections of contrast agent often result in time curves that are influenced by non-enhanced blood mixing entering regions with enhanced blood, either by flow from the same vessel, or through collateral pathways. Therefore, it is important to show a simple case where flow curves with pulsatile characteristics is evaluated using both method 1 and method 2. **Figure 2-19** shows a simple

case with a single vessel and a voxel of interest that is at the center of the vessel. The ground truth waveform (as shown in the upper-right) shows a TCC waveform that is typical of a selective injection in to an artery with high blood flow rates. The lower left image shows the intermediate data that is used to calculate the minimum for method 1. On the lower right is the intermediate data used to calculate the minimum value for method 2 (search range shown in orange for both methods).

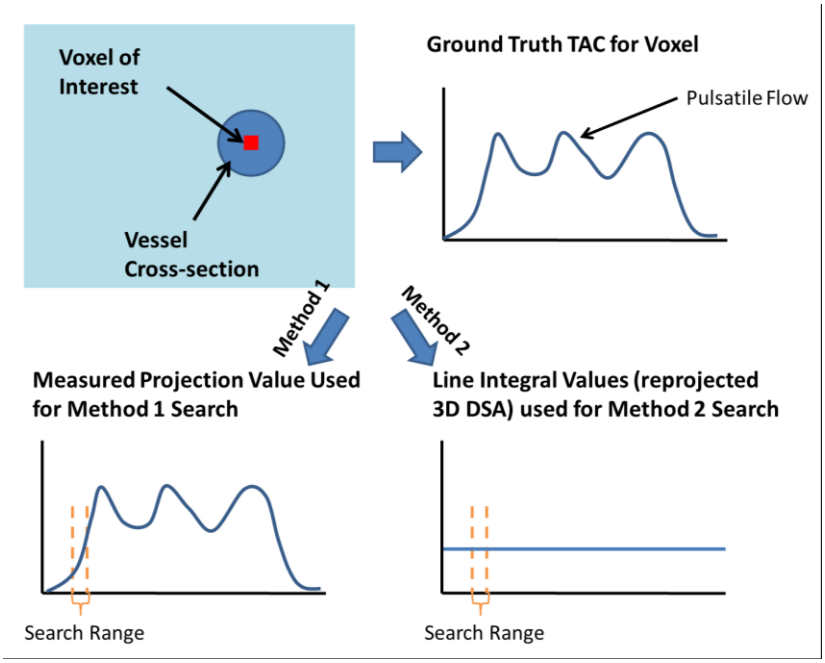

Figure 2-19: Case 2. Evaluation of method 1 and method 2 for a pulsatile waveform

The results follow closely what happens in case 1 for both methods. For method 1, the minimum search finds local minimum always on the left side of an upward slope (backwards in time) and the right side (forward in time). This leads to the same behavior seen in case 1 where the contrast washes in late and washes out early. However, depending on the size of the search range and the frequency of the pulsation, method

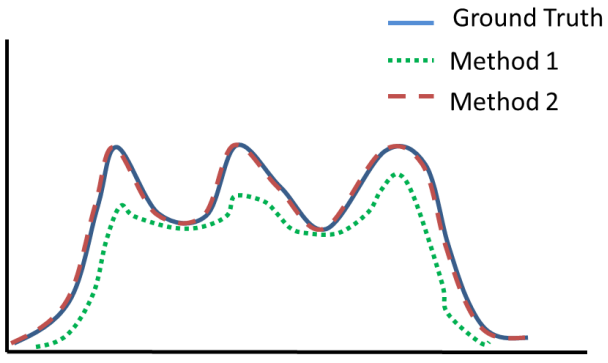

Figure 2-20: Results for case 2. In this case, method 1 yields inferior results compared to method 2.

1 can severely dampen or even completely remove the pulsations in the results. Method 2 yields similar results to case 1. Since there is no geometric overlap occurring in this case, the intermediate data is a constant value and therefore the value for each time point is used. **Figure 2-20** illustrates the results of method 1 and method 2. As you can, for this case method 2 leads to superior results since it is not based on the measured time curve.

2.6.3 Case 3: Single Vessel with Off-Center Voxel

In cases 1 and 2, only the center voxel was considered for the minimum search result. However, it is necessary to consider off-center voxels as well, since these make up the majority of the vascular voxels in a 3D DSA image. **Figure 2-21** shows an illustration of this example. The upper left portion depicts a vessel cross-section with the voxel of interest located near the edge of the vessel. The upper right shows a standard time curve. The lower left shows the intermediate data for method 1 and the lower right shows the intermediate data for method 2. It is clear that method 1 performs as seen in cases 1 and 2. However, method 2 no longer has a constant value, but rather a periodically changing value that is dependent on the orientation of the projection ray through the vessel. As the projection data is

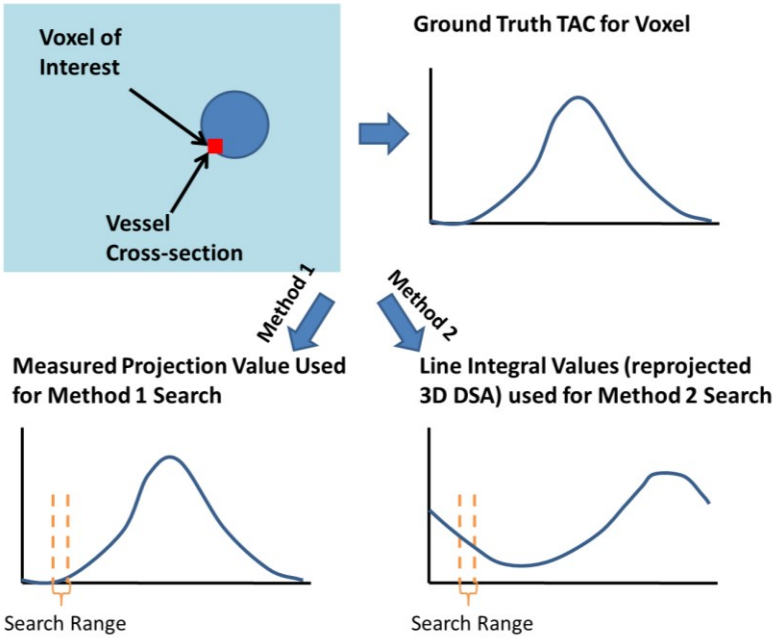

Figure 2-21: Case 3. Evaluation of method 1 and method 2 for an off-center voxel

acquired from different view orientations, the length of the vessel it passes through changes as a function of this view angle.

The results of both methods are shown in **Figure 2-22**. In this case neither method is obviously superior to the other, as each of them result in significant deviations from the ground truth. However, the result for method 2 appears more erratic and could prove to be less realistic to the clinician evaluating the images.

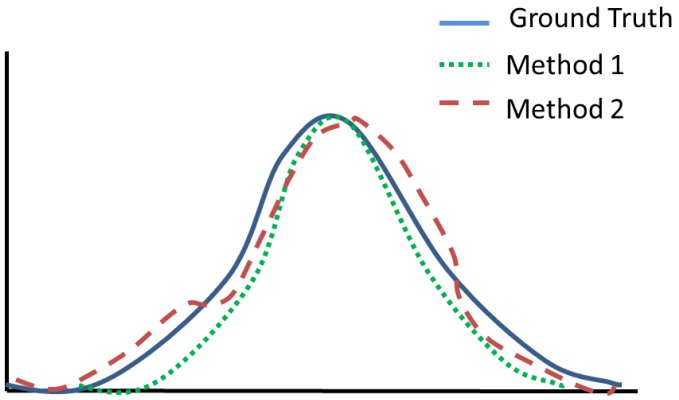

Figure 2-22: Results for case 3. In this case both method 1 and method 2 result in significant error.

2.6.4 Case 4: Two Vessels with Center Voxel

Finally, it is important to evaluate a case where overlap is occurring between two vessels. In this case, we will examine two overlapping vessels where one vessel enhances early (vessel 1) and the other enhances later (vessel

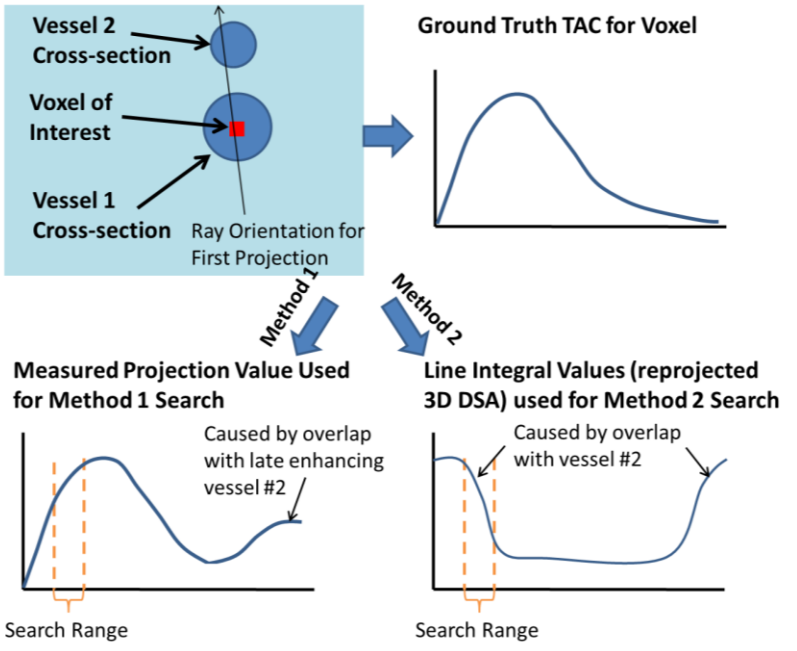

Figure 2-23: Case 4. Two vessels with overlap during the first view projections.

2), similar to a late filling vein. **Figure 2-23** provides an illustration of this case. The upper left shows the two vessels, the voxel of interest, and the orientation of the initial view ray that result in overlap during the early acquired projections. The top right shows the ground truth time curve for the voxel location. The lower left shows the intermediate data used for method 1. Notice that the overlap with the late filling vein causes a rise at the end of the time curve (relative to the ground truth). The lower right shows the intermediate data used for method 2. Here we see the vessel overlap issue at both the beginning and end of the intermediate data curve, with a constant value in between.

Figure 2-24 shows an illustration of the results for case 4. Similar to the other cases, method 1 results in a delayed wash-in of contrast and an early washout of contrast. Method 2 results in the opposite where the wash-in of contrast appears early (right from the first time point). This occurs as a result of the first projection orientation overlapping vessel 1 and vessel 2. As a result, the minimum search for method 2 moves to the very right of the search range (forward in time) for the early time points in an overlap situation. This results in the contrast arriving early. This is a very similar situation to the results that were shown for the Tube Phantom experiments.

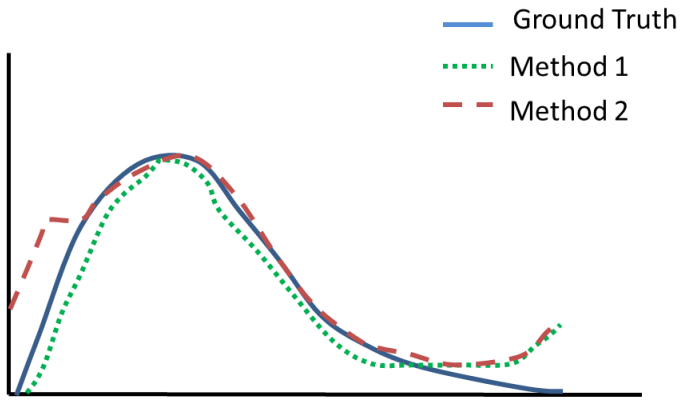

Figure 2-24: Results for case 4. Both method 1 and method 2 have errors, however, method 1 yields superior results for the wash-in of the bolus

2.7 Conclusion

This chapter introduces basic methods and a framework intended to be used as a development and evaluation tool for the 4D DSA algorithm and proposed overlap correction methods. The use of sophisticated digital phantoms derived from human anatomical models and flow characteristics allow for a better understanding of the performance of the algorithm in real-world situations. Further, having a set of increasingly complex phantoms allows for a better understanding of how robust these methods are across a diverse range of anatomical situations.

There are a few important points that were learned from this basic evaluation comparing overlap correction method 1 and method 2. First, for most cases, using no overlap correction outperforms the overlap correction when considering the accuracy of all voxel time-curves. Second, method 1 results in a greater amount of error than method 2. However, the error introduced in method 1 appears to be more predictable and better preserve the relative flow dynamics. Third, increasing the size of the minimum search range leads to increasing amounts of error. Finally, both method 1 and method 2 are applied indiscriminatingly to all voxels at every time point and consequently introduce error for time points that do not suffer from overlap issues. The results for both methods would greatly improve if the overlap correction was only applied to time points that specifically suffer from overlap situations. Future research should be aimed at developing these modified correction algorithms.

Chapter 3: Metric for Image Sparsity and Improved Methods for Vessel Overlap Detection

3.1 Introduction

The previous chapter demonstrates that 4D DSA can be very accurate for simple anatomical situations where there is little to no overlap between vascular structures along a projection ray. This is frequently referred to as having a "sparse" vascular anatomy. However, as the vascular anatomy becomes increasingly complex and less "sparse", the number of overlapping vascular structures in the measured projection increases. This situation leads to an increasingly underdetermined system of unknown vessel voxel time attenuation (TAC) values $V(X,t)$ (where X represents the 3D voxel location) relative to our measured projection values $P\,(U,t)$, where U represents 2D coordinates in the coordinate system for the measured projection at time t. The 4D DSA algorithm uses the local minimum search technique (described in Chapter 1 and an alternative implementation described in Chapter 2) to calculate corrected $V(X,t)$ values for vessel overlap situations. Regardless of the approach, as the incidence of vessel overlap increases, the more difficult the problem becomes to recover the correct TAC values.

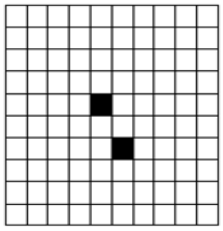

Figure 3-1: A simple 10x10 matrix with 100 elements is shown. 2 of the elements are non-zero, representing a sparsity of 2/100 or 2%

Currently, there is no accepted method or metric used to evaluate and characterize the complexity of a given 3D DSA dataset for use in generating 4D DSA results. Literature related to the topic of undersampled signal recovery commonly refers to these datasets as having a necessary level (or amount) of sparsity[7], [42]. In this case, they are defining sparsity as a vector with very few non-zero elements relative to the total size of the vector. **Figure 3-1** provides a simple example of the traditional metric associated with data sparsity. In this example, a 10x10 matrix of elements (100 total elements) is shown where only 2 of the elements are non-zero. This results in a metric value of 2/100 or 2% non-zero elements. Increasing the number of elements (or in the case of 4D DSA, blood vessels) will decrease the sparsity of the 3D DSA volume (which serves as the constraint for the 4D DSA algorithm), lead to an increased number of overlap occurrences for 4D DSA, and potentially reduce the accuracy of the 4D DSA result. However, the classic definition of sparsity for the 3D DSA volume is not sufficient to predict the results of the 4D DSA algorithm alone. Due to the projection geometry of the C-arm CT, the spatial locations and distributions of the vessels also plays a significant factor in the accuracy of the 4D DSA results. **Figure 3-2** and **Figure 3-3** provide a simple example to illustrate this point.

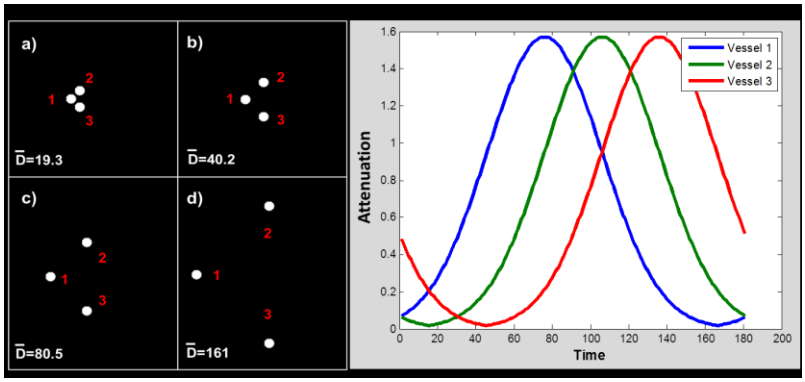

Figure 3-2: Left: Simple 3 vessel phantom model with increasing distance between the 3 vessels (a,b,c,d). Right: TAC curve functions assigned to each of the 3 vessels.

Figure 3-2 shows a cross-sectional slice of a simple digital phantom with three vessel cross sections. The average distance between the vessels was increased by approximately a factor of two (**Figure 3-2 a-d**) to create four different scenarios. It is important to note that each scenario exhibits

the same image sparsity as defined by the number of non-zero voxels, since we did not change the size, shape or number of vessel cross-sections. Only the positions of the vessels have changed. Each vessel was assigned a unique TAC as shown in the right pane of **Figure 3-2**. Using a forward projection step, this data can then be used to generate measured projection data, which can then in turn be used to generate 4D DSA results. For the purposes of this paper, we will use a basic 4D DSA algorithm without the local minimum search in order to reduce the complexity. In this chapter, we will not implement a method for vessel overlap correction in this work in order to best establish an initial correlation between the metric and 4D DSA results. **Figure 3-3** shows the results of the basic 4D DSA algorithm with no overlap correction (green) for increasing distance between vessels compared to the ground truth (blue).

This simple example clearly shows that the accuracy of the 4D DSA results are influenced not only by the number vessels present, but also by the spatial locations of these vessels. This chapter outlines the development of the vessel overlap sparsity index (VOSI) metric that is capable of more accurately predicting the accuracy of the 4D DSA results (given specific anatomy) when compared to traditional sparsity measurements. The VOSI metric can be used to characterize the complexity of a given dataset and offer guidance as to when 4D DSA algorithms can accurately be applied for clinical cases where the ground truth is not known. The VOSI metric will also provide

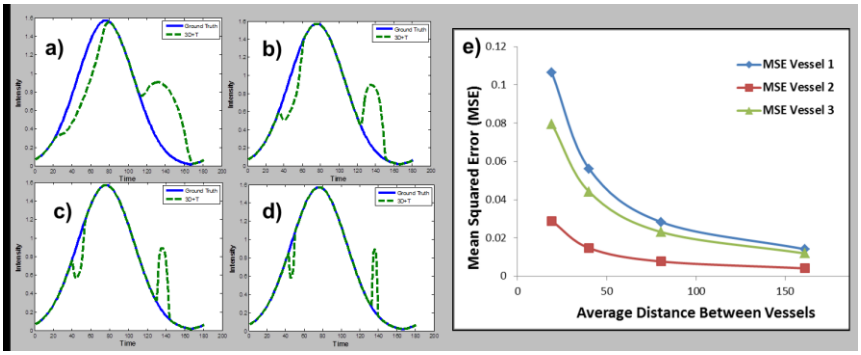

Figure 3-3: Left: Vessel location #1 3D+T TAC results (green-dashed line) for increasing average distance between vessels compared to ground truth (blue line) (a-d). Right: Mean Squared Error plots for each vessel as a function of average distance between vessels.

a data-dependent metric by which 4D DSA implementations can be compared for their ability to accurately recover TAC information for cases of a known VOSI metric value.

3.2 Methods and Materials

3.2.1 2D Slice Digital Phantom Design

In order to support the initial development of the VOSI metric, two series of 2D digital phantom slices were developed. While we will focus on 2D slice data for this chapter, it is straightforward to extend this concept to incorporate the full z-axis series of slices (3D volume). The first series of phantom slices consist of 3 different slices, each with an increasing number of simulated vessel cross sections with a uniform diameter. The simplest of these consist of a single vessel, with the most complex slice having 10 vessels as shown in **Figure 3-4**. The locations of the vessels are randomly selected for each slice, with the constraint that no vessel may overlap with another vessel in the slice plane. The second series of phantom slices also consisted of 3 slices, each with a decreasing radius within which a constant number of vessels (n=10) are randomly distributed relative to the total field of view (FOV) of the slice. In other words, the spatial distribution of 10 vessels is increasing confined to a decreasing area of the slice, thus increasing the spatial density of the vessel locations. Again, the constraint of no overlapping or touching vessels in the slice plane is applied to the generation of these datasets. The radius deceased from 75% of the

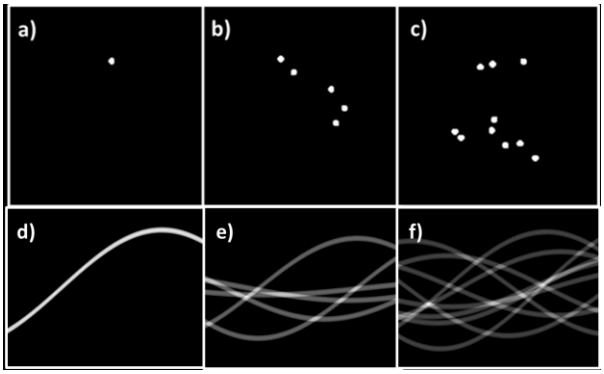

Figure 3-4: a-c, example digital phantom slices with increasing number of randomly placed vessels (1, 5, and 10 vessels). **d-f,** sinogram visualization for 2D slices (1, 5, and 10 vessels respectively)

total FOV to 35% of the FOV in steps of 20%. **Figure 3-5** illustrates an example of the 2D slices (a-c) and corresponding sinograms (d-f) for this digital phantom with decreasing FOV. The goal of this phantom is to understand the effects of vessel spatial distribution on 4D DSA results.

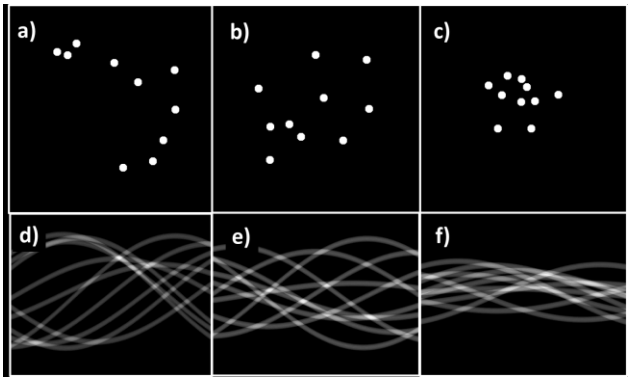

Figure 3-5: **a-c**, example digital phantom slices with decreasing FOV constraint for 10 randomly placed vessels (75%, 55%, 35%). **d-f**, sinogram visualization for 2D slices (75%, 55%, 35%)

For the purposes of this initial work, all calculations were performed using simulated rotational acquisitions with parallel ray geometry using Matlab R2013a (The Mathworks, Inc., Matick, MA). This technique can be extended to support fan beam and cone beam geometry as applicable.

3.2.2 Methods for Generation of Ground Truth Datasets

For each digital phantom slice dataset, voxels that define a unique vessel within the slice were identified and then assigned a randomly generated TAC to represent the time-varying contrast kinetics for that particular vessel. A total number of 180 time steps were used for all TACs. The TAC curve was modeled as a Gaussian distribution in time with a randomly assigned standard deviation (σ) within the interval [-11, 11] time points and with a randomly assigned shift in time within the interval of [-45, 45] time steps. The TACs were assigned to each vascular voxel in a given 2D slice. The resulting dataset represents the ground truth data that will be used to evaluate the accuracy of the 3D+T result.

Once the time-resolved ground truth voxel data is generated, each time step can then be forward projected at each angular step size to generate a series of time-varying projections that range from [0°, 179°] using an angular step size of 1°. This projection data represents the measured projection values that will be used as input to the 3D+T algorithm. **Figure 3-6** demonstrates an example of this time-varying projection data. **Figure 3-6a** shows the sinogram of the static 3D slice after reprojection. **Figure 3-6b** shows the sinogram of the ground truth 3D+T digital phantom after the reprojection of each time step.

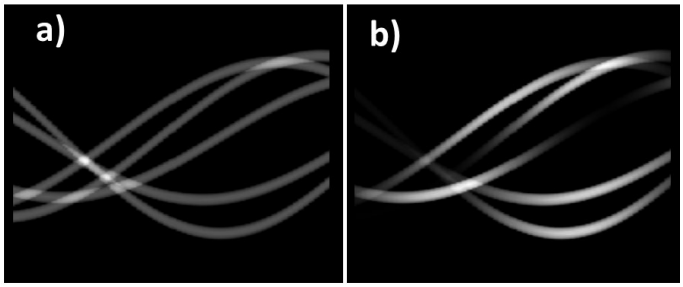

Figure 3-6: a) Sinogram of constraint 3D data (single slice). b) Sinogram of time-varying projections based on the ground truth phantom

3.2.3 Vessel Number Area Histogram

The VOSI metric is motivated by the concept of the dose volume histogram commonly used in radiation therapy[43]. The previous chapter illustrates how the 4D DSA reconstruction accuracy is strongly related to the degree of overlap of vessels within a projection data set. The VOSI metric measures the percent of the sinogram in which vessels can be uniquely detected (non-overlapped). **Figure 3-7** provides a simple example of this concept. **Figure 3-7a** shows 2D slice with a total of 10 vessel cross-sections, which are counted explicitly and used as *a priori* knowledge. This is also the case for a standard 4D DSA acquisition, since we know the static 3D DSA prior to the 4D DSA encoding. **Figure 3-7b** displays the corresponding sinogram for **Figure 3-7a** after reprojection. For each view angle in the sinogram, a determination was made of how many unique vessels can be distinguished. A unique vessel was defined as one or more nonzero values bordered by zero values. In the case of

vessel overlap, two or more vessels will be counted in the sinogram as a single nonzero series of values for a given view angle and therefore considered as a single vessel. I want to thank and acknowledge Brian Davis (University of Wisconsin, Department of Biomedical Engineering) for providing the inspiration and original concepts for vessel overlap detection in the sinogram domain. **Figure 3-7c** is a plot of the number of detected vessels as a function of view angle. **Figure 3-7d** is a plot of the vessel number area histogram. This histogram plots the percent of the sinogram view angles where the number of detected vessels is higher than a given vessel number (x-axis). The VOSI metric is then calculated as the ratio of the area under the curve of the vessel number area histogram to the ideal vessel number area histogram. The area under an ideal vessel number area histogram (where all vessels are detected correctly) is calculated as 100% multiplied by the number of vessels in each slice (x-axis). The known vessel number cannot be determined from the sinogram (due to the vessel overlap). Instead, this was calculated from the actual image slice using connected components analysis. In practice, the known vessel number can easily be determined from the segmentation of an *a priori* 3D DSA image volume.

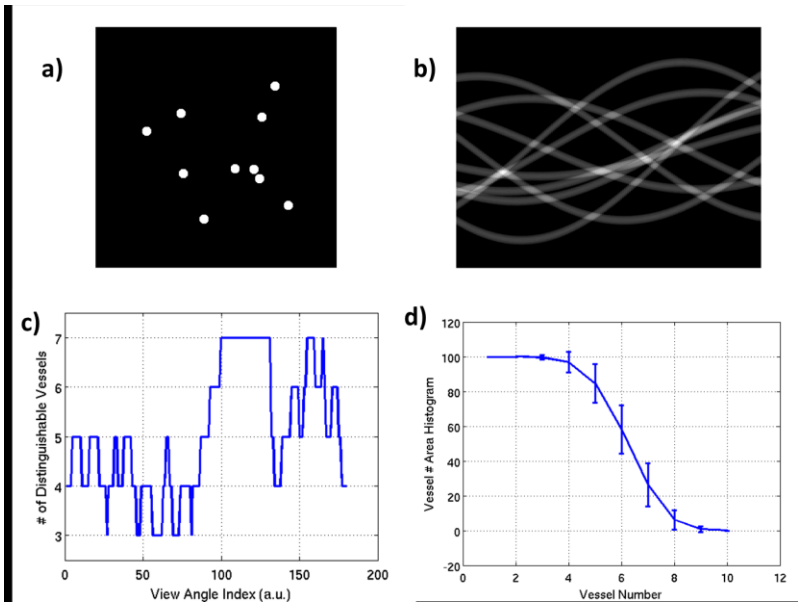

Figure 3-7: a) Vessel phantom (n=10). b) Sinogram of (a). c) Vessel detection as a function of view angle. d) Vessel number area histogram

3.2.4 Methods for Evaluation of 4D DSA Results

At this point, the original static slice data (*a priori* 3D DSA volume) and the measured time-varying projections can then be used as input to the 4D DSA algorithm. The results of the 4D DSA algorithm can then be compared to the original ground truth data using a mean squared error (MSE) analysis, similar to the analysis performed in the previous chapter. **Figure 3-8** shows an example of a time frame from the ground truth data (**Figure 3-8a**), the 4D DSA result at the same time frame (**Figure 3-8b**), and the residual comparison image (**Figure 3-8c**). The MSE was calculated across all time points for each vessel. For each slice, the average MSE was then calculated across all vessels, providing a composite MSE value for each 2D vessel phantom slice configuration. This composite MSE value can then be used to evaluate the performance of the VOSI metric compared to the 4D DSA algorithm results. In order to establish a large sample size of simulation results, each series of phantoms (increasing vessel number and decreasing FOV) were generated and evaluated for 30 unique vessel position instances. Results were averaged across the 30 instances and the performance of the VOSI metric was compared to the MSE of the 4D DSA results.

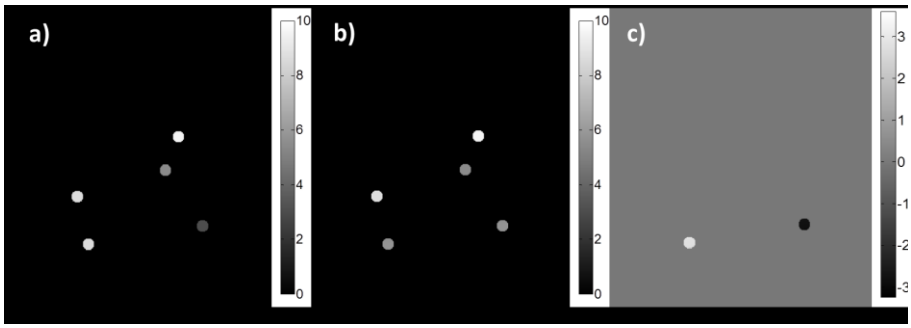

Figure 3-8: a) Ground truth slice for t=179. b) 4D DSA result for t=179. c) Residual comparison image used to calculate MSE

3.3 Results

The results across the two series of phantoms (increasing vessel number and decreasing FOV) show the VOSI metric was inversely correlated to the MSE results of the 4D DSA simulations.

Figure 3-9 provides a graphical representation of the MSE and VOSI results as a function of vessel number (**Figure 3-9a**) and FOV constraint (**Figure 3-9b**). Both **Figure 3-9a** and **Figure 3-9b** demonstrate a close inverse relationship between the VOSI metric and the MSE results of the 4D DSA calculations. **Figure 3-9c** and **Figure 3-9d** plot the same relationship substituting sparsity for the VOSI metric. **Figure 3-9c** shows a strong correlation between sparsity and the MSE results for increasing vessel number. However, **Figure 3-9d** demonstrates the failure of the sparsity metric to correlate with MSE results. **Figure 3-10a** and **Figure 3-10b** show scatter plots of the VOSI versus MSE metric for all simulation data points (n=90) for the vessel number and FOV series respectively.

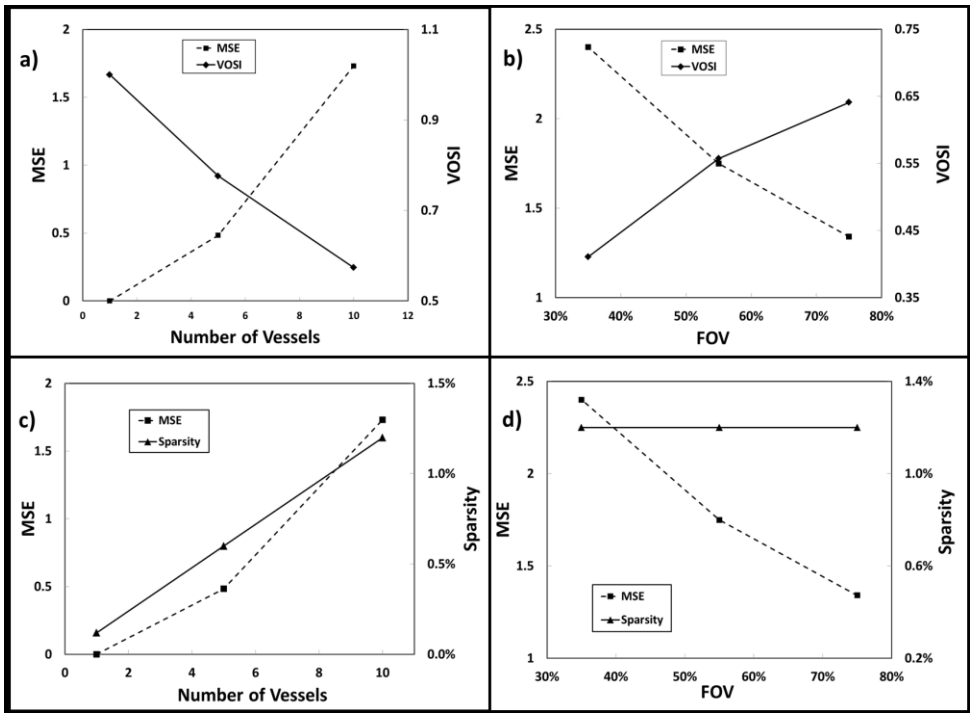

Figure 3-9: a) Plot of MSE as a function of vessel number compared with VOSI metric as a function of vessel number. b) Plot of MSE as a function of FOV compared with VOSI metric as a function of FOV. c-d) Results of sparsity metric substituted for VOSI.

The Pearson correlation coefficient (for VOSI vs. MSE) was calculated for each series (increasing vessel number and FOV) and also demonstrates a strong inverse correlation (r=-0.91, p<0.01 and r=-0.78, p<0.01 respectively), further confirming the results shown in **Figure 3-9** and **Figure 3-10** for the VOSI metric. Similarly, the Pearson correlation coefficient was also calculated for sparsity versus MSE, confirming a strong correlation between sparsity and MSE for vessel number, but no correlation for changes in FOV (r=0.90, p<0.01 and r=0,p=1 respectively).

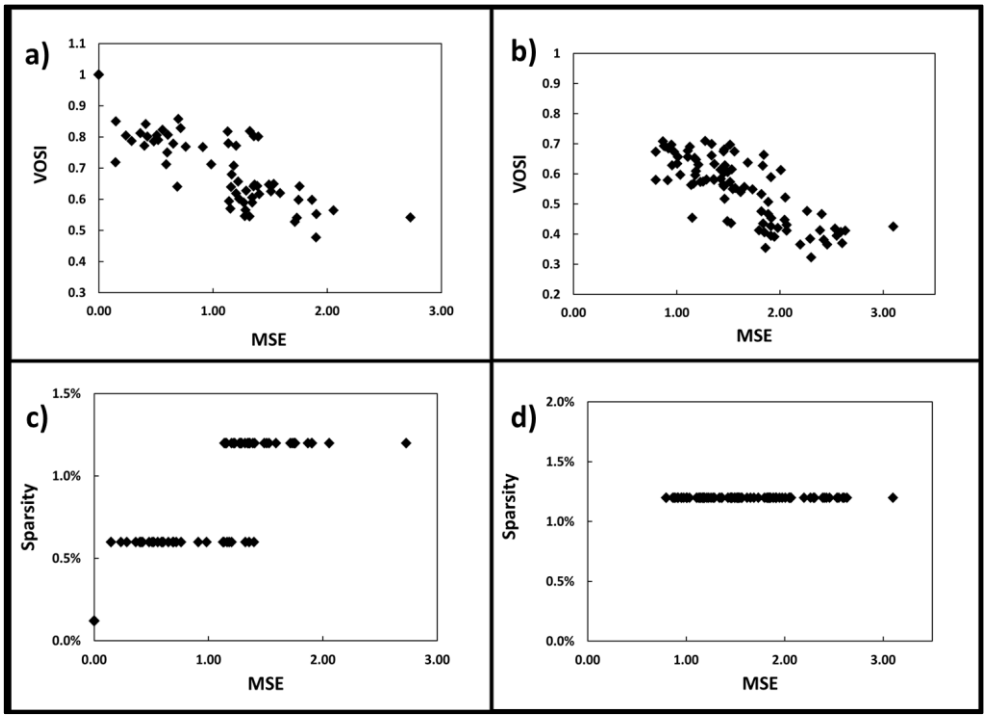

Figure 3-10: a) Scatter plot of VOSI vs MSE for vessel number series (n=90). b) Scatter plot of VOSI vs MSE for FOV series (n=90). c) Scatter plot of sparsity vs MSE for vessel number series. d) Scatter plot of sparsity vs MSE for FOV series.

When examining a fully volumetric dataset, the VOSI metric can be examined as a function of slice number (or z-axis position) as shown in **Figure 3-11a-c**. In this case, the VOSI metric can be used to identify the areas within a 3D volume that are most likely to have vessel overlap that will impact the 4D DSA results. In order to further enhance the presentation of the VOSI metric, the composite VOSI value can be encoded back into the volumetric 3D DSA data and presented in a color-coded manner as show in **Figure 3-11d** and **Figure 3-11e**. Alternatively, a composite VOSI score can be assigned to a given 3D DSA volume. In these cases, it is suggested to weight the composite VOSI metric to a percentage of the lowest total VOSI scores of the slices. Future work will be aimed at developing guidelines for establishing the composite VOSI metric.

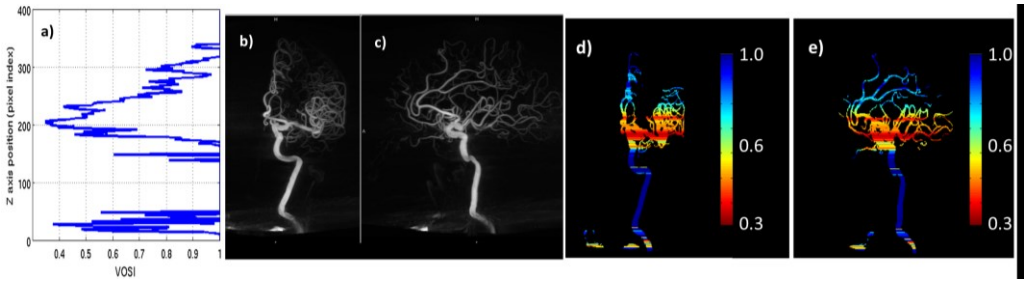

Figure 3-11: a) Plot of VOSI metric as a function of z-axis position. b) Anterior view of 3D DSA aligned with 10a to demostrate the anatomical regions with highest overlap issues. c) Lateral view of 3D DSA also aligned to 10a d) color-coded VOSI metric assigned to 3D voxels in anterior and e) lateral orientations

3.4 Summary

In summary, the VOSI metric demonstrates a very strong inverse correlation with 4D DSA results for vessel phantoms of various complexities. In practice the VOSI metric can be used classify the complexity of given datasets for use with 4D DSA algorithms. As shown in this work the VOSI metric can be used to predict the performance of a 4D DSA algorithm that does not include corrections for vessel overlap. In practice, 4D DSA algorithms that include overlap correction techniques can be evaluated against phantoms of varying VOSI scores in order establish a baseline in

which to judge the performance of the overlap correction. In other words, for a dataset with a given VOSI value, the MSE error associated with a given 4D DSA algorithm can be estimated and compared with other approaches. For example, the digital phantoms described in the previous chapter (and future versions) can be assigned a VOSI score such that there is a common understanding of how the complexity of each phantom compares to the others. This can be used to guide the digital phantom selection when trying to evaluate specific changes to the 4D DSA algorithm overlap detection.

Finally, VOSI color maps (as shown in **Figure 3-11d)** can also be interpreted as a type of confidence map. Areas with a low VOSI value can be visually shown in a color (such as red) to draw attention to areas where the 4D DSA may have less accuracy. This could potentially guide the clinician in understanding what areas they can be confident in the results of the algorithm.

3.5 Future Work

Building on what was learned from the VOSI metric and the validation results, we know that error can be introduced into the 4D DSA reconstruction as a result of overlap with vessels that are in-plane along the same ray given a specific view angle projection. One intermediate step of the VOSI calculation is to generate a view-angle specific count of the number of identified vessels. Knowing the true number of vessels, we can determine if that particular view angle suffers from vessel overlap. However, this does not provide information on exactly which vessels are overlapping, only that overlap exists.

3.5.1 Explicit Overlap Detection and Correction

One method for determining the vessel overlap is to use a ray-driven vessel counter, much like a forward projection. This approach can be voxel driven and explicitly count the number of vessels along a given ray defined by the system geometry. Once the number of vessels along the ray is known, overlap correction techniques (such as the angular minimum search) can then be used only to correct only those time points where explicit vascular overlap is occurring, rather than indiscriminately being applied to all time points. **Figure 3-12a** shows a sinogram with overlapping vessels. Using a vessel counter along the projection ray, the number of vessels can be mapped to the same sinogram to illustrate exactly which spatio-temporal locations exhibit vessel overlap. The result is shown in **Figure 3-12b.** Pixel values greater than 1 indicate where vessel overlap situations occur. This value can be backprojected into the 3D domain in order to have voxel and time-specific information, which could be used to optimize when angular search methods are applied to the reconstruction. Future work will focus on refining this method.

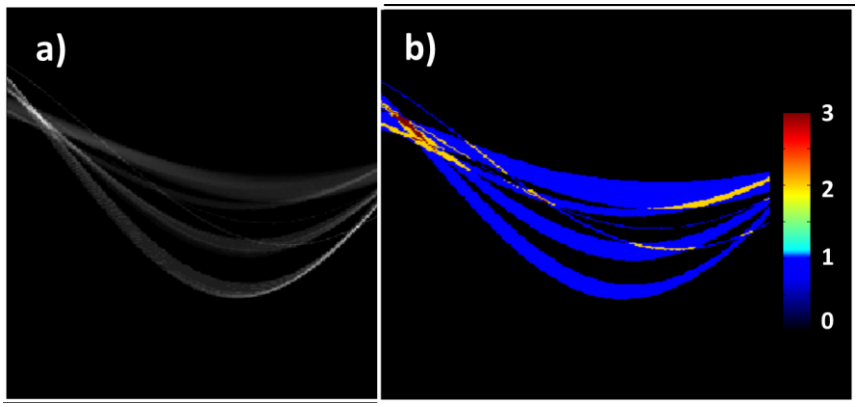

Figure 3-12: a) sinogram of measured projection data b) sinogram of vessel counts along the projection ray, color coded to show where overlap situations occur (values > 1 define overlap)

Chapter 4: Acquisition Protocols for 4D DSA

4.1 Preliminary 4D DSA Acquisition Methods using Standard Commercial 3D Protocols

Modern C-arm angiography systems typically are equipped with one or more acquisition protocols dedicated to rotational angiography (3D DSA). As a clinical example, the Siemens Artis zee biplane system that is installed in the University of Wisconsin's interventional neuroradiology department has two factory installed acquisition options for 3D DSA. **Table** 4-1: Summary of standard **3D DSA acquisition** protocols for Siemens Artis zee biplane system

summarizes the two factory-installed acquisition programs.

	5s DSA	10s DSA
Angular Scan Range	200°	200°
# of Projections per Rotation	133	248
Angular Step per Projection	1.5°/projection	0.8°/projection
Scan duration	4.6 seconds	9 seconds
Dose per Frame (Automatic Exposure Control)	High-dose – 1.20 μGy/F Low-dose – 0.36 μGy/F	High-dose – 1.20 μGy/F Low-dose – 0.36 μGy/F

Table 4-1: Summary of standard 3D DSA acquisition protocols for Siemens Artis zee biplane system

These commercial acquisition protocols are designed to provide two options for subtracted contrast-enhanced 3D reconstructions. The 5s DSA scan protocol is designed for pure high contrast vascular imaging of early-filling arterial structures such as aneurysms and AVMs. The 10s DSA protocol, with its slower gantry rotation and larger number of acquired projections, is designed to provide better visualization of distal arteries and early-venous structures while still providing the same early and mid-phase arterial visualization provided by the 5s DSA protocol.

A typical injection protocol for a 3D DSA rotation involves an injection of contrast agent (sometimes diluted with saline) directly through a catheter selectively placed in the artery of interest. A power injector is synchronized with the C-arm system, such that after the first mask rotational acquisition is acquired, the injector is triggered to inject contrast agent in synchronization with the second (fill) rotational acquisition. For projection-based CT imaging, it is important that structures be uniformly enhanced through all of the acquired projections in order to obtain a filtered backprojection-based reconstruction that does not suffer from data inconsistency artifacts[44], [45]. For this reason, an x-ray delay on the order of 1-2 seconds is typically programmed into the system such that the injection begins 1-2 seconds prior to the start of the second acquisition, allowing time for the important arterial structures to be fully enhanced prior to the acquisition.

4.2 Preliminary 4D DSA Results Using Standard Protocols

The following sections demonstrate some of the early clinical 4D DSA imaging results that were obtained using the standard commercial 3D DSA protocols described in **Table 4-1**. Injection timing differed in delay time and duration between the two acquisition types, and is described in detail below.

4.2.1 Preliminary 5s DSA Acquisition Results

The 5 second DSA protocol acquires 133 projections over a 200 degree range in approximately 4.5 seconds. This results in an angular acquisition rate of 1.5 degrees/frame with an approximate frame rate of just less than 30 frames per second. As a result, the timing for the injection has little margin for error. In order to make sure that the main arterial vessels were adequately filled for the majority of the projections, a 1 second x-ray delay time was used. A standard injection rate of 2.5 ml/s was used for the internal carotid location with undiluted contrast agent. The injection was carried out for 6 seconds of total length to cover the total length of the scan. This injection protocol reflects a typical injection protocol used for basic 3D DSA imaging of the internal carotid territory.

Using the 4D DSA reconstruction process outlined in Chapter 1, results were generated and visually compared with the original projection data at matching time points. **Figure 4-1** shows an example of a large aneurysm originating from the internal carotid artery segment. The grayscale images in the top row show the first, middle, and ending subtracted projections that were acquired as part of the rotational acquisition. The bottom row shows the corresponding 4D DSA reconstruction results at the same time and view orientation as the original projections shown directly above them.

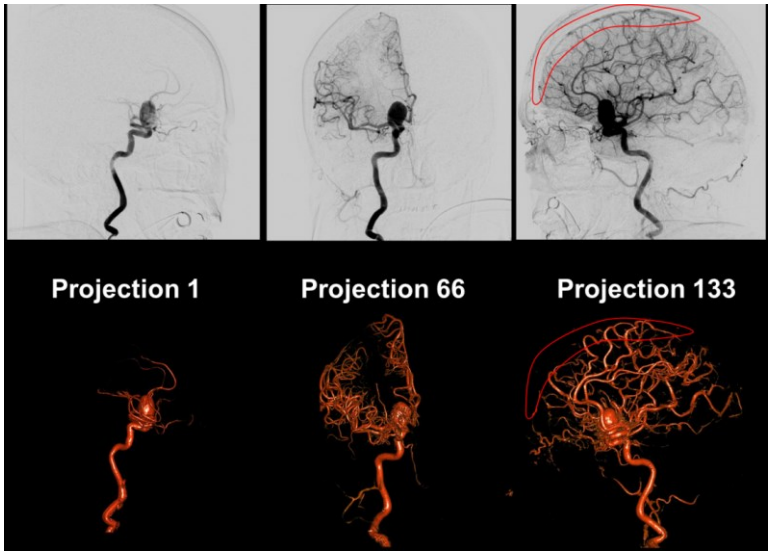

Figure 4-1: Rotational 2D subtracted projections of 5s DSA acquisition (top row) and corresponding 4D DSA time frames shown at matching orientations (bottom row)

As a result of the relatively short scan time of the 5s DSA acquisition, several limitations are imposed on the final 4D DSA result. Traditionally, an x-ray delay is used in conjunction with the contrast injection to allow time for the major arterial structures to enhance prior to the start of the x-ray acquisitions. While this delay improves the data consistency (and ultimately the 3D DSA reconstruction accuracy), it prevents the visualization of the earliest phase of the bolus in the 4D DSA result, since the x-ray measurement does not begin until after portions of the vessel are already enhanced. Removing this delay can result in increased artifacts in the reconstruction such as streaks or geometric inaccuracies of vascular structures. Another major drawback is the lack of venous structures that are captured in the projections, the 3D DSA constraining image, and the 4D DSA reconstruction. The red outline shown in **Figure 4-1** highlights the fact that the sagittal sinus structure only just begins to fill during the final projections acquired during the 5s DSA acquisition. As a result, the sagittal sinus is not reconstructed in the constraint 3D DSA volume, and consequently is also not recovered in the 4D DSA volume (lower right image) for the final time frames (also highlighted by the red outline in **Figure 4-1**).

While the 5s DSA protocol will likely not be useful for seeing the full transit of the contrast agent through the arterial, capillary, and venous phases, it potentially can be useful for looking at early filling arterial structures where most of the key anatomical structures are enhanced within the first few seconds of the injection. High flow vascular malformations such as high grade AVMs and arteriovenous fistulas (AVFs) may be appropriate pathologies to image with this protocol, as these structures often enhance immediately after delivery of the contrast agent.

4.2.2 Preliminary 10s DSA Acquisition Results

In order to try and capture late filling arterial, capillary, and venous structures, it is necessary to extend the length of the acquisition such that these anatomic structures are enhanced in the acquired projections and will be accurately reconstructed in the 3D DSA constraining volume. The 10s DSA scan is the longest standard DSA acquisition protocol available on the commercial Siemens Artis zee biplane system. One advantage of using a longer duration scan protocol is that it allows for the potential to start the injection later such that the arrival of bolus can be fully captured in the early projections. A second potential benefit of the longer scan is that it may be possible to stop the bolus prior to the end of the scan such that the washout or trailing edge of the bolus can be visualized in the final projections. Lastly, the longer scan duration should offer the ability to reconstruct more late-filling anatomical structures than the shorter 5s DSA protocol. **Figure 4-2** shows preliminary results from a 10s DSA acquisition, where the grayscale subtracted projections are shown in the top row and the reconstructed 4D DSA volumes are shown in the bottom row. The results clearly show that the longer acquisition captures more of the small arteries and early venous structures that the 5s DSA acquisition failed to capture. The red arrows in the figure show the venous structures such as the sagittal sinus, the transverse sinus, and the jugular vein. The earlier filling sagittal sinus and transverse sinus were visualized well in the projections and were partially captured in the 4D DSA reconstruction. The later filling sigmoid sinus and jugular venous structures are not well visualized compared to the 2D DSA. Clearly the longer duration

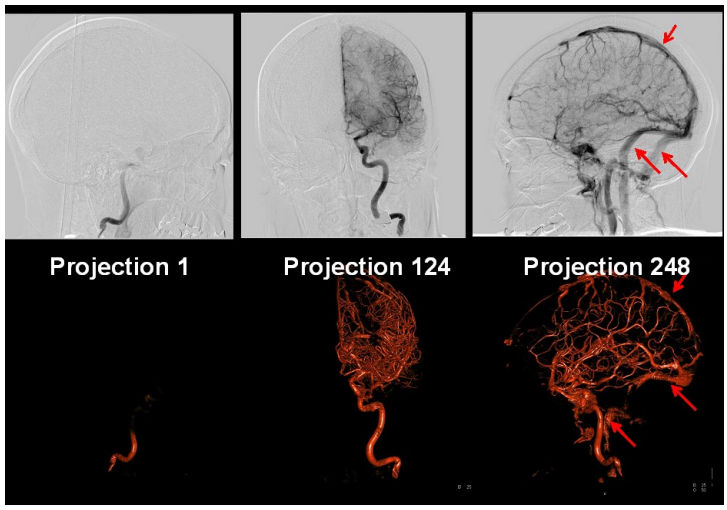

Figure 4-2: Rotational 2D subtracted projections of the 10s DSA acquisition (top row) and corresponding 4D DSA time frames shown at matching orientations (bottom row)

acquisition was able to provide more information than the shorter 5s DSA scan, and research is warranted to determine if even longer acquisition scans can provide superior results without significantly increasing the radiation dose.

4.3 Challenges and Limitations with Commercial 3D DSA Acquisitions for 4D DSA

4.3.1 Insufficient 3D DSA Scan Duration

As discussed in earlier in this chapter, the currently available 3D DSA protocols are limited to maximum acquisition durations of 10 seconds. Preliminary results show that for patients with relatively normal circulation times, small veins do not significantly enhance until approximately 5 seconds after the start of the injection and large veins do not significantly enhance until almost 6.5 seconds after the start of the injection. Published work by Lin et al. reinforces our observations, reporting that small veins reach peak enhancement approximately 4.83±0.93 seconds and large veins as long as 6.51±1.1 seconds from the injection for their control (normal) cohort of patients[46].

The longest 3D DSA acquisition protocol available is approximately 10 seconds in duration, indicating that fewer than half of the projections acquired would have enhancing venous structures. This results in poor 3D image quality for early and late filling venous structures in the 3D DSA constraining volume (as demonstrated in **Figure 4-1** and **Figure 4-2**) resulting in limited 4D DSA visualization of these structures.

4.3.2 Geometric Artifacts from Data Inconsistencies in the Acquired Projections

Commercially available C-arm CT 3D DSA protocols are limited to having a single "mask" acquisition that contains no contrast agent and a single "fill" rotation that contains contrast-enhanced vessels that can be subtracted and then filtered and backprojected (typically a FDK-based reconstruction algorithm[47]) to create a 3D angiographic volume of vascular data. Traditional rotational angiography techniques require that the vessels of interest must be enhanced in all of the projection views at a consistent attenuation level in order to have accurate 3D reconstruction of the data[48], [49]. Failure to fulfill this angular data consistency requirement results in inaccurate 3D reconstructions of the sparse anatomical structures[44]. In order to demonstrate these artifacts, a basic digital phantom experiment was performed using the high contrast detail of the Shepp-Logan phantom and a simulated parallel ray geometry reconstruction based on the MATLAB iradon and radon transforms. Beginning with the full 180 degrees of projections for the standard reconstruction, each subsequent reconstruction used an increasingly smaller subset of data to simulate this data inconsistency issue. **Figure 4-3** provides an example of the types of artifacts that arise in the 3D reconstruction as a result of not having consistent contrast enhancement of a vascular structure throughout all projections. This example demonstrates the geometric artifacts become visually significant once inconsistent enhancement occurs in greater than 15-20% of the projections. This concept presents challenges in

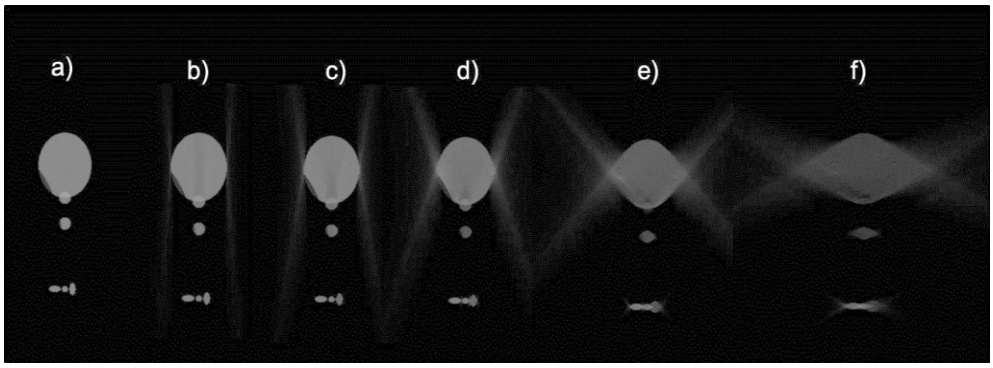

Figure 4-3: Geometric reconstruction artifacts due to inadequate number of projections with contrast enhancement: a) 180 degrees of consistent data b) 170 degrees of consistent data c) 160 degrees d) 140 degrees e) 120 degrees f) 100 degrees.

particular for large veins that have neither fully nor consistently enhanced (due to non-iodinated blood from other vascular inputs) in a significant number of projections when using our existing acquisition protocols combined with an intra-arterial injection of contrast agent. This data inconsistency already exists with standard 3D DSA imaging protocols, however, to date, 3D DSA imaging protocols are rarely used to image more than just early enhancing arterial structures or arterialized venous structures, so these artifacts typically do not impair the diagnostic accuracy of these specific segments.

Conversely, the 4D DSA acquisition and injection protocols are designed to create vascular dynamics throughout the entire course of the acquisition such that temporal information about the vascular filling can be encoded back into the 3D DSA constraining image. These two principles compete against each other, and a compromise for both temporal dynamics and 3D reconstruction accuracy must be met if 4D DSA will always be derived from a single rotational 3D DSA acquisition and injection. Since the 4D DSA data is derived from the 3D DSA reconstruction, the image quality of the 4D DSA reconstruction will suffer from many of the artifacts that are in the 3D DSA constraining volume. Further research will be conducted to learn how to minimize the geometric artifacts in the 3D DSA volume that can be introduced by data inconsistency without impacting the ability of the 4D DSA algorithm to encode the temporal filling patterns of the vascular structures.

4.4 Experimental Acquisition Protocols for 4D DSA

In order to address the issues described in the previous sections, new scan protocols were devised that are focused on improving data inconsistency artifacts and expand the temporal coverage of the acquisition. The Siemens biplane angiography has specific mechanical and architectural limitations that impact the design of these protocols. Specifically, the floor stand C-arm plane (plane A), which is used for acquiring the 3D projection data, is limited in the angular range, the rotational

velocity of the C-arm, the readout rate of the detector, and the maximum number of projections that can be acquired and processed for a single rotational angiography scan. Of these limitations, the maximal angular range and the memory limitations for the total number of projections impact the 4D DSA most significantly. The maximal angular range for the C-arm acquisition plane is 260 degrees (starting at 130 degrees RAO and rotating to 130 degrees LAO). Due to memory limitations of the 3D image processing pipeline, the maximum number of projections allowed for a rotational acquisition (mask and fill rotation combined) is 610 projections at a matrix size of 1280x960, which represents the standard brain 3D DSA readout (where the detector is operating in a 2x2 binning mode of adjacent detector elements). Based on these system limitations, modifications to the 5s DSA and 10s DSA protocols were made to create two new experimental acquisition protocols that are summarized in **Table 4-2**.

	6s DSA	**12s DSA**
Angular Scan Range	260°	260°
# of Projections per Rotation	172	304
Angular Step per Projection	1.5°/projection	0.85°/projection
Scan duration	6.1 seconds	12 seconds
Dose per Frame (Automatic Exposure Control)	0.36 μGy/F	0.36 μGy/F

Table 4-2: Summary of experimental 3D DSA acquisition protocols for Siemens Artis zee biplane system

4.4.1 Temporal Duration for Experimental 4D DSA Acquisitions

One primary modification to the existing commercial 5s and 10s DSA protocols was performed in order to extend the time duration of these two protocols. By extending the duration of the scan and acquiring a large angular sampling range, this allows for the ability to increase the amount contrast dynamics in the scan, but still result in a high-quality 3D DSA volume. This modification consisted of an extension of the 3D DSA scan range from 200 degrees to the maximal allowable angular range of 260 degrees. By adding an additional 60 degrees of scan range, the effective duration for both the 5s and 10s scans can be extended by approximately 1.5 and 2.5 seconds respectively. This resulted in two new experimental protocols that were named "6s DSA" and "12s DSA" to indicate their change from the original 5s and 10s DSA commercial protocols.

Unfortunately, simply extending the 10s DSA acquisition from 200 degrees to 260 degrees angular range was not possible (at the same angular sampling interval) due to system memory limitations that prevented more than 610 projections to be acquired for the combination of mask and fill. A slight modification to the 12 DSA protocol was made to account for this by changing the angular step size from 0.80°/frame (standard with the 10s DSA protocol) to a larger step size of 0.85°/frame, resulting in a total of 608 total projections. This larger angular step size does limit the extension of the temporal duration over the 10s DSA to only an additional 2.5 seconds.

4.4.2 Data Consistency Improvements using Experimental 4D DSA Acquisitions

Another advantage offered by the 260 degree protocols is the possibility of starting the injection simultaneous with the start of the fill acquisition scan (in order to capture the inflow of contrast agent) without significantly increasing the data consistency artifacts that would be introduced in the standard 5s DSA product acquisition. The standard product 3D acquisitions are typically limited to 200 degrees (180 degrees plus the fan angle), which satisfies only the minimum angular sampling criteria for accurate FDK reconstruction of a cone beam geometry.

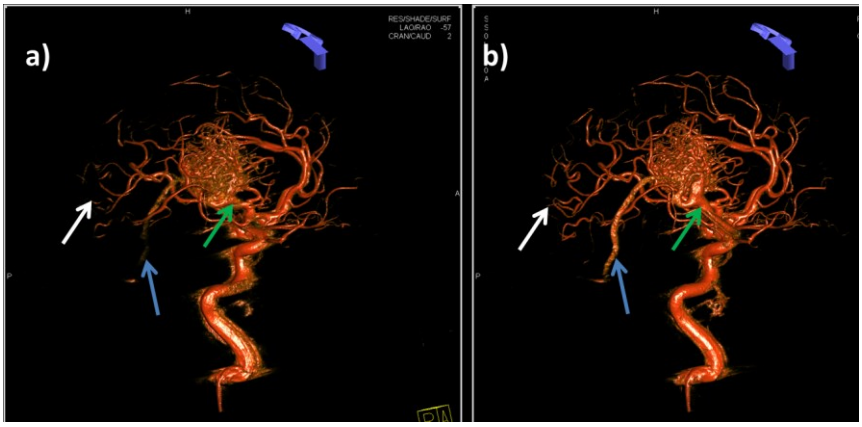

Figure 4-4: Comparison of 3D DSA image quality a) reconstructing only the first 200 degrees of projections b) all 260 degrees of projections. Blue and green arrows show improved visualization of the draining veins. The white arrows show the improved visualization of small distal arteries.

Figure 4-4 provides an example of the benefits of the 260 degree acquisition. This figure shows two reconstructions from a 6s DSA acquisition. The first reconstruction uses only the first 200 degrees of projections to reconstruct the 3D DSA data that will serve as the constraint data for the 4D DSA. Note that since the angular sampling rate is identical to the 5s DSA, this is a close approximation of the reconstructed image quality that would be achieved using a standard 5s DSA scan where the injection is started simultaneously with the fill acquisition. The image on the right hand side of the figure shows the 3D DSA that is reconstructed using all projections acquired over the 260 degree scan range. As a result of the extended time coverage and angular sampling of the 260 degree protocol, a significant improvement in image quality can be seen. Specifically, the green and blue arrows highlight draining venous structures of the AVM that are not well visualized on the simulated

5s DSA, but are clearly visualized with the 6s DSA. Similarly, later filling small distal arterial branches (white arrows) are also better visualized with the extended 6s DSA scan. Finally, streak artifacts around the internal carotid artery due to data inconsistency are seen clearly on the 5s DSA image and are decreased as a result of the additional angular sampling in the 6s DSA image. Streak artifacts such as these often result in distracting artifacts after the 4D DSA reconstruction, as these streaks are included in the constraint image and are enhanced in projections where contrast agent measured in the projection overlaps with the streak artifacts after the temporal encoding step.

4.4.3 Clinical Workflow for Experimental 4D DSA Acquisitions Protocols

Once the experimental acquisition protocols are defined, the next step is to develop workflows that use these protocols in a manner that can be reliably repeated from patient to patient for a variety of neurovascular disorders. The 6s and 12s experimental protocols allow for the grouping of cases into two categories: 1) Early filling arterial structures that enhance within a few seconds of the contrast injection and 2) later filling arterial and early filling venous structures that enhance at a later time point. Establishing a clear distinction between the use of the 6s and 12s DSA protocols is essential such that the physician can ensure adequate temporal coverage with the acquisition at the optimized radiation dose level.

4.4.3.1 6s DSA Acquisition Workflow

The workflow for the 6s DSA requires only a slight modification to the standard clinical workflow for 3D DSA imaging. Typically, an x-ray delay of 1 second is applied to the injection protocol, such that the x-ray acquisition waits 1 second to start from the time the contrast injection begins in order to allow the enhancement of early arterial structures. For the 6s protocol, the x-ray delay is removed, allowing the injector and the x-ray system to start synchronously. This allows for the imaging of the earliest contrast flow into the large arteries while still obtaining enough contrast filling of the smaller, distal arteries to generate a high-quality 3D DSA reconstruction that can serve as a constraint model for the 4D DSA algorithm. **Figure 4-5** provides a pictorial overview of the workflow for the 6s 3D/4D experimental protocol.

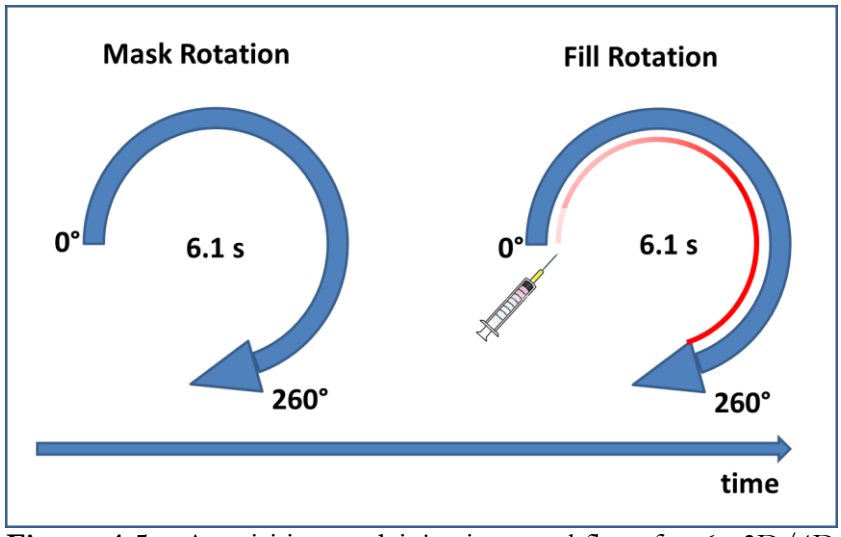

Figure 4-5: Acquisition and injection workflow for 6s 3D/4D DSA acquisition protocol

4.4.3.2 12s DSA Acquisition Workflow

The 12s protocol workflow is very similar to that of the 6s protocol, with one significant difference. With the 6s protocol, the injection lasts for the entire duration of the 6s scan. In a normal patient, the injection rate is typically 2-3 mL/s of contrast agent, resulting in an injection of 12-18mL of total contrast. If we were to keep the same strategy with the 12s acquisition, we would injection 24-36mL of total contrast agent per acquisition, which is a significant amount of contrast for a single acquisition. In order to keep the contrast load reasonable, the 12s workflow uses and injection duration of 8 seconds, which reduced the contrast load and allows for the opportunity to see some washout of contrast at the end of the scan. The final result is a contrast delivery of 16-24 mL total contrast agent. **Figure 4-6** illustrates the acquisition and injection workflow for the 12s 3D/4D DSA protocol.

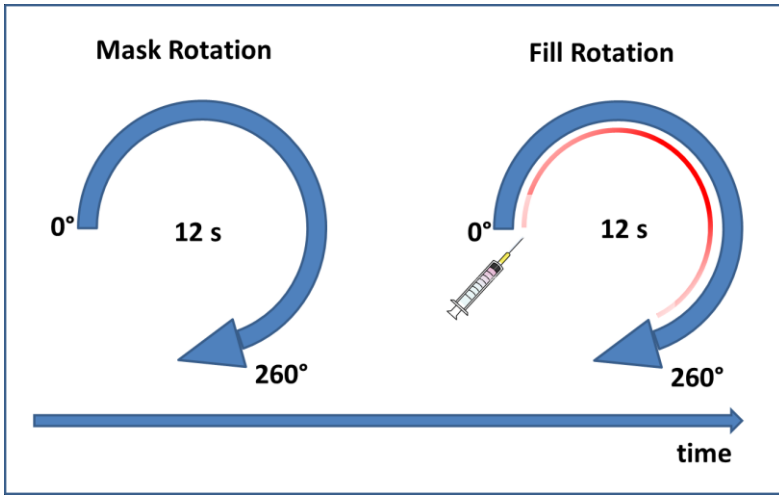

Figure 4-6: Acquisition and injection workflow for 12s 3D/4D DSA acquisition protocol

4.4.4 Experimental Protocol Results

4.4.4.1 6s Protocol Results

More than 20 cases with the 6s protocol have been acquired and evaluated. Early feedback from interventional neuroradiologists and neurosurgeons indicate that his protocol is good for imaging of normal early and mid-phase arterial anatomy and high-grade fistulas and AVMs that shunt to veins within a few seconds of the start of the contrast injection. Any pathology that takes longer than a few seconds to enhance with contrast is often not well visualized by the 6s protocol. Pathologies that should be excluded from the 6s protocol use include (but are not limited to) stroke, stenosis, distal AVMs, small vessel disease and venous pathologies. **Figure 4-7** shows an example of the acquired projections and corresponding 4D DSA reconstruction from the 6s protocol at similar points in time.

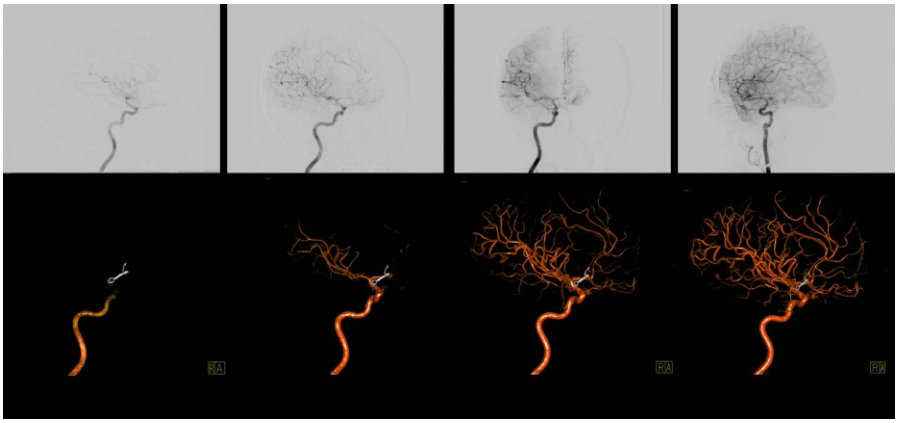

Figure 4-7: Example of 6s DSA projections (top row) and reconstructed 4D DSA time points (bottom row)

4.4.4.2 12s Protocol Results

To date, over 30 cases using the 12s protocol have been collected. There has been limited experience with the 12s protocol for evaluation of occlusive disease such as stenosis or ischemic stroke. Largely, the pre-clinical work with the 12s protocol has focused on large AVMs that require a longer duration than the 6s protocol affords. **Figure 4-8** shows an example of a large AVM imaged using the 12s protocol. The top row shows selected projection frames, and the bottom row shows the 4D DSA results at similar time points as the projection 2D DSA images. The 4D DSA results for the

arterial segments, the nidus, and the draining veins are well visualized in the 4D DSA result. However, the larger sagittal sinus and jugular veins are still not well visualized.

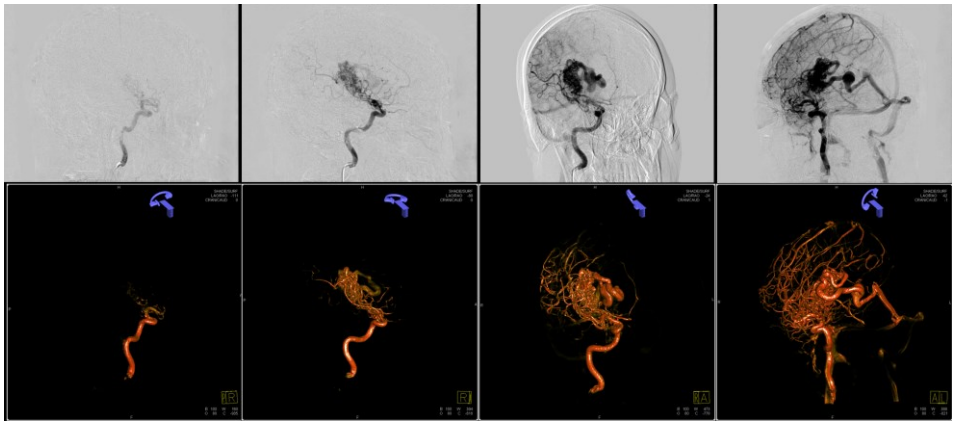

Figure 4-8: Example of 12s DSA projections (top row) and reconstructed 4D DSA time points (bottom row)

Even with this longer scan protocol, venous imaging is difficult due to the typical uneven enhancement of the veins (common with selective contrast injections, this is often due to non-enhanced blood also filling these veins from other territories of the brain) and the timing of their filling. It is not uncommon to have veins in fewer than 40% of the projections with the 12s protocol. As we have seen from previous examples, data inconsistencies introduced by this late filling and uneven contrast enhancement lead to poorly reconstructed venous structures in the 3D DSA reconstruction.

4.5 Open Issues

4.5.1 Current Scan Protocols do not Consistently Result in Adequate Venous Visualization

As pointed out earlier, even with the 12s protocol, it is often difficult to reconstruct the large late-enhancing veins well in the 3D DSA volume. This is due to two factors. First, these venous structures often do not begin to enhance until 6-8 seconds after injection of contrast agent. As a result, fewer than half of the projections have contrast enhancement for these venous structures, and consequently these structures do not reconstruct well in the 4D DSA reconstruction. Second, these structures are draining all regions of the brain, such that they are filled with both non-enhanced blood and contrast enhanced blood. These are low-pressure vascular structures and often result in uneven mixing of the contrast agent with the non-enhanced blood, which also causes significant issues with the quality of the 3D DSA reconstruction for these structures. **Figure 4-9** illustrates an example of this issue.

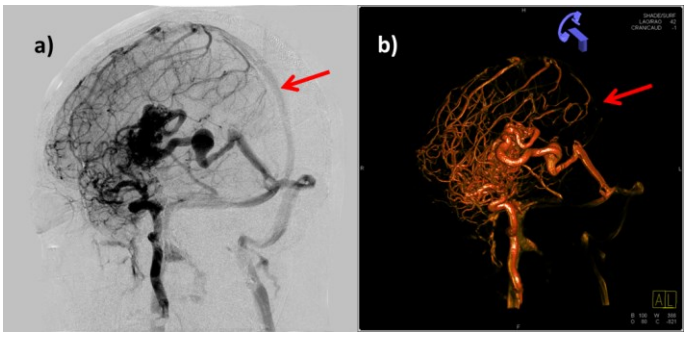

Figure 4-9: a) 2D Projections showing large vein enhancement (red arrow) b) 4D DSA at same time point showing no large vein enhancement (red arrow)

4.5.2 Parenchymal Contrast Blush

Another issue that results from a long bolus and a long, single acquisition is the non-sparse parenchyma that enhances in late capillary phase of the contrast bolus. As discussed in Chapters 2 and 3, the 4D DSA algorithm relies on

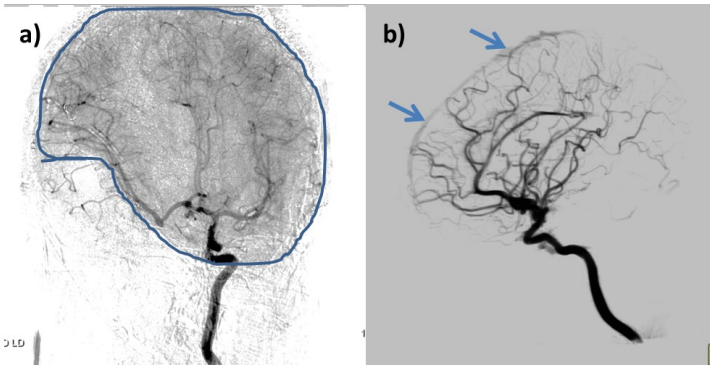

Figure 4-10: a) 2D projection showing the parenchymal contrast "blush" circumscribed in blue b) 4D DSA reconstruction at same time point shows parenchymal blush causing early enhancement of venous structures

sparseness of blood vessels and their distribution in order to minimize the overlap conditions in the 2D projection. The brain parenchyma is a non-sparse object that is often referred to as a "blush" of contrast. In this case, the parenchyma is not reconstructed as part of the 3D DSA volume used to constrain and normalize the 4D DSA reconstruction. As a result, the 4D DSA algorithm has no way to correct for this painting of enhancement that typically occurs across most of the hemisphere supplied by the feeding artery. This results in the parenchyma blush enhancing venous structures early, enhancing arterial structures that have already washed out with contrast, or significantly modulating the scale of the enhancement to unrealistically high levels due to the inability to normalize for this additional enhancement. **Figure 4-10** provides an example of early venous enhancement caused by the parenchymal enhancement in the 2D projection images.

4.5.3 Bolus Duration is Longer than Desired

Most clinical 2D DSA injection protocols use a short, discrete bolus with a duration of only 2 to 3 seconds. Applying a short bolus in this manner has the advantage of using less contrast, but also more importantly, allows for the visualization of the discrete arterial, capillary, and venous phases of the blood flow with minimal overlap. With 4D DSA, we are required to use a longer bolus in order to meet the data consistency requirements necessary to yield a high-quality 3D DSA reconstruction. In

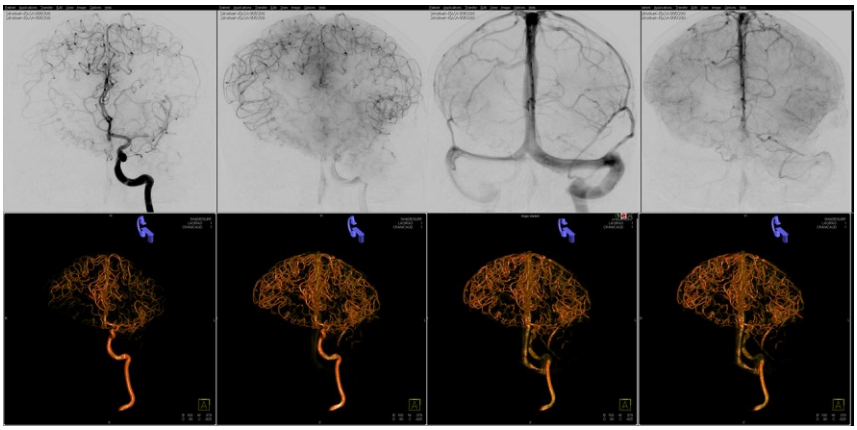

Figure 4-11: top row: 2D DSA study with distinct arterial, capillary, and venous phases **bottom row:** 4D DSA result shows all phases combined together due to the much longer bolus

practice, the 4D DSA protocols require injections that range from 6 to 8 seconds in duration. The results is a 4D DSA reconstruction where most vascular structures stay enhanced through the duration of the 4D DSA reconstruction, resulting in large amounts of overlapping structures (arterial, capillary, and venous) in the later time points of the 4D DSA reconstruction. **Figure 4-11** provides a visual comparison of the 2D DSA (top row) showing discrete phases of arterial, capillary, and venous enhancement. The bottom row of **Figure 4-11** shows the corresponding 4D DSA reconstruction where all phases overlap with each other due to the 3D requirements of having a long contrast bolus.

4.6 Future Work

Future work on injection and acquisition protocols will be aimed at addressing the open issues listed above. The following areas will be investigated.

4.6.1 Multi-Rotation Protocols

One method of addressing many of these issues is to acquire a series of 3D DSA scans using multiple C-arm rotations at shorter durations. This would allow for the use of several constraint 3D DSA volumes (arterial, capillary, and venous for example) and increase the sparsity and reduce the overall complexity of the 3D to 2D overlap. The 4D DSA reconstructions can be performed independently for each rotation, and then concatenated at the end to produce one large

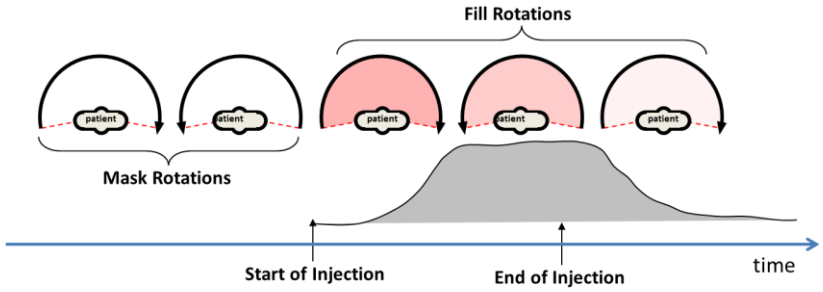

Figure 4-12: Example of one possible design of a multi-rotation acquisition protocol for 4D DSA. This protocol uses 5 total rotations: 2 mask and 3 fill

time-series of volumes. Shortening the rotation time may also allow for a shorter bolus of contrast. This method would help with all three of the open issues discussed above. **Figure 4-12** provides an example of one possible multi-rotation protocol that could be used. Rather than 2 long rotations (as currently implemented), the 4D DSA acquisition could be a series of 5 faster rotations (2 mask and 3 fill), with each of the fill rotations resulting in an independent constraint 3D.

4.6.2 Modeled Bolus Visualization

Due to the long bolus required for the 4D DSA, the later frames of the 4D DSA images typically have large arteries, small arteries, and early filling veins all enhanced at the same time (discussed in **Figure 4-11**). This differs from traditional 2D DSA images, where a short bolus allows early arteries and some small arteries to completely washout prior to the contrast agent reaching the arteries. This results in clear visualization of the different phases (arteries, capillaries, and veins). Currently, 4D DSA cannot provide this due to the long bolus that keeps all of these structures enhanced through most of the acquisitions. One option for creating 4D DSA reconstructions that appear more similar to standard 2D DSA imaging would be to artificially

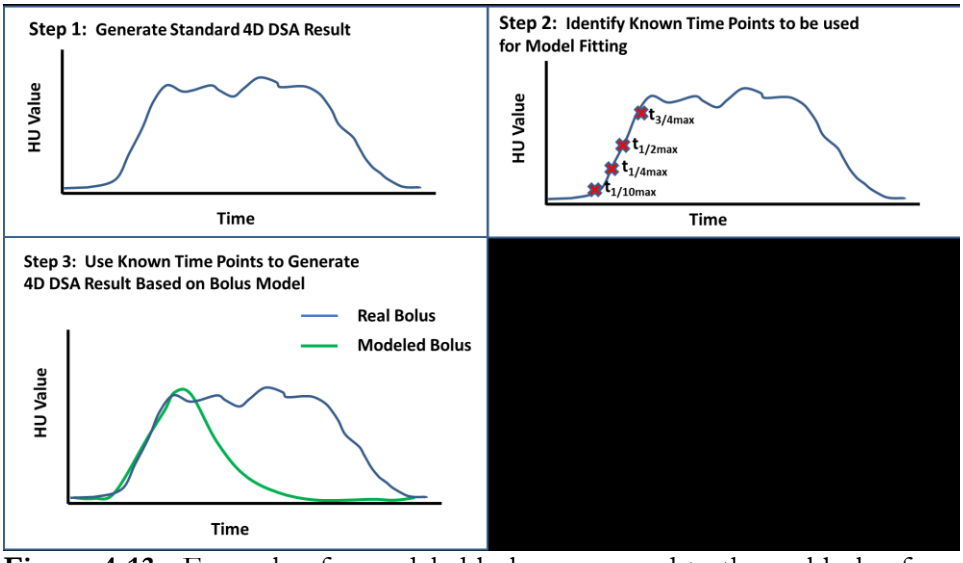

Figure 4-13: Example of a modeled bolus compared to the real bolus for a typical 4D DSA acquisition

(computationally) shorten the bolus in a manner that results in a bolus that is more representative of what is commonly used for 2D DSA. Rather than having a long, broad TCC curve for each voxel, we can use the arrival time and contrast wash-in rate to model a bolus shape that more closely matches that of a 2D DSA injection.

Figure 4-13 provides an example illustration of a how the modeled bolus would be derived from the real measured bolus for 4D DSA. The first step is to generate the standard 4D DSA results. After that, measured data points are extracted from the contrast up-take curve. Finally, those measured data points are used to create a model fit (such as a gamma variate curve) to more closely approximate a standard bolus used in 2D DSA imaging. The disadvantage to this approach is the assumption that is made on how the bolus washes out after the end of the injection. In some cases, such as large aneurysms and capillary or small artery occlusion, the washout rate will be delayed significantly, and this won't be captured by the modeled bolus.

Chapter 5: Pre-clinical and Clinical Results and Applications

5.1 4D DSA Prototype Design and Implementation

In order to gain insight and provide a means of clinically evaluating the 4D DSA reconstructions, a prototype was developed (in conjunction with Siemens) and integrated into the existing angiography equipment platform. The prototype was designed and developed to support both pre-clinical and clinical evaluations of the 4D DSA results. At a high level, the prototype must offer the flexibility to change or adjust parameters associated with the 4D DSA reconstruction algorithm. The prototype must be straightforward to use, and have the computational performance required to generate 4D DSA results in a reasonable amount of time. For this work, we defined a goal of less than five minutes for a 5s DSA scan of 133 mask/fill projection pairs including deformable registration of the mask projection to the fill projection.

The 4D DSA prototype implementation is based on the commercial Siemens *syngo* X-Workplace hardware and software platform (version VB21 and VC10) in order to provide a familiar user interface for the physician or technician. The workstation provides both a 3D/4D viewer as well as a viewer for 2D DSA images. This allows all image analysis tasks to be performed on a single machine. The system hardware contains one high-end graphics card (Nvidia® Quadro® FX 5800, Nvidia Corp, Santa Clara, CA) with a multi-core GPU that is used for the computation associated with the 3D and 4D DSA reconstruction and visualization. The workstation hardware (Fujitsu CELSIUS

R670) runs the Microsoft Windows XP 64bit operating system (Microsoft Corp., Redmond, WA) and has 12GB of installed RAM memory.

5.1.1 4D DSA Prototype Workflow

The 4D DSA prototype workflow can be divided into two basic steps. The first workflow step involves the reconstruction of the 4D DSA result from the mask and fill projection pairs acquired as part of a 3D DSA acquisition. The second workflow step involves the visualization of the 4D DSA results using a rendering engine that allows for both volume rendering technique (VRT) and maximum intensity projection (MIP) viewing of the resulting time-resolved volumes. Additionally, the visualization engine serves as the user interface to allow for the manipulation of the volume viewing projection (rotation and translation), windowing, zooming, and playback of the time-resolved volumes. The 4D DSA results are also archived such that they can be retrieved and reviewed at a later time. **Figure 5-1** provides a graphical depiction of this high-level workflow.

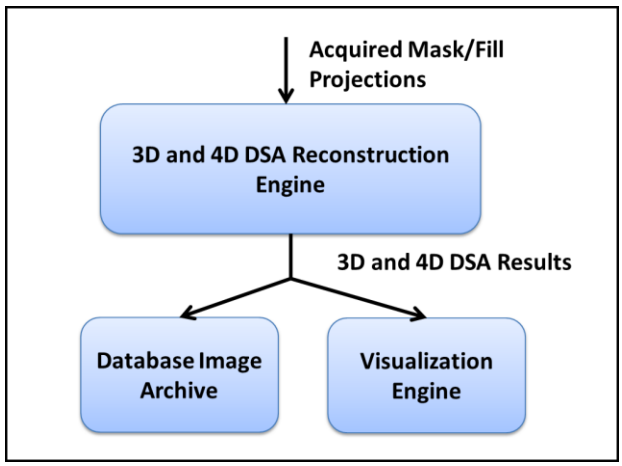

Figure 5-1: High-level overview of 4D DSA prototype workflow

5.1.2 3D and 4D DSA Reconstruction Engine

Once the raw mask and fill projection data are acquired, the projection data is then pre-pre-processed, log-corrected, filtered, subtracted, and backprojected by using a FDK-based cone beam reconstruction algorithm, which has been outlined in previous work[17], [22], [50]. A configuration

option allows for the possibility of performing a block-matching registration algorithm to deform each mask projection to account for patient motion, based on the work by Deuerling-Zheng et al[51]. After the 3D DSA volume is reconstructed, it is stored to the database archive and can be retrieved at a later time.

In order to derive the 4D DSA result, the 3D DSA volumetric data must be segmented to create a sparse vascular volume, where only voxels that have the potential to change intensity values in time (due to contrast propagation) are non-zero. The prototype currently implements a simple intensity threshold segmentation algorithm such that all voxels with values above a certain HU threshold retain their original values. All other voxels are then set to a value of zero. The threshold value can be pre-configured and applied to all cases, or there is an option for a user interaction step where the user defines the threshold value interactively for each case. Once the constraint volume is defined, the 4D DSA methods outlined in Chapter 1 are employed to compute the time resolved 3D DSA data. **Figure 5-2** shows a high-level block diagram of the 4D DSA reconstruction engine that is implemented in the 4D DSA prototype. There are a number of configurable parameters associated with the blurring filter applied to the projections, the angular range used for the angular minimum search, and an optional temporal filter that can be used to denoise the voxel-wise time contrast curves (TCC)s. Once the 4D DSA

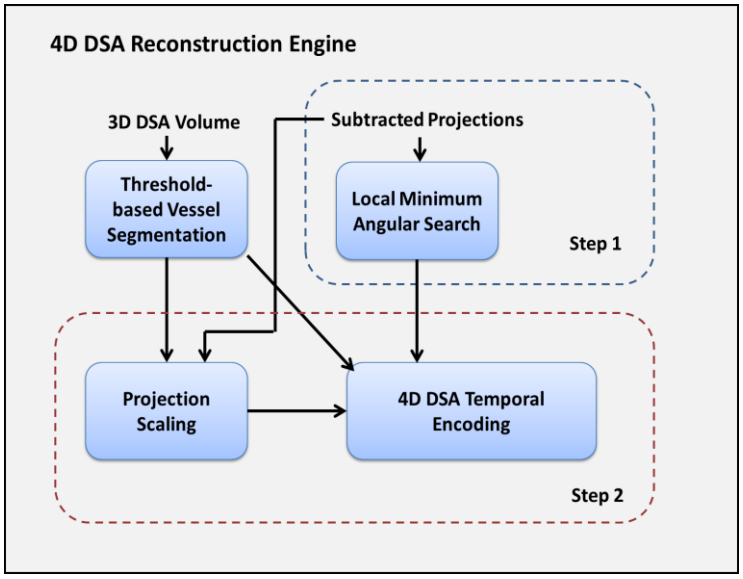

Figure 5-2: Block diagram of the prototype 4D DSA algorithm implementation

reconstruction is completed, the time-varying voxel data is stored to a specific folder on the workstation in a sparse format such that only the segmented (non-zero) voxel values and their indices are stored. This allows for significant data compression and an increase in performance when loading the 4D DSA data from disk into GPU memory for rendering.

5.1.3 4D DSA Prototype User Interface

The 4D DSA prototype was designed to provide a means of quickly loading the projection data from the angiography system via a DICOM transfer over a network or via a file system. The prototype was also designed to perform automated reconstructions in a simple manner to enable its use by clinicians or technologists involved with research studies. Once the automated 4D DSA reconstruction process is complete, two new datasets are written to the DICOM database: 1) standard 3D DSA reconstruction, and 2) the 4D DSA reconstruction results. **Figure 5-3** shows a snapshot of the database from a research case that was retrospectively reconstructed and analyzed. The arrows point to the three different entries associated with the 4D DSA data (the reconstructed 3D DSA, the reconstructed 4D DSA, and the original acquired projection data).

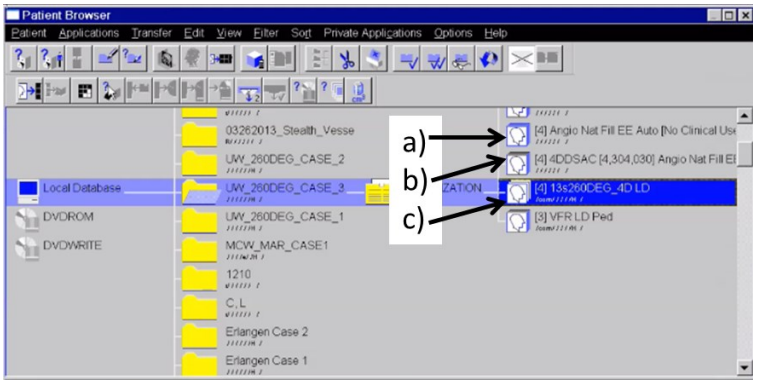

Figure 5-3: DICOM database showing entries of a) 3D DSA volume, b) 4D DSA time-resolved volume, and c) acquired projection data

After the 4D DSA reconstruction is completed, the results are loaded into the 3D/4D viewer tab, known as ***syngo*** InSpace 4D (Siemens AG, Forchheim, Germany). The prototype software is incorporated as a plugin to the InSpace viewer that allows for interaction and manipulation of the volume data after it is loaded into the viewer memory. In order to support the necessary performance requirements for visualizing the volumetric updates in time required by the 4D DSA, a sparse storage and update of voxels was implemented. For example, a standard volumetric matrix for a 3D DSA reconstruction is on the order of 512x512x400 voxels at 16 bit storage depth. This results in a memory requirement of 200Mbytes per volume. The 12s DSA acquisitions have 304 projections, thus resulting in the potential to have 304 time varying instances of the 3D DSA volume. This would require 64Gbytes of memory allocation on the graphics card in order to maintain a reasonable update rate. In order to address this performance issue, the prototype software modifies the rendering software to only store and update the time-varying sparse voxels identified by the constraint volume. As a result, most volumes require less than 1Gbyte of memory to store all 304 time resolved instances, and only ~1% of the total volumetric voxels are updated with each time step.

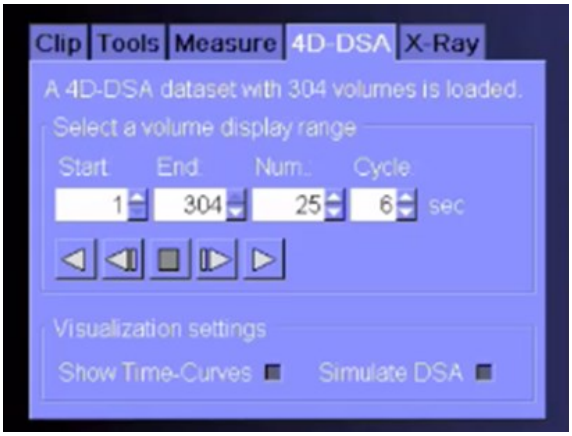

Figure 5-4: Custom 4D DSA control interface

Once the 4D DSA volume is loaded to the InSpace viewer, a custom control (shown in **Figure 5-4**) is activated that can be used to interact with the rendered 4D DSA dataset. The control includes buttons that allow for playing and stepping forward and backwards in time. There is also a stop button that can be used to stop the playback. Additional controls allow for a subset range of projection time points ("Start" and "End") to be used for playback. The user can also select how many subsampled time points are used when playing through the time points ("Num"), as it is not always necessary or desired to play through every available time step in the 4D DSA reconstruction. Finally, the total playback time (from the starting time point to the ending time point) can be specified by the user in order to match realistic playback speed. However, this option is hardware limited, as the current system cannot update the volume at more than 5-7 fps (depending on the selected VRT preset and the complexity of the dataset to be rendered).

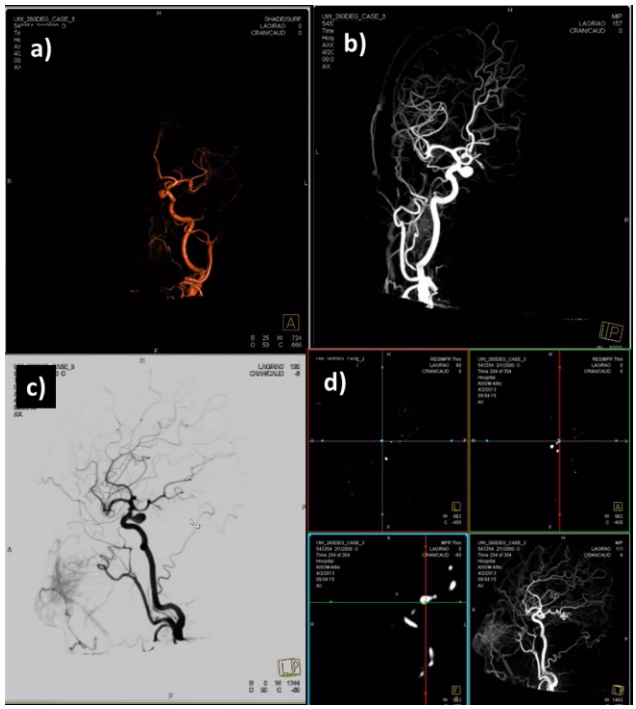

Figure 5-5: Examples of visualization presets: a) VRT Vessel, b) MIP, c) virtual DSA VRT, and d) orthogonal cross-sections (axial, sagittal, coronal)

Once the 4D DSA dataset is loaded into the InSpace VRT engine, the data can be visualized using a VRT preset or MIP display. Currently, modified versions of the workstation product presets are used as a basis to visualize 4D DSA reconstructions. These presets include a "Golden" vessel VRT, a standard "White" vessel VRT, a virtual DSA VRT, and standard MIP visualization. These presets have optimized transfer functions and windowing for general 4D DSA results. In addition to

the full-volume visualization options, the user can also view the 4D DSA time series in cross-sectional planes with a user-defined slice thickness. **Figure 5-5** provides examples of these different rendering modes as applied to a 4D DSA dataset. The user also has access to the same standard InSpace features (including volume cropping, punching, cut planes, rotation, panning, zooming, and bookmarking) for the 4D DSA volume that exist for standard 3D DSA volumes.

The prototype also supports the visualization and export of TCCs from specific voxel locations to assist with quantitative validation efforts and analysis. The custom 4D DSA control has a checkbox option to enable the visualization of a voxel-specific TCC. Once this option is selected, the playback of the 4D DSA will halt and the user must enter the cross-sectional visualization. The crosshairs shown in the cross-sectional slice indicate the voxel that will be interrogated. This data can be exported into a simple text file format that can be analyzed at a later point in time. **Figure 5-6** shows an image of how a specific voxel location can be selected and the TCC can then be displayed in a separate window pane.

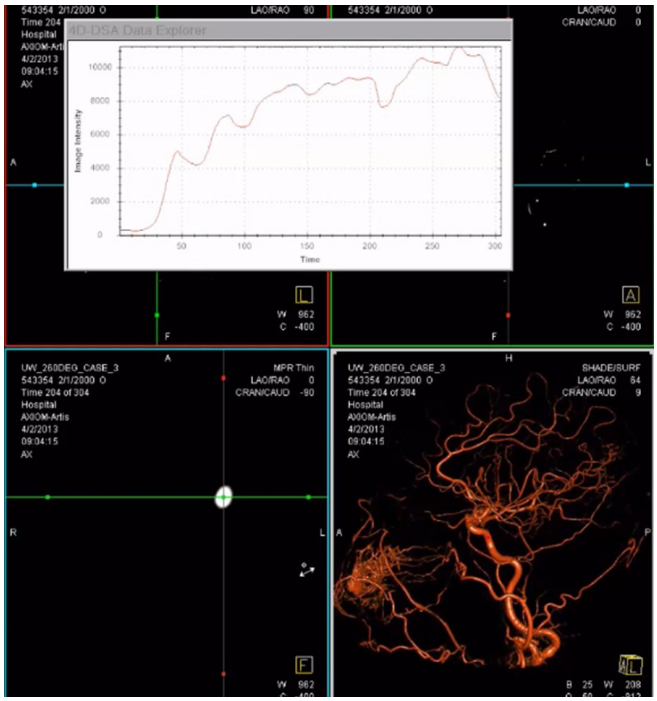

Figure 5-6: White dialog box shows a plot of HU value (y-axis) at a given projection time (x-axis) for the voxel identified by the crosshair location in the lower left pane.

5.2 Pre-clinical Study and Evaluation

In order to further evaluate and validate the 4D DSA method, five canine studies were performed where 2D, 3D, and 4D DSA imaging were acquired for each subject. The beagle canine animal model is one of the most well-established non-primate animal models used for vascular brain imaging research[52]. In addition, the intra-cranial blood vessels of the canine are much smaller(often less than 2mm in diameter) and more densely distributed than those of a human, which poses significant vessel overlap challenges for 2D, 3D, and 4D DSA imaging methods. The goal of this study was to evaluate the image quality and diagnostic performance of the 4D DSA reconstructions compared with conventional 2D and 3D DSA. The evaluation focused on grading each modality's visualization and filling of proximal and distal arterial segments of the head and neck. In this study, radiation dose and x-ray dose was recorded for each subject, however no optimization was performed for the 4D DSA protocols to minimize these dose levels, as the primary goal was to evaluate the accuracy and image quality of the reconstruction.

5.2.1 Methods

5.2.1.1 Image Acquisition

Five canine subjects were evaluated using 2D DSA, 3D DSA, and 4D DSA acquisitions. As specified by the NIH grant application, each canine subject had imaging performed with a 4F guiding catheter located in three different locations: proximal common carotid artery, mid-level external carotid artery, and distal external carotid artery, in order to evaluate the impact of vascular complexity on the 4D DSA results (proximal location considered most complex and distal being considered the least complex). **Figure 5-7** shows example 2D DSA images from the three different catheter positions for one of the subjects. The decreasing level of vascular complexity can be seen as the catheter position changes from the proximal to distal location.

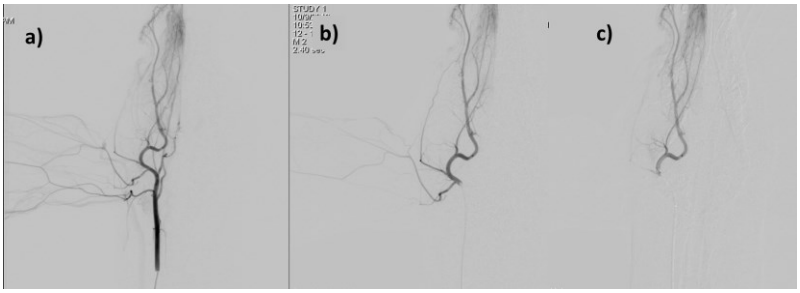

Figure 5-7: 2D DSA images for a) Proximal catheter position b) mid catheter position c) distal catheter position.

At each catheter position, 2D, 3D, and 4D DSA acquisitions were serially performed for each canine research subject. The injection protocol rate, volume, concentration, and timing were aimed at minimizing reflux of contrast, avoiding beam hardening artifacts, and optimum enhancement of the vessels for a given acquisition. A dual syringe power injector (Medtron AG, Germany) was used for all power injections. 2D DSA acquisitions were performed using hand injections of contrast with a syringe in order to mimic the bolus that is typically used in clinical practice. **Table 5-1** summarizes the injection protocols used for the canine research study.

	Proximal			Mid			Distal		
	2D DSA	3D DSA	4D DSA	2D DSA	3D DSA	4D DSA	2D DSA	3D DSA	4D DSA
Contrast Volume (ml)	8-9	20	20	8-9	11	11	8-9	8	9
Concentration (%)	50%	50%	50%	50%	50%	50%	50%	50%	50%
Flow Rate (ml/sec)	H.I.	3	3	H.I.	1.5-2.5	1.5-2.5	H.I.	1-1.5	1-1.5
Injection Duration (sec)	H.I.	6.6	6.6	H.I.	6	6	H.I.	7.3	7.3
Injection Delay (sec)	1	0	0	1	0	0	1	0	0
X-ray Delay (sec)	0	1	0	0	1	0	0	1	0

Table 5-1: 2D, 3D, and 4D DSA injection protocols for canine study. H.I. indicates hand injection was performed.

2D DSA acquisitions were performed for each catheter location during the study. Standard clinical 2D DSA imaging was acquired using a biplane 4 fps acquisition. The zoom factor and collimation for the 2D DSA was set such that all vascular anatomy of interest was always included in the field of view (FOV). Clinically standard anterior-posterior (AP) and lateral (LAT) projection orientations were used for each of the two planes. Similarly, a clinically standard 3D DSA protocol was used to acquire a vascular 3D dataset. One clear difference between the 3D DSA and 4D DSA protocols is the x-ray delay (as seen in **Table 5-1).** Typical 3D DSA clinical protocols use an x-ray delay of 1-2 seconds in order to allow the contrast to reach a more steady state of enhancement in the large arterial segments prior to the start of the 3D acquisitions. The 4D DSA removes this x-ray delay in order to capture contrast dynamics into the projections.

The 4D DSA dataset was acquired using the 6s 260 degree acquisition program. The cerebral circulation time in the canine is much faster than that of a typical human patient. Therefore, it was determined that the 6s DSA acquisition would be the most appropriate acquisition for the canine model due to its short duration. The injection was synchronized with the start of the acquisition such that the first frame of the 4D DSA acquisition contains little to no contrast. **Table 5-2** provides an overview of the 3D and 4D DSA protocols used for the canine study.

	5s DSA	6s DSA
Angular Scan Range	200°	260°
# of Projections per Rotation	133	172
Scan duration	4.6 seconds	6.2 seconds
Dose per Frame (Automatic Exposure Control)	High-dose – 1.20 μGy/F	High-dose – 1.20 μGy/F

Table 5-2: Summary of 3D and 4D DSA acquisition protocols

5.2.1.2 Image Reconstruction

Parameter	Value
Kernel	"HU"
Kernel Characteristic	"Auto"
Motion Correction	Enabled
Matrix Size	512x512
Voxel Size	0.47 mm
Total Slices	388

Table 5-3: Reconstruction properties used for 3D DSA reconstructions

All 2D, 3D, and 4D DSA projection data were transferred to a research workstation running both the commercial software (*syngo* X-workplace VB21, Siemens AG, Forchheim, Germany) and the 4D DSA prototype software. The 3D DSA reconstructions were performed using the product software and standard reconstruction kernels ("HU auto") with a projection-based motion correction algorithm applied to mitigate any

issues with small amounts of subject motion during the acquisition. A matrix size of 512x512 and 388 slices with a reconstructed isotropic voxel size of 0.46 mm (representing the full FOV) was used for all cases. **Table 5-3** summarizes the reconstruction parameters used for the 3D DSA and 4D DSA reconstructions.

Once the 3D DSA reconstruction was complete, the 4D DSA reconstruction was performed. The same reconstruction parameters used for the 3D DSA reconstruction were also used to reconstruct the constraint 3D dataset used as the basis for the 4D DSA reconstruction. The 4D DSA reconstruction also has a number of options that can be configured that are shown in **Table 5-4**. The term σ refers to the spatial or temporal neighborhood size used for the filtering/smoothing kernels. All 4D DSA reconstructions used the same parameters for every subject that was evaluated. Once all 3D and 4D DSA reconstructions were completed, the reconstructed data were stored on the research workstation until the time of evaluation.

Parameter	Value
Angular Search Range	± 5 projections
Temporal Smoothing	σ = 2 time pts
Spatial Smoothing	σ = 2.5 mm
Total Time Frames	172
Frame rate	30 fps

Table 5-4: 4D DSA reconstruction parameters

5.2.1.3 Image Review

The images from all datasets were analyzed by a resident neurosurgeon and a radiologist to identify relevant arterial vascular segments for each catheter position (proximal, mid, and distal) that

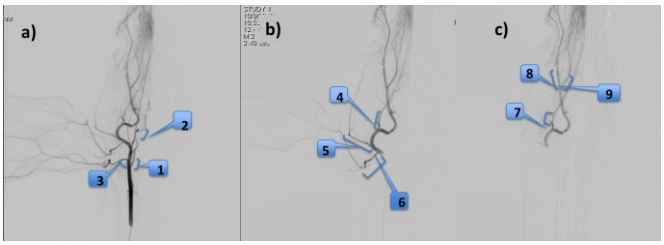

Figure 5-8: Example pictorial reference form provided to the image reviewers identifying the vascular segments to be evaluated. a) proximal b) mid c) distal positions

will be evaluated by the reviewers using each modality. After all segments for review were identified, scoring forms and image keys were generated to provide the reviewers a pictorial reference to clarify the vascular anatomy to be reviewed. **Figure 5-8** shows an example of the pictorial reference that was provided to the image reviewers. **Table 5-5** provides a list of the arterial segments used for evaluation by the image reviewers.

Two experienced neuroradiologists were asked to score the 2D, 3D, and 4D DSA images. **Appendix 1** provides an example review form from a single canine evaluation. **Figure 5-9** provides an example of 2D DSA and 4D DSA time frames at similar time points and matching view angles. Each review form asks the reviewer to score the visualization of three unique arterial vascular segments for each catheter position (9 total vascular segments per canine subject). Specifically, the reviewer is asked to score how well the segment is visualized (is the segment present and is it free of overlap) and if the filling is in an anterograde or retrograde manner. The Hinkmann rating scale (1-5) was used for this part of the evaluation, as it is a scale that has been previously used for similar image evaluation tasks in previously published literature[53]. The reviewer is also asked to score the image quality of the 4D DSA (with respect to a given vascular segment) for two different rendering schemes (VRT and MIP). A scale from 0-4 was used for this portion of the review, as there is historical precedence for this scale from previously published studies with similar image review tasks[54].

Canine Head and Neck Arteries
ICA origin
ICA loop at skull base
Origin of lateral auricular artery
Origin of trifurcation lateral auricular artery
Lingual artery
Infralingual artery
Sublingual artery
Infraorbital artery
Mesial orbital artery
Facial artery
Zygomatic artery

Table 5-5: List of canine artery segments used for image evaluation across all catheter positions

During the image review process, the reviewer is first presented with the 2D DSA image sequences and asked to score these images per the questions provided on the review form for that specific canine subject. Once the 2D DSA scoring is completed, the user is presented with 3D DSA dataset from the corresponding catheter position for the same canine subject. The reviewer is free to rotate, pan and zoom, window, and interact with the 3D DSA volume as they normally would in a standard clinical setting. The reviewer is then asked to score the 3D DSA imaging on the same form for each vessel segment associated with that catheter position.

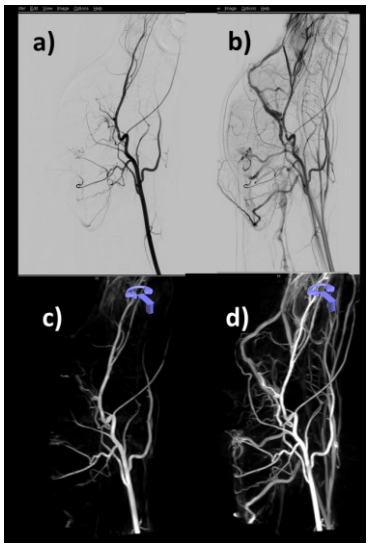

Figure 5-9: Comparison of 2D DSA (a,b) and 4D DSA (c,d) image time frames at a matching orientation and time points.

Finally, the reviewer is presented with the 4D DSA time-series of image volumes. Again the reviewer is allowed to interact with the rendered volume the same way they interacted with the 3D DSA volume (rotate, pan/zoom, etc…). **Figure 5-10** provides a visual comparison of an early 2D DSA time frame, an early 4D DSA time frame from a similar view, and the 3D DSA volume also from the same view orientation. In addition to these methods of interaction, the reviewer is also allowed to play through the time series of volumes, stop playback, and step backward and forward in time as allowed by the user

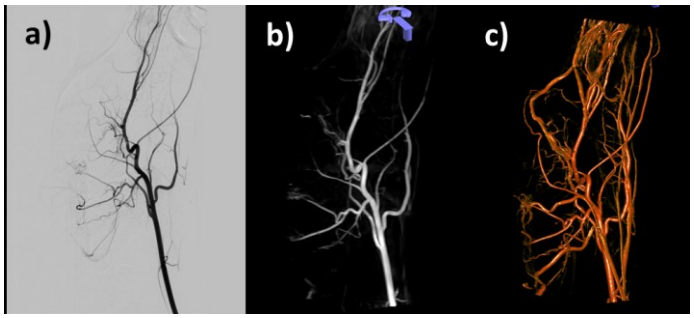

Figure 5-10: Comparison of a) 2D DSA, b) 4D DSA , and c) 3D DSA images

interface of the 4D DSA prototype (described earlier in this chapter). The reviewer is also asked to evaluate the 4D DSA image quality for both volume rendering and MIP visualizations in order to gain an understanding of which rendering strategies are appropriate for certain imaging tasks. The reviewer is also allowed to provide general comments for each review step if there are specific comments and opinions they want to include in the evaluation review. This process is repeated for all three catheter positions for all five canine subjects.

5.2.2 Results

Two independent observers reviewed 44 vessel segments across 5 canine subjects (one subject only had eight vessel segments evaluated). The first evaluation was aimed at assessing the diagnostic image quality for each modality (2D DSA, 3D DSA, and 4D DSA) independently. The reviewers were asked to grade the modality results for each of the 44 vessel segments using the Hinkmann scale (0-4 rating where '0' indicates the vessel cannot be visualized and '4' indicates excellent image quality and arterial enhancement). **Table 5-6** provides an overview of the average modality rating.

	2D DSA	3D DSA	4D DSA
Average Ranking	3.53	3.16	3.79

Table 5-6: Average reviewer rating for 2D, 3D, and 4D DSA modalities. Rankings based on Hinkmann scale (0-4) where '0' indicates vessel is not well visualized and '4' indicates excellent image quality

Reviewers were also asked to judge their preference for rendering the 4D DSA datasets as a volume-rendered display or as a MIP display. In general, reviewers felt that the MIP visualization yielded superior visualization of fine vessel details, where the VRT rendering offered superior depth and overlap information, as well as surface details. Both 4D VRT and 4D MIP rendering yielded an average rating of 1.9 (on a scale of 1-5, where '1' represents excellent image quality and '5' represents insufficient image quality). This indicates that

both VRT and MIP renderings are useful and both should be included as methods for display in the 4D DSA prototype and future studies. Reviewers found the use of two different scales to be confusing. In future work, we will work to use a single grading scale for image evaluation.

Finally, the readers were asked (for each vessel segment) to select the modality that they prefer (between 2D, 3D, and 4D DSA). For 82.4% of cases, reviewers chose 4D DSA as the preferred modality. In 13.5% of cases, 2D DSA was preferred. In just 4.1% of cases, 3D DSA was preferred.

5.2.3 Discussion

Based on the results of reviewer evaluation, 4D DSA appears to provide diagnostic performance at least as good as the existing 2D and 3D DSA imaging modalities. Reviewers appreciated the ability to be able to view the time-resolved volumetric data from any viewing angle and from any point in time. They also appreciated the ability to render the 4D DSA results in a variety of ways (VRT, MIP, etc…) to improve the diagnostic performance of the modality.

This main goal of this study was two-fold. First, the goal was to compare the performance of 4D DSA to the existing gold-standard modalities of 2D and 3D DSA for the task of evaluating morphological details and blood flow patterns in arterial vascular segments. The second goal of the study was to gain experience and gather feedback from expert users on the 4D DSA prototype. Specifically, it is important to understand the necessary playback rates, temporal subsampling requirements, and optimal rendering modes when using the 4D DSA prototype software. This feedback can help to improve the prototype such that it will be more suited for clinical evaluation.

5.2.3.1 Potential Applications

The results show that 4D DSA can be beneficial for evaluation of complex structures where there is potentially a high degree of overlapping vessels. These benefits are derived primarily from the user's ability to use the 4D DSA to evaluate early filling of these complex structures from any desired viewing projection. Based on this observation, we hypothesize that 4D DSA may be very beneficial for evaluation and treat planning for complex AVMs, AV fistulas, and potentially vascular tumors with several arterial feeding arteries that may be considered for embolization treatments. As a result, the first clinical evaluation for 4D DSA will focus on the determining if there is any additional information or added benefits 4D DSA imaging may bring to cerebral AVM diagnosis and treatment planning.

5.3 Clinical Study and Evaluation

Based on the results of the canine study, we proposed an initial clinical study aimed at evaluating the 4D DSA technology applied to the evaluation and treatment planning for cerebral AVMs. Cerebral AVMs are complex vascular diseases that include abnormal arterial-venous connections that can include flow-related pathologies such as intra-nidal aneurysms and arterialized venous systems. All of these pathologies carry an increased risk of cerebral hemorrhage for the patient. Currently, surgeons use a combination of diagnostic modalities such as MR and CT, as well as more invasive selective catheter angiography to gain an understanding of a patient's AVM angioarchitecture and develop a treatment plan. Often, these imaging modalities result in suboptimal assessment of intra-nidal aneurysms, artery to vein fistulas, and venous outflow obstructions due to their inability to resolve vascular overlap. The goal of this small pilot study was determine if the 4D DSA imaging modality can provide additional information for surgeons evaluating brain AVMs.

5.3.1 Methods

Under an institutionally approved protocol 2D, 3D, and 4D DSA image data were acquired in 9 consecutive patients with cerebral AVMs that underwent selective catheter angiography. Each patient received a standard biplane 2D DSA acquisition from standard working projections and used a clinically standard hand injection technique. Each patient also received either a 6s or 12s DSA rotational angiography acquisition that was used for both the 3D and 4D DSA image reconstructions. The same injection protocol was used for all 9 patients and consisted of a 3 ml/s injection rate for total injection duration of 8 seconds resulting in 24 ml of undiluted contrast agent in total. In order to guarantee there was no contrast delivered before the first frame of the acquisition, an injection delay of one second was applied for all cases.

5.3.1.1 Image Reconstruction

All 2D and 3D/4D DSA projection data were transferred to a research workstation running both the commercial software (*syngo* X-workplace VB21, Siemens AG, Forchheim, Germany) and the 4D DSA prototype software. The 3D DSA reconstructions were performed using the product software and standard reconstruction kernels ("HU auto") with a projection-based motion correction algorithm applied to mitigate any issues with small amounts of patient motion during the acquisition. A matrix size of 512x512 and 388 slices with a reconstructed isotropic voxel size of 0.46 mm (representing the full FOV) was used for all cases. The same reconstruction parameters used for the canine study (listed in **Table 5-3**) reconstructions were used for the 3D DSA reconstructions for the AVM clinical study.

Once the 3D DSA reconstruction was complete, the 4D DSA reconstruction was performed. The same reconstruction parameters used for the 3D DSA reconstruction were also used to reconstruct the constraint 3D dataset used as the basis for the 4D DSA reconstruction. The 4D DSA reconstruction parameters were also consistent with what was used for the canine research study (shown in **Table 5-4**). All 4D DSA reconstructions used the same parameters for every subject that was evaluated. After all 3D and 4D DSA reconstructions were completed, the reconstructed data were stored on the research workstation until the time of evaluation.

5.3.1.2 Study Exclusions

After the datasets were reconstructed, an initial review of the datasets was performed by both a resident neurosurgeon and an experienced interventional neuroradiologist. Upon review, it was found that 2 of the cases that used the 6s DSA protocol did not scan long enough to adequately capture the venous drainage of the vascular malformation for the 3D and 4D DSA image modalities. A third dataset included a very small intra-orbital vascular lesion that was not well depicted on any of the three modalities. These three cases were excluded from the review process, resulting in a total of 6 cases used for the final review.

5.3.1.3 Image Review

Review of all 2D, 3D, and 4D DSA images was performed by three expert cerebrovascular neurosurgeons and one interventional radiologist. For each subject, the reviewers were asked to complete the evaluation form shown in **Appendix 2**. Similar to the canine study, each reviewer was presented with images for each modality from a single case and asked to score the imaging modality's ability to visualize intra-nidal aneurysms, arterial-venous fistulas, and venous outflow obstructions.

Also, each modality was evaluated on a 4 point scale[53] for its ability to visualize the blood flow in feeding arterial pedicles, draining veins, and an overall rating of image quality. The reviewers are first presented with the 2D DSA images, followed by the 3D DSA images, and then finally with the 4D DSA images. Once they scored the images for each modality, they are finally asked to state if any one modality is acceptable as a single imaging modality that can provide all of the necessary diagnostic information necessary for the reviewer to evaluate the AVM and plan a strategy for treatment. In total, four reviewers evaluated six cases yielding 24 independent evaluations for 2D, 3D, and 4D DSA.

5.3.2 Results

In three out of the six cases evaluated, there was 100% agreement among the four evaluators that 4D DSA was sufficient to use as a standalone modality and was the preferred modality. In two of the remaining cases, there was agreement among two of four (50%) of the reviewers that 4D DSA was the most useful modality, whereas the other reviewers (50%) indicated that 2D DSA was the preferred modality. In the final case, there was no consensus agreement among the reviewers regarding the preferred modality.

5.3.3 Radiation and Contrast Dose

Radiation and contrast dose was recorded for all 2D DSA and 3D/4D DSA acquisitions for 4 of the 6 cases. Contrast dose was estimated to be 6mL per 2D DSA acquisition, as the injections were performed

	Mean
# of 2D Acqs	11.5
# of 4D Acqs	2
Total 2D DAP	11999 uGym^2
Total 4D DAP	9675 uGym^2
Total 2D Skin Dose	1331 mGy
Total 4D Skin Dose	363 mGy
Total 2D Contrast	71 mL
Total 4D Contrast	47 mL

Table 5-7: Summary of mean radiation and contrast dose for 2D and 4D acquisitions. The mean represents the average per case values across the 4 recorded cases

by hand with a syringe, so precise recording was not possible. The contrast dose used with the 3D/4D DSA acquisitions was performed using a power injector, so precise recording of this contrast load was possible.

Radiation dose recording were taken from the exam dose report that is compiled at the end of each case by the angiographic imaging system. **Table 5-7** provides a summary of the mean radiation and contrast dose for the 4 of 6 recorded cases. The results show overall lower dose area product (DAP) values, significantly lower skin dose levels, and lower contrast dose for the 4D DSA acquisitions compared to the 2D DSA acqusitions.

5.3.4 Discussion

The ability to detect and visualize intra-nidal aneurysms was a distinct advantage for the 4D DSA modality. **Figure 5-11** shows an example case where an intra-nidal aneurysm is clearly seen in an early 4D DSA time frame that is not otherwise depicted in the 2D or 3D DSA modalities. The presence of intra-nidal aneurysms can influence the treatment decisions of the surgeon, as they carry an increased risk of cerebral hemorrhage.

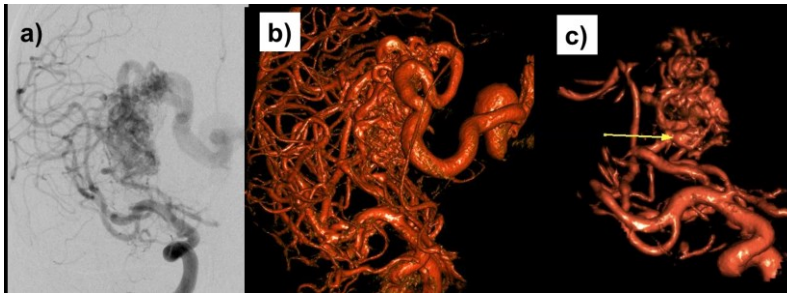

Figure 5-11: a) 2D DSA b) 3D DSA, and c) 4D DSA visualization of AVM. An early time frame of the 4D DSA depicts an intra-nidal aneurysm not shown in the other modalities

Reviewers also indicated that both the MIP and volume-rendering modes each exhibited unique advantages and it is beneficial to incorporate both visualizations when reviewing 4D DSA image data. **Figure 5-12** shows an example of 4D DSA time frames rendered in both MIP visualization and a vessel VRT visualization scheme. Reviewers noted that MIP visualization provided superior small vessel details over the volume rendering and better showed variations in contrast density, such as the difference between arteries and veins (which often have contrast enhanced blood mixed with non-enhanced blood from other vascular territories). Reviewers found that the volume-rendered image data provide better details of the surface and morphology of vascular anatomy, as well as a better understanding of the depth and the spatial relationship of vascular structures. All of these factors are important when decisions regarding the treatment and long-term management of the patient's disease are being made.

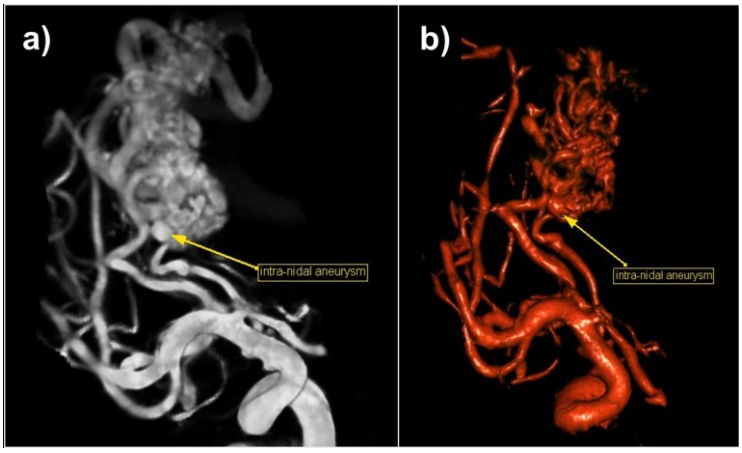

Figure 5-12: a) MIP rendering of 4D DSA time frame b) VRT rendering of 4D DSA time frame. Yellow arrow denotes the intra-nidal aneurysm, which can be observed in both rendering schemes

5.3.5 Conclusion

Although this is a small study with limited scope, the results of the pilot study indicate that 4D DSA could be very useful tool for understanding the angioarchitecture of cerebral AVMs. The ability for the user to play through a time series of 3D images with 4D DSA allows the user to find an optimal combination of viewing projection and vascular filling time points to understand the arterial

pedicles, the draining veins, and uncover potential intra-nidal aneurysm that may have been obscured in existing modalities due to the overlapping vascular structures.

5.4 Future Work

5.4.1 Interventional Neuroradiology Applications

The results from the pre-clinical and clinical studies indicate that 4D DSA can add value for complex, high-flow vascular anatomy such as AVMs and AVFs. Future work will focus on evaluating the 4D DSA technology for ischemic disease such as stenosis, vasospasm, and ischemic stroke where having spatial and temporal information about collateral circulation could be of diagnostic benefit. Other diseases such as aneurysms, arterial dissections, tumors, and moyamoya disease will also be considered.

5.4.2 Non-invasive or Minimally Invasive 4D DSA

Many surgical specialties can benefit from time-resolved 3D angiographic imaging without the need to insert a catheter and perform selective angiography. For example, after a neurosurgeon clips an aneurysm via open surgical access, it is necessary to verify that blood flow has not been compromised to any areas of the brain. Currently, selective angiography is often used to evaluate cerebral vascular blood flow. However, 4D DSA performed using an intravenous injection of contrast or via a pigtail catheter placed in the aortic root could potentially provide quick and easy assurance that blood flow has not been compromised as a result of the surgery.

Several types of AVMs have feeding arteries originating from different supplying large arteries (for example the left and right carotid arteries). These AVMs could potentially be imaged with a single

injection of contrast using these non-invasive or minimally invasive methods. Currently, each vessel segment would need to be imaged separately and evaluated independently.

Future work will focus on characterizing the required signal-to-noise ratio (SNR) that is required by non-selective injections of contrast to yield adequate 4D DSA results.

5.4.3 Quantitative 4D DSA

Once the voxel-wise TCC is derived by the 4D DSA algorithm, these curves can be analyzed to extract specific parametric temporal information such as the time at which the bolus arrived at a given voxel. These derived parameters can then be used to generate composite parametric images of the 3D volume that encode these parameters with a color-coded table. **Figure 5-13** shows an example of bolus arrival time (BAT) visualized as a color-coded display of the 3D volume. Future work will focus on selection of meaningful parameters and visualization schemes to optimally present this quantitative information to the clinician.

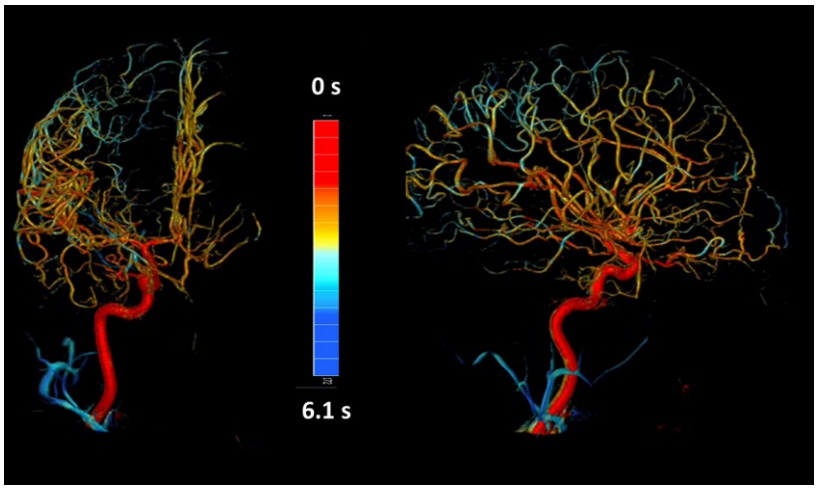

Figure 5-13: Bolus arrival time (BAT) volumetric color-coding (derived from 4D DSA)

Future work will also investigate the potential for deriving velocity and flow rates from the 4D DSA results.

5.4.4 Applications for 4D DSA Outside of Neuroradiology and Neurosurgery

4D DSA has the potential to add diagnostic value for vascular imaging outside of the brain. Interventional radiologists, vascular surgeons, interventional cardiologists, urologists and many other specialties are now performing minimally-invasive vascular procedures for both diagnosis and treatment of a diverse range of vascular disease.

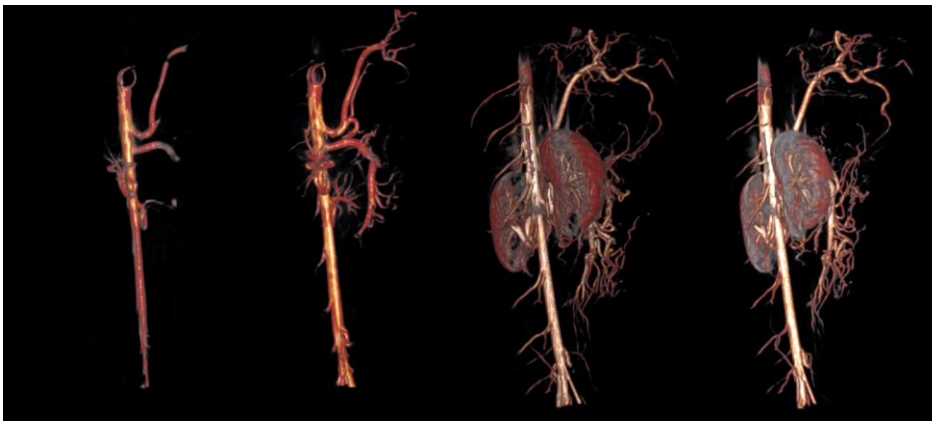

Figure 5-14: 4D DSA time frames of an aortagram performed in canine subject

For example, trans-arterial chemoembolization (TACE) procedures require similar diagnostic imaging requirements as AVMs. Small feeding arteries must be identified, catheterized, and embolized. Having time-resolved 3D imaging of the hepatic arterial system could provide additional information for diagnosis and treatment planning. Similarly, new methods for treating prostate tumors with catheter-based embolization could benefit from the high spatial and temporal resolution provided by 4D DSA. **Figure 5-14** shows an example of a 4D DSA aortagram performed in a canine subject.

In order to enable 4D DSA for chest, abdomen, and peripheral vascular imaging, research will need to focus on motion compensation techniques (due to respiratory and cardiac motion), dose reduction, and scan time reduction. Many patients are not under general anesthesia during these procedures, so non-rigid motion is an issue for these types of procedures that is not present with brain imaging.

Appendix 1: Canine Image Review Form

4D DSA: Validation of Diagnostic and Therapeutic Capabilities

EVALUATION FORM

Examiner:

Subject:

Proximal Carotid artery

SEGMENT 1: ICA origin				
	2D	3D	4D	
1. Is the segment present? Margins and full extent of the segment clearly seen?				Hinkmann scale (0) vessel not delimitable; (1) Poor image quality, blurring of the vessel contours; (2) Fair image quality, suboptimal arterial enhancement for confident diagnosis; (3) Good image quality and arterial enhancement, adequate for confident diagnosis; and (4) Excellent image quality and arterial enhancement.

2. Are there superimposed/adjacent arteries/veins that obscure visualization?				Yes/No
3. Is the segment filling in an antegrade or retrograde manner?				Antegrade/Retrograde
4. 4D DSA rating on 1 to 5 scale MIP				(1) Excellent cannot distinguish a difference in vascular filling from a corresponding 2D acquisition; (2) Good, looks almost like a 2D acquisition; (3) Useable but clearly different than a 2D acquisition; substandard; (4) Marginal for use, vascular filling does not look realistic; (5) Insufficient.
5. 4D DSA rating on 1 to 5 scale Golden				
6. Overall, which image do you prefer?				

SEGMENT 2: ICA loop at skull base			
	2D	3D	4D

1. Is the segment present? Margins and full extent of the segment clearly seen?				Hinkmann scale (0) vessel not delimitable; (1) Poor image quality, blurring of the vessel contours; (2) Fair image quality, suboptimal arterial enhancement for confident diagnosis; (3) Good image quality and arterial enhancement, adequate for confident diagnosis; and (4) Excellent image quality and arterial enhancement.
2. Are there superimposed/adjacent arteries/veins that obscure visualization?				Yes/No
3. Is the segment filling in an antegrade or retrograde manner?				Antegrade/Retrograde
4. 4D DSA rating on 1 to 5 scale MIP				(1) Excellent cannot distinguish a difference in vascular filling from a corresponding 2D acquisition; (2) Good, looks almost like a 2D acquisition; (3) Useable but clearly different than a 2D acquisition; substandard; (4) Marginal for use, vascular filling does not look realistic; (5) Insufficient.
5. 4D DSA rating on 1 to 5 scale Golden				

6. Overall, which image do you prefer?	

SEGMENT 3: Origin of lateral auricular				
	2D	3D	4D	
1. Is the segment present? Margins and full extent of the segment clearly seen?				Hinkmann scale (0) vessel not delimitable; (1) Poor image quality, blurring of the vessel contours; (2) Fair image quality, suboptimal arterial enhancement for confident diagnosis; (3) Good image quality and arterial enhancement, adequate for confident diagnosis; and (4) Excellent image quality and arterial enhancement.
2. Are there superimposed/adjacent arteries/veins that obscure visualization?				Yes/No
3. Is the segment filling in an antegrade or retrograde manner?				Antegrade/Retrograde
4. 4D DSA rating on 1 to 5 scale MIP				(1) Excellent cannot distinguish a difference in vascular filling from a corresponding 2D acquisition; (2) Good, looks almost like a 2D acquisition; (3) Useable but clearly different than a 2D

				acquisition; substandard; (4) Marginal for use, vascular filling does not look realistic; (5) Insufficient.
5. 4D DSA rating on 1 to 5 scale Golden				
6. Overall, which image do you prefer?				

Most distal Carotid Artery			
SEGMENT 4: Lingual artery			
	2D	3D	4D

1. Is the segment present? Margins and full extent of the segment clearly seen?				Hinkmann scale (0) vessel not delimitable; (1) Poor image quality, blurring of the vessel contours; (2) Fair image quality, suboptimal arterial enhancement for confident diagnosis; (3) Good image quality and arterial enhancement, adequate for confident diagnosis; and (4) Excellent image quality and arterial enhancement.
2. Are there superimposed/adjacent arteries/veins that obscure visualization?				Yes/No
3. Is the segment filling in an antegrade or retrograde manner?				Antegrade/Retrograde
4. 4D DSA rating on 1 to 5 scale MIP				(1) Excellent cannot distinguish a difference in vascular filling from a corresponding 2D acquisition; (2) Good, looks almost like a 2D acquisition; (3) Useable but clearly different than a 2D acquisition; substandard; (4) Marginal for use, vascular filling does not look realistic; (5) Insufficient.
5. 4D DSA rating on 1 to 5 scale Golden				

6. Overall, which image do you prefer?	

SEGMENT 5: Infraorbital artery				
	2D	3D	4D	
1. Is the segment present? Margins and full extent of the segment clearly seen?				Hinkmann scale (0) vessel not delimitable; (1) Poor image quality, blurring of the vessel contours; (2) Fair image quality, suboptimal arterial enhancement for confident diagnosis; (3) Good image quality and arterial enhancement, adequate for confident diagnosis; and (4) Excellent image quality and arterial enhancement.
2. Are there superimposed/adjacent arteries/veins that obscure visualization?				Yes/No
3. Is the segment filling in an antegrade or retrograde manner?				Antegrade/Retrograde
4. 4D DSA rating on 1 to 5 scale MIP				(1) Excellent cannot distinguish a difference in vascular filling from a corresponding 2D acquisition; (2) Good, looks almost like a 2D acquisition; (3) Useable but clearly different than a 2D

				acquisition; substandard; (4) Marginal for use, vascular filling does not look realistic; (5) Insufficient.
5. 4D DSA rating on 1 to 5 scale Golden				
6. Overall, which image do you prefer?				

SEGMENT 6: Facial artery				
	2D	3D	4D	
1. Is the segment present? Margins and full extent of the segment clearly seen?				Hinkmann scale (0) vessel not delimitable; (1) Poor image quality, blurring of the vessel contours; (2) Fair image quality, suboptimal arterial enhancement for confident diagnosis; (3) Good image quality and arterial enhancement, adequate for confident diagnosis; and (4) Excellent image quality and

				arterial enhancement.
2. Are there superimposed/adjacent arteries/veins that obscure visualization?				Yes/No
3. Is the segment filling in an antegrade or retrograde manner?				Antegrade/Retrograde
4. 4D DSA rating on 1 to 5 scale MIP				(1) Excellent cannot distinguish a difference in vascular filling from a corresponding 2D acquisition; (2) Good, looks almost like a 2D acquisition; (3) Useable but clearly different than a 2D acquisition; substandard; (4) Marginal for use, vascular filling does not look realistic; (5) Insufficient.
5. 4D DSA rating on 1 to 5 scale Golden				
6. Overall, which image do you prefer?				

Mid portion of carotid artery				
SEGMENT 7: Sublingual artery				
	2D	3D	4D	
1. Is the segment present? Margins and full extent of the segment clearly seen?				Hinkmann scale (0) vessel not delimitable; (1) Poor image quality, blurring of the vessel contours; (2) Fair image quality, suboptimal arterial enhancement for confident diagnosis; (3) Good image quality and arterial enhancement, adequate for confident diagnosis; and (4) Excellent image quality and arterial enhancement.
2. Are there superimposed/adjacent arteries/veins that obscure visualization?				Yes/No
3. Is the segment filling in an antegrade or retrograde manner?				Antegrade/Retrograde

4. 4D DSA rating on 1 to 5 scale MIP				(1) Excellent cannot distinguish a difference in vascular filling from a corresponding 2D acquisition; (2) Good, looks almost like a 2D acquisition; (3) Useable but clearly different than a 2D acquisition; substandard; (4) Marginal for use, vascular filling does not look realistic; (5) Insufficient.
5. 4D DSA rating on 1 to 5 scale Golden				
6. Overall, which image do you prefer?				

SEGMENT 8: Zygomatic artery				
	2D	3D	4D	
1. Is the segment present? Margins and full extent of the segment clearly seen?				Hinkmann scale (0) vessel not delimitable; (1) Poor image quality, blurring of the vessel contours; (2) Fair image quality, suboptimal arterial enhancement for confident diagnosis; (3) Good image quality and arterial enhancement, adequate for confident diagnosis; and (4)

				Excellent image quality and arterial enhancement.
2. Are there superimposed/adjacent arteries/veins that obscure visualization?				Yes/No
3. Is the segment filling in an antegrade or retrograde manner?				Antegrade/Retrograde
4. 4D DSA rating on 1 to 5 scale MIP				(1) Excellent cannot distinguish a difference in vascular filling from a corresponding 2D acquisition; (2) Good, looks almost like a 2D acquisition; (3) Useable but clearly different than a 2D acquisition; substandard; (4) Marginal for use, vascular filling does not look realistic; (5) Insufficient.
5. 4D DSA rating on 1 to 5 scale Golden				
6. Overall, which image do you prefer?				

SEGMENT 9: Origin of trifurcation of auriculars (lat/intermediate/medial)				
	2D	3D	4D	
1. Is the segment present? Margins and full extent of the segment clearly seen?				Hinkmann scale (0) vessel not delimitable; (1) Poor image quality, blurring of the vessel contours; (2) Fair image quality, suboptimal arterial enhancement for confident diagnosis; (3) Good image quality and arterial enhancement, adequate for confident diagnosis; and (4) Excellent image quality and arterial enhancement.
2. Are there superimposed/adjacent arteries/veins that obscure visualization?				Yes/No
3. Is the segment filling in an antegrade or retrograde manner?				Antegrade/Retrograde
4. 4D DSA rating on 1 to 5 scale MIP				(1) Excellent cannot distinguish a difference in vascular filling from a corresponding 2D acquisition; (2) Good, looks almost like a 2D acquisition; (3) Useable but clearly different than a 2D acquisition; substandard; (4) Marginal for use, vascular filling does not look realistic; (5) Insufficient.

5. 4D DSA rating on 1 to 5 scale Golden	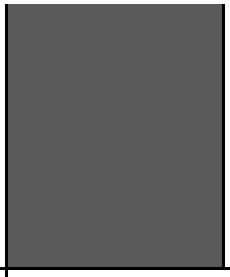
6. Overall, which image do you prefer?	

Question 15: Overall, which image do you prefer?		2D + 3D or 4D.

Appendix 2: Reviewer Evaluation Form for Clinical AVM Imaging

CASE #			
	2D	**3D**	**4D**
Evaluate nidal architecture			
1. Is there an intra-nidal aneurysm?	Yes / No	Yes / No	Yes / No
2. Is there a fistula?	Yes / No	Yes / No	Yes / No
3. Is there venous obstruction?	Yes / No	Yes / No	Yes / No
4. Overall rating scale	0 1 2 3	0 1 2 3	0 1 2 3
Sequence of arterial filling			
5. Feeding pedicles	0 1 2 3	0 1 2 3	0 1 2 3
Sequence of venous drainage			
6. Venous drainage	0 1 2 3	0 1 2 3	0 1 2 3
Overall Impression			
7. Are any of the 3 sufficient as a standalone test? If so which?			
Yes / No			

References

[1] J. Rösch, F. S. Keller, and J. A. Kaufman, "The Birth, Early Years, and Future of Interventional Radiology," *J. Vasc. Interv. Radiol.*, vol. 14, no. 7, pp. 841–853, Jul. 2003.

[2] J. S. Krohmer, "Radiography and fluoroscopy, 1920 to the present.," *Radiographics*, vol. 9, no. 6, pp. 1129–1153, Nov. 1989.

[3] D. P. Friedman and B. K. Pramanik, "Fellowship and Practice Trends in Neuroradiology Training Programs in the United States," *Am. J. Neuroradiol.*, vol. 22, no. 9, pp. 1650–1653, Oct. 2001.

[4] J. J. Connors III, D. Sacks, A. J. Furlan, W. R. Selman, E. J. Russell, P. E. Stieg, and M. N. Hadley, "Training, Competency, and Credentialing Standards for Diagnostic Cervicocerebral Angiography, Carotid Stenting, and Cerebrovascular Intervention," *J. Vasc. Interv. Radiol.*, vol. 15, no. 12, pp. 1347–1356, Dec. 2004.

[5] T. M. Grist, C. A. Mistretta, C. M. Strother, and P. A. Turski, "Time-resolved angiography: Past, present, and future," *J. Magn. Reson. Imaging*, vol. 36, no. 6, pp. 1273–1286, 2012.

[6] C. A. Mistretta, "Sub-Nyquist acquisition and constrained reconstruction in time resolved angiography," *Med. Phys.*, vol. 38, no. 6, pp. 2975–2985, 2011.

[7] C. A. Mistretta, "Undersampled radial MR acquisition and highly constrained back projection (HYPR) reconstruction: Potential medical imaging applications in the post-Nyquist era," *J. Magn. Reson. Imaging*, vol. 29, no. 3, pp. 501–516, 2009.

[8] B. T. Christian, N. T. Vandehey, J. M. Floberg, and C. A. Mistretta, "Dynamic PET Denoising with HYPR Processing," *J. Nucl. Med.*, vol. 51, no. 7, pp. 1147–1154, Jul. 2010.

[9] J. M. Floberg, C. A. Mistretta, J. P. Weichert, L. T. Hall, J. E. Holden, and B. T. Christian, "Improved kinetic analysis of dynamic PET data with optimized HYPR-LR," *Med. Phys.*, vol. 39, no. 6, pp. 3319–3331, 2012.

[10] R. Krissak, C. A. Mistretta, T. Henzler, A. Chatzikonstantinou, J. Scharf, S. O. Schoenberg, and C. Fink, "Noise Reduction and Image Quality Improvement of Low Dose and Ultra Low Dose Brain Perfusion CT by HYPR-LR Processing," *PLoS ONE*, vol. 6, no. 2, p. e17098, Feb. 2011.

[11] K. Royalty, M. Manhart, K. Pulfer, Y. Deuerling-Zheng, C. Strother, A. Fieselmann, and D. Consigny, "C-Arm CT Measurement of Cerebral Blood Volume and Cerebral Blood Flow Using a Novel High-Speed Acquisition and a Single Intravenous Contrast Injection," *Am. J. Neuroradiol.*, May 2013.

[12] B. Davis, K. Royalty, M. Kowarschik, C. Rohkohl, E. Oberstar, B. Aagaard-Kienitz, D. Niemann, O. Ozkan, C. Strother, and C. Mistretta, "4D Digital Subtraction Angiography: Implementation and Demonstration of Feasibility," *Am. J. Neuroradiol.*, Apr. 2013.

[13] C. A. Mistretta, E. Oberstar, B. Davis, E. Brodsky, and C. M. Strother, "4D-DSA and 4D fluoroscopy: preliminary implementation," pp. 762227–762227, Mar. 2010.

[14] R. A. Pooley, J. M. McKinney, and D. A. Miller, "The AAPM/RSNA Physics Tutorial for Residents Digital Fluoroscopy1," *Radiographics*, vol. 21, no. 2, pp. 521–534, Mar. 2001.

[15] A. B. Crummy, M. F. Stieghorst, P. A. Turski, C. M. Strother, R. P. Lieberman, J. F. Sackett, W. D. Turnipseed, D. E. Detmer, and C. A. Mistretta, "Digital subtraction angiography: current status and use of intra-arterial injection.," *Radiology*, vol. 145, no. 2, pp. 303–307, Nov. 1982.

[16] R. Fahrig, A. J. Fox, S. Lownie, and D. W. Holdsworth, "Use of a C-arm system to generate true three-dimensional computed rotational angiograms: preliminary in vitro and in vivo results.," *Am. J. Neuroradiol.*, vol. 18, no. 8, pp. 1507–1514, Sep. 1997.

[17] R. Fahrig, M. Moreau, and D. W. Holdsworth, "Three-dimensional computed tomographic reconstruction using a C-arm mounted XRII: correction of image intensifier distortion," *Med. Phys.*, vol. 24, no. 7, pp. 1097–1106, Jul. 1997.

[18] T. Abe, M. Hirohata, N. Tanaka, Y. Uchiyama, K. Kojima, K. Fujimoto, A. M. Norbash, and N. Hayabuchi, "Clinical Benefits of Rotational 3D Angiography in Endovascular Treatment of Ruptured Cerebral Aneurysm," *Am. J. Neuroradiol.*, vol. 23, no. 4, pp. 686–688, Apr. 2002.

[19] W. J. van Rooij, M. E. Sprengers, A. N. de Gast, J. P. P. Peluso, and M. Sluzewski, "3D Rotational Angiography: The New Gold Standard in the Detection of Additional Intracranial Aneurysms," *Am. J. Neuroradiol.*, vol. 29, no. 5, pp. 976–979, May 2008.

[20] A. Hochmuth, U. Spetzger, and M. Schumacher, "Comparison of Three-Dimensional Rotational Angiography with Digital Subtraction Angiography in the Assessment of Ruptured Cerebral Aneurysms," *Am. J. Neuroradiol.*, vol. 23, no. 7, pp. 1199–1205, Aug. 2002.

[21] J. A. Seibert, "Flat-panel detectors: how much better are they?," *Pediatr. Radiol.*, vol. 36, no. 2, pp. 173–181, Sep. 2006.

[22] M. Zellerhoff, B. Scholz, E.-P. Ruehrnschopf, and T. Brunner, "Low contrast 3D reconstruction from C-arm data," pp. 646–655, Apr. 2005.

[23] W. A. Kalender, "Der Einsatz von Flachbilddetektoren für die CT-Bildgebung," *Radiol.*, vol. 43, no. 5, pp. 379–387, 2003.

[24] G. J. E. Rinkel, M. Djibuti, A. Algra, and J. van Gijn, "Prevalence and Risk of Rupture of Intracranial Aneurysms A Systematic Review," *Stroke*, vol. 29, no. 1, pp. 251–256, Jan. 1998.

[25] S. C. Wong, O. Nawawi, N. Ramli, A. Kadir, and K. Azmi, "Benefits of 3D Rotational DSA Compared with 2D DSA in the Evaluation of Intracranial Aneurysm," *Acad. Radiol.*, vol. 19, no. 6, pp. 701–707, Jun. 2012.

[26] F. Kucukay, R. S. Okten, A. Tekiner, M. Dagli, C. Gocek, M. A. Bayar, and T. Cumhur, "Three-dimensional volume rendering digital subtraction angiography in comparison with two-dimensional digital subtraction angiography and rotational angiography for detecting aneurysms and their morphological properties in patients with subarachnoid hemorrhage," *Eur. J. Radiol.*, vol. 81, no. 10, pp. 2794–2800, Oct. 2012.

[27] P. Gölitz, T. Struffert, F. Knossalla, M. Saake, S. Ott, O. Ganslandt, and A. Doerfler, "Angiographic CT with Intravenous Contrast Injection Compared with Conventional Rotational Angiography in the Diagnostic Work-Up of Cerebral Aneurysms," *Am. J. Neuroradiol.*, vol. 33, no. 5, pp. 982–987, May 2012.

[28] J. S. McDonald, R. J. McDonald, J. Fan, D. F. Kallmes, G. Lanzino, and H. J. Cloft, "Comparative Effectiveness of Unruptured Cerebral Aneurysm Therapies Propensity Score Analysis of Clipping Versus Coiling," *Stroke*, vol. 44, no. 4, pp. 988–994, Apr. 2013.

[29] W. Brinjikji, M. H. Murad, G. Lanzino, H. J. Cloft, and D. F. Kallmes, "Endovascular Treatment of Intracranial Aneurysms With Flow Diverters A Meta-Analysis," *Stroke*, vol. 44, no. 2, pp. 442–447, Feb. 2013.

[30] R. Al-Shahi and C. Warlow, "A systematic review of the frequency and prognosis of arteriovenous malformations of the brain in adults," *Brain*, vol. 124, no. 10, pp. 1900–1926, Oct. 2001.

[31] P. W. A. Willems, P. Taeshineetanakul, B. Schenk, P. A. Brouwer, K. G. Terbrugge, and T. Krings, "The use of 4D-CTA in the diagnostic work-up of brain arteriovenous malformations," *Neuroradiology*, vol. 54, no. 2, pp. 123–131, Feb. 2012.

[32] T. Illies, N. D. Forkert, T. Ries, J. Regelsberger, and J. Fiehler, "Classification of Cerebral Arteriovenous Malformations and Intranidal Flow Patterns by Color-Encoded 4D-Hybrid-MRA," *Am. J. Neuroradiol.*, vol. 34, no. 1, pp. 46–53, Jan. 2013.

[33] A. Back, O. Zeck, C. Shkedy, and P. Shedden, "Staged Embolization with Staged Gamma Knife Radiosurgery to Treat a Large AVM," *Can. J. Neurol. Sci.*, vol. 36, no. 4, pp. 500–503, Jul. 2009.

[34] R. F. Spetzler, N. A. Martin, L. P. Carter, R. A. Flom, P. A. Raudzens, and E. Wilkinson, "Surgical management of large AVM's by staged embolization and operative excision," *J. Neurosurg.*, vol. 67, no. 1, pp. 17–28, Jul. 1987.

[35] W. J. van Rooij, M. Sluzewski, and G. N. Beute, "Brain AVM Embolization with Onyx," *Am. J. Neuroradiol.*, vol. 28, no. 1, pp. 172–177, Jan. 2007.

[36] J. P. Rahal and A. M. Malek, "Benefit of cone-beam computed tomography angiography in acute management of angiographically undetectable ruptured arteriovenous malformations: Clinical article," *J. Neurosurg.*, vol. 119, no. 4, pp. 1015–1020, Oct. 2013.

[37] H. Schmitt, M. Grass, R. Suurmond, T. Köhler, V. Rasche, S. Hähnel, and S. Heiland, "Reconstruction of blood propagation in three-dimensional rotational X-ray angiography (3D-RA)," *Comput. Med. Imaging Graph.*, vol. 29, no. 7, pp. 507–520, Oct. 2005.

[38] I. Waechter, J. Bredno, R. Hermans, J. Weese, D. C. Barratt, and D. J. Hawkes, "Model-based blood flow quantification from rotational angiography," *Med. Image Anal.*, vol. 12, no. 5, pp. 586–602, Oct. 2008.

[39] A. D. Copeland, R. S. Mangoubi, M. N. Desai, S. K. Mitter, and A. M. Malek, "Spatio-Temporal Data Fusion for 3D+T Image Reconstruction in Cerebral Angiography," *IEEE Trans. Med. Imaging*, vol. 29, no. 6, pp. 1238–1251, 2010.

[40] B. A. Schueler, D. F. Kallmes, and H. J. Cloft, "3D Cerebral Angiography: Radiation Dose Comparison with Digital Subtraction Angiography," *Am. J. Neuroradiol.*, vol. 26, no. 8, pp. 1898–1901, Sep. 2005.

[41] J. Endres, M. Kowarschik, T. Redel, P. Sharma, V. Mihalef, J. Hornegger, and A. Doerfler, "A Workflow for Patient-Individualized Virtual Angiogram Generation Based on CFD Simulation," *Comput. Math. Methods Med.*, vol. 2012, Nov. 2012.

[42] E. J. Candes, J. Romberg, and T. Tao, "Robust uncertainty principles: exact signal reconstruction from highly incomplete frequency information," *IEEE Trans. Inf. Theory*, vol. 52, no. 2, pp. 489–509, 2006.

[43] F. M. Khan, "The Physics of Radiation Therapy," *CERN Document Server*, 2003. [Online]. Available: http://cds.cern.ch/record/1101043. [Accessed: 23-Jan-2014].

[44] M. Terabe, H. Ichikawa, T. Kato, and K. Koshida, "Artifacts caused by insufficient contrast medium filling during C-arm cone-beam CT scans: a phantom study," *Radiol. Phys. Technol.*, pp. 1–10.

[45] J. Tang, P. Thériault Lauzier, Z. Qi, T. Szczykutowicz, and G.-H. Chen, "New consistency theorem of motion contaminated projection data and applications in motion artifacts correction," 2012, vol. 8313, p. 83131E–83131E–8.

[46] C. J. Lin, S. C. Hung, W. Y. Guo, F. C. Chang, C. B. Luo, J. Beilner, M. Kowarschik, W. F. Chu, and C. Y. Chang, "Monitoring Peri-Therapeutic Cerebral Circulation Time: A Feasibility Study Using Color-Coded Quantitative DSA in Patients with Steno-Occlusive Arterial Disease," *Am. J. Neuroradiol.*, vol. 33, no. 9, pp. 1685–1690, Oct. 2012.

[47] L. A. Feldkamp, L. C. Davis, and J. W. Kress, "Practical cone-beam algorithm," *J. Opt. Soc. Am. A*, vol. 1, no. 6, pp. 612–619, Jun. 1984.

[48] R. Fahrig, A. J. Fox, S. Lownie, and D. W. Holdsworth, "Use of a C-arm system to generate true three-dimensional computed rotational angiograms: preliminary in vitro and in vivo results.," *Am. J. Neuroradiol.*, vol. 18, no. 8, pp. 1507–1514, Sep. 1997.

[49] R. K. Tu, W. A. Cohen, K. R. Maravilla, W. H. Bush, N. H. Patel, J. Eskridge, and H. R. Winn, "Digital subtraction rotational angiography for aneurysms of the intracranial anterior circulation: injection method and optimization.," *Am. J. Neuroradiol.*, vol. 17, no. 6, pp. 1127–1136, Jun. 1996.

[50] N. Strobel, O. Meissner, J. Boese, T. Brunner, B. Heigl, M. Hoheisel, G. Lauritsch, M. Nagel, M. Pfister, E.-P. Rührnschopf, B. Scholz, B. Schreiber, M. Spahn, M. Zellerhoff, and K. Klingenbeck-Regn, "3D Imaging with Flat-Detector C-Arm Systems," in *Multislice CT*, M. F. Reiser, C. R. Becker, K. Nikolaou, and G. Glazer, Eds. Springer Berlin Heidelberg, 2009, pp. 33–51.

[51] Y. Deuerling-Zheng, M. Lell, A. Galant, and J. Hornegger, "Motion compensation in digital subtraction angiography using graphics hardware," *Comput. Med. Imaging Graph.*, vol. 30, no. 5, pp. 279–289, Jul. 2006.

[52] M. Mehra, N. Henninger, J. A. Hirsch, J. Chueh, A. K. Wakhloo, and M. J. Gounis, "Preclinical acute ischemic stroke modeling," *J. NeuroInterventional Surg.*, Jul. 2011.

[53] F. M. Hinkmann, H. L. Voit, K. Anders, U. Baum, P. Seidensticker, W. A. Bautz, and M. M. Lell, "Ultra-Fast Carotid CT-Angiography: Low Versus Standard Volume Contrast Material Protocol for a 128-Slice CT-System," *Invest. Radiol.*, vol. 44, no. 5, pp. 257–264, May 2009.

[54] V. Sehgal, Z. Delproposto, D. Haddar, E. M. Haacke, A. E. Sloan, L. J. Zamorano, G. Barger, J. Hu, Y. Xu, K. P. Prabhakaran, I. R. Elangovan, J. Neelavalli, and J. R. Reichenbach, "Susceptibility-weighted imaging to visualize blood products and improve tumor contrast in the study of brain masses," *J. Magn. Reson. Imaging*, vol. 24, no. 1, pp. 41–51, Jul. 2006.